Theory and Application of Planar Ion Traps

by

Christopher Elliott Pearson

B.S. Physics, University of Washington (2006)

Submitted to the Department of Physics
in partial fulfillment of the requirements for the degree of

Master of Science in Physics

at the

MASSACHUSETTS INSTITUTE OF TECHNOLOGY

June 2006

Author .....
Department of Physics
May 26, 2006

Certified by .....
Isaac L. Chuang
Associate Professor of Physics
Thesis Supervisor

Accepted by .....
Thomas J. Greytak
Professor of Physics
Associate Department Head for Education

Theory and Application of Planar Ion Traps

by

Christopher Elliott Pearson

Submitted to the Department of Physics
on May 26, 2006, in partial fulfillment of the
requirements for the degree of
Master of Science in Physics

Abstract

In this thesis, we investigate a new geometry of Paul trap with electrodes in a plane. These planar ion traps are compatible with modern silicon microfabrication, and can be scaled up to large arrays with multiple trapping zones. We implement these designs on printed circuit boards with macroscopic ions, allowing us to study the traps while avoiding the experimental challenges of atomic ion traps. We discuss the dynamics of ions in the traps using both numerical and analytical means.

Scalable traps are of interest to the quantum computing community as a potential implementation of a large scale quantum computer. However, there are concerns about the low trap depth relative to a conventional trap of the same size. We address this in three ways, first by introducing a conductive plane above the trap to increase its depth, then by using a deeper trap with a three dimensional electrode geometry to load the trap, and finally by loading the trap directly while using a buffer gas to slow down energetic ions so that the trap can capture them. Also of concern is the ability of the trap to move ions through arms and intersections. We demonstrate these movement operations, and study properties of the linear trap including the secular frequency and geometric factors between planar and four rod traps.

The precision of atomic ion trap experiments makes them sensitive to background gas pressure at levels that are undetectable to conventional gauges. The capacity for integrating circuitry and optical elements with the trap could anticipate complete ion trap experiments performed by a single chip, and a new technology for an integrated pressure gauge would be immensely useful if the pressure detection can shown to be feasible and repeatable. In a point planar trap, we observe ion motion to determine background gas pressure, demonstrating an application that could bring planar ion traps into much wider use.

Thesis Supervisor: Isaac L. Chuang
Title: Associate Professor of Physics

Contents

List of Figures

List of Tables

Chapter 1

Introduction

The first experiments with trapped ions are nearly 50 years old [POF58, WSL59, Fis59], and ion traps have since proven their value as a tool for isolating a small number of particles in a controlled environment. These devices have seen widespread application in precision spectroscopy [IBW87], mass spectrometry [Tod91], atomic clocks [Fis97], and quantum computation [WMI+98]. Figure 1-1 shows a variety of Paul trap geometries used in these applications, along with those investigated here.

In this chapter we begin with the short history of the planar ion trap, and discuss its applications to quantum computing and to pressure measurement. We then briefly discuss our approach to these applications, and the context in which the analyses and experiments were performed, and detailing my specific contributions in this thesis research. We finish with an overview of the structure of this thesis.

1.1 The planar ion trap

In 2005, Chiaverini *et al.* [CBB+05] proposed a planar Paul trap geometry for ion trap quantum computing. In the same year, Stahl *et al.* [SGA+05] proposed a planar Penning trap geometry for use in precision spectroscopy and controlled particle interaction. The electrodes in these designs all lie in a plane, and ions are trapped above the plane of the electrodes [JPM90]. Such planar ion traps can be built using silicon VLSI technology and thus have the capability to scale to arbitrarily large and

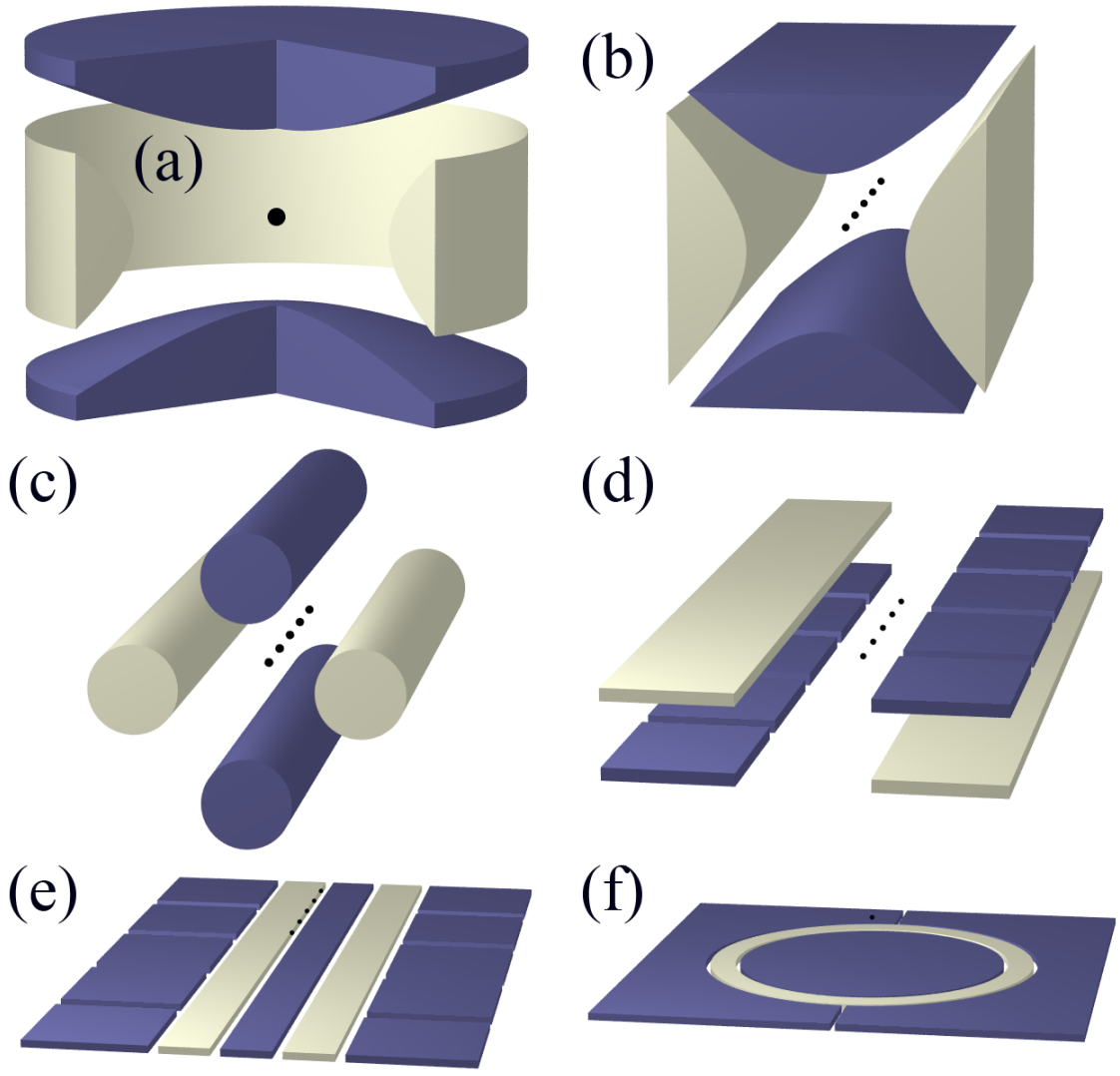

Figure 1-1: An assortment of Paul trap geometries. Light electrodes are driven at at an RF potential $V\cos(\Omega t)$ and dark electrodes are at RF ground. (a) The original point configuration, using hyperbolic electrodes. (b) The hyperbolic linear configuration. Both (a) and (b) produce ideal quadrupole potentials in the limit that the electrodes extend out to infinity. (c) A four rod geometry typical of mass spectrometry applications. (d) A stacked wafer linear design used in quantum computing applications. The ground electrodes are segmented to allow DC potentials to be applied. (e) The linear planar design investigated here. (f) The point planar design investigated here.

complex trap arrays [K$^+$05, KPM$^+$05].

In the five electrode linear planar design shown in Fig. 1-1(e), the center and outermost electrodes are held at RF ground while the remaining two electrodes are biased with an RF potential for radial confinement. The point planar design shown in Fig. 1-1(f) implements the same concept with concentric zones rather than strips.

Either the center electrode or the outermost electrodes can be segmented and DC biased. In the linear trap, this is useful for axial confinement and shuttling, while in the point trap it can be used to couple the ions to a test signal or to ions in other traps.

1.2 Application to scalable quantum computing

In recent years, the quantum computing community has demonstrated the basic building blocks of a scalable ion trap quantum computer [CZ95, WMI$^+$98, KMW02, Ste04]. The design uses the electronic states of ions trapped in a Paul trap as qubits and accomplishes logic gates and state readout by laser-ion interactions. Ions are shuttled between zones in an array of ion traps to perform two qubit gates between arbitrary pairs of qubits. Recent experiments have accomplished state readout [BZ88], one and two qubit gates [NLR$^+$99, TWK$^+$98], and ion shuttling in straight lines and through tees [R$^+$02, H$^+$05]. Scaling this architecture up to the many thousands of qubits necessary for a useful computation, however, will involve significant physics and engineering challenges.

One of these challenges is to build a many zone ion trap array capable of holding several thousands of ions in memory zones and moving arbitrary pairs of them together in interaction zones. The ion traps used for quantum computation are based on the linear Paul trap [PDM89, Pau90, RGB$^+$92, Gho95]. Current experiments typically use gold electrodes deposited on two or more alumina substrates with a geometry similar to that shown in Fig. 1-1(d) [T$^+$00, DHL$^+$04]. Ions are confined radially to the null axis of an RF quadrupole electric field, while axial confinement and ion movement operations are accomplished by DC electric fields. While these

multiple level traps can be adapted to microfabrication techniques [MHS+04], it is not clear whether they can be scaled to many zone traps because they require slots through the trap structure. This will make trap topologies that include loops difficult, as there will be islands of electrodes that will have to be mechanically supported and electrically connected.

The primary advantage of the linear planar trap configuration to quantum computing is its scalability to large, multiplexed arrays. Several challenges will have to be addressed, however, before planar ion traps can be used for quantum computing. Perhaps the most significant challenge is that planar ion traps have trap depths that are only of order 1% that of a multiple level trap of comparable dimensions [CBB+05]. While this is not a problem once the ions are loaded and laser cooled to near the ground state of the motion, it makes loading from a thermal ion source at room temperature or above difficult. A second challenge is to show that it is possible to perform the three basic ion movement operations required to implement the Kielpinski et al. [KMW02, WMI+98] ion trap quantum computer architecture in a planar trap: ballistic ion transport in straight lines, splitting and joining pairs of ions in a single trap, and shuttling ions around corners in intersections. Further challenges are that optical access for laser cooling is blocked along the axis orthogonal to the trap substrate, and that ion heating is enhanced first by the close proximity of the electrodes that is required to achieve a reasonable trap depth, and second by the more resistive semiconductor materials used for VLSI [YLS06]. We address the first and second challenges here. The latter challenges are addressed elsewhere [K+05, YLS06].

1.3 Application to pressure measurement

Two limitations on the attainability and usefulness of extreme high vacuum [Red99] are the outgassing by ion gauges and residual gas analyzers, and the inability of gauges to read pressures much lower than 10^{-10} torr. However, pressures below this, as low as 10^{-17} torr, have been reported in cryogenic environments using ion and atom traps as the gauge [G+91, WL95]. Collisions with background gas were undesirable

sources of decoherence and atom loss in these cases, but by loading a simple ion trap or array of traps and watching for collisional effects, it would be possible to measure pressures down to levels limited only by the ions' collision cross section and the allowed observation time.

Of course, observing individual collisions is not the only way to determine background gas pressure using trapped ions. The pressure sensitivity of trapped ion dynamics was observed even in the first experiments with charged aluminum dust [WSL59]. At higher pressures, changes in the ion motion can be observed as individual ions are slowed and cooled by the gas, or as collections of ions undergo transitions from cloud-like to crystalline states. At still higher pressures, the trap stability is affected [WO91, NF01]. This variety of sensitivities may make it possible to use a single ion trap device to measure pressures over ranges as large or larger than any single gauge available today.

In this application, planar traps have the immediate advantage of mechanical simplicity. In addition, for traps fabricated on silicon we gain the potential for integrated lasers and microelectromechanical (MEMS) optics, and electronic ion detection and control systems [KPM$^+$05]. These technologies make an integrated circuit pressure gauge an encouraging goal for future work.

Just as in the quantum computing application, several challenges will need to be addressed in order for ion traps in general and planar traps in particular to become a useful technology for pressure measurement. First among these is finding appropriate ion species and dynamical mechanisms for measuring pressure in ranges of interest. Second, we must show that it is possible to carry out these measurements to arrive at reliable values for pressure, that are not washed out by chronic systematic or random errors. Third, we must make the loading and measurement processes sufficiently reliable that they can be performed entirely automatically over long periods of time, to yield useful results. Finally, the experimental apparatus must be trimmed down to the barest essentials to allow its use as a self-contained measurement device and not an experiment in and of itself: a user must be able to insert the gauge into a port on their system and simply switch it on. We address the first and second challenges

in this work.

1.4 In this work

We investigate planar ion traps using printed circuit board (PCB) electrodes to trap macroscopic charged particles in rough to high vacuum environments. We do not cool our ions, and imaging is accomplished by classical (off resonant) scattering of laser light. Because these experiments do not require an ultra high vacuum environment, we are able to achieve a fast cycle time for testing different electrode layouts. In each case we optimize the electrode geometry to maximize the trap depth, and employ soft ionization techniques to load the traps.

We demonstrate loading from a conventional four rod Paul trap acting as a reservoir of ions. Atomic ions could be laser cooled in the four rod trap before being transferred to the planar trap to circumvent the problem of low trap depth. We test trap layouts with segmented center electrodes and segmented outer electrodes, and have accomplished all three of the movement operations required for the Kielpinski et al. [KMW02] architecture. While transport, splitting and joining [R$^+$02], and movement through intersections [H$^+$05] have already been achieved in multi-level traps, this work represents the first realization of these operations in planar ion traps.

We demonstrate loading directly to a point Paul trap in high vacuum. We then excite and observe the motion of a small number of loaded ions to determine the background gas pressure, illustrating one mechanism for pressure measurement that is applicable down to the base pressure of the pumping system. We then compare these results with measurements using conventional gauge technologies.

1.5 Context and contributions

This work is performed under the supervision of Prof. Isaac Chuang in the Quanta research group, part of the Center for Ultracold Atoms and Research Laboratory of Electronics at MIT. The primary goal of this group's research is to realize implementa-

tions of quantum information processing, particularly using the ion trap architecture. In that context, goal of this work with PCB planar traps has been to understand their operation of the traps on a larger-than-atomic scale in order to guide and facilitate later research at the atomic scale.

I conducted this thesis work in two stages, focusing at first on showing the feasibility of the planar trap in a quantum computing context, and then investigating applications of the PCB planar trap in areas other than quantum computation. I was the first person in our group to begin dedicated research on planar ion traps following their proposal by Chiaverini [CBB+05], and so constructed many early versions of the traps with a variety of electrode layouts, loading schemes, and control electronics, in order to establish reliable procedures for operating the traps. David Leibrandt then constructed the vacuum enclosure described in Sec. 3, and he and Waseem Bakr performed the simulations described in Sec. 2.2 and the ion characterization and trap performance experiments described in Sections 3.2 and 3.3. We then published the work described in Chapters 2 and 3 [PLB+06].[1]

Meanwhile, I was busy deigning and investigating new PCB planar traps, including more complex linear trap arrays, and arrays of point traps like those described in [SGA+05]. Prof. Chuang suggested that I use the planar trap to measure background gas pressure in a cryostat while Waseem Bakr simultaneously attempted to set up an ion trap for strontium-88 in that system. Though I eventually left this cryostat collaboration, I continued the effort of applying the planar trap to pressure measurement in a room temperature vacuum environment. The remainder of the work discussed in this thesis I performed essentially in isolation, with some help from Stahl [SGA+05] and Prof. Chuang to get started on point trap theory (Chapter 4), which I then extended in Sections 4.2 and 4.3. The development of the experimental apparatus and method in Chapter 5 and the data acquisition and analysis Chapter 6 is entirely my own work.

[1]The material in these chapters is copyright © 2006 The American Physical Society, and is reprinted here in accordance with the terms of the usage agreement.

1.6 Overview

This paper proceeds as follows. Chapter 2 offers a general discussion of Paul trap design, the linear planar trap, and the effects of background gas on ion motion. In Chapter 3, we present a detailed description of our experimental setup, we characterize the macroscopic charged particles we use to test the linear trap, and present the results of our investigation of the linear trap including secular motion and ion movement experiments. In Chapter 4 we move to the point planar trap with a theoretical analysis of that configuration. Chapter 5 details the experimental method and apparatus for pressure measurement, and Chapter 6 discusses the results of this experiment. Finally, in Chapter 7 we review the results of these investigations and their implications regarding the application of planar ion traps.

Chapter 2

Theory: The Linear Planar Trap

In this chapter, we begin with a discussion of ion dynamics in terms of electric potentials and pseudopotentials in Paul traps in general and linear traps in particular. Next, we explore some simulated linear geometries, using them to determine trap location, depth, and secular frequencies from specified electrode dimensions. Finally, we discuss the important influence of background gas on the motion of macroscopic ions in these traps.

2.1 Linear Paul trap theory

The motion of an ion in a Paul trap is determined by solving classical equations of motion [Gho95]. For an RF quadrupole electric potential in a linear configuration,

$$\phi(x, y, t) = \frac{x^2 - y^2}{2r_0^2} \left(U - V\cos(\Omega t)\right), \tag{2.1}$$

where V and U are the RF and DC voltages applied to opposing electrodes (see Fig. 1-1) and r_0 is the distance from the trap center to the electrode surface in a hyperbolic electrode trap, the x and y equations of motion take the form of Mathieu equations:

$$\frac{d^2 r_i}{d\tau^2} + \left(a - 2q\cos(2\tau)\right) r_i = 0. \tag{2.2}$$

Here $r_i = x$ or y, $\tau = \Omega t/2$ is a scaled time, the Mathieu parameters

$$q = \frac{2QV}{m\Omega^2 r_0^2} \tag{2.3}$$

$$a = \frac{4QU}{m\Omega^2 r_0^2} \tag{2.4}$$

are scaled RF and DC voltages respectively, and Q and m are the ion charge and mass.

The ion motion is stable (*i.e.*, both components of the ion position, x and y, are bounded in time) for certain regions of the a-q parameter space. In particular, for $a = 0$, the motion is stable for $0 < q \leq q_{max} = 0.908$.

In the pseudopotential approximation, where $q \ll 1$, the ion motion in the r_i direction can be decomposed into slow, large amplitude secular motion at the secular frequency ω_i and fast, small amplitude micromotion at the RF drive frequency Ω [Deh67]. For arbitrary RF and DC electric potentials $\phi_{RF}(\mathbf{r})$ and $\phi_{DC}(\mathbf{r})$, such that

$$\phi(\mathbf{r}, t) = \phi_{RF}(\mathbf{r}) \cos(\Omega t) + \phi_{DC}(\mathbf{r}), \tag{2.5}$$

the secular motion is described by the secular potential or 'pseudopotential'

$$\Psi(\mathbf{r}) = \frac{Q^2}{4m\Omega^2} |\boldsymbol{\nabla} \phi_{RF}(\mathbf{r})|^2 + Q\, \phi_{DC}(\mathbf{r}). \tag{2.6}$$

Note that the additional factor of Q makes this an electric potential energy. The pseudopotential for the linear planar trap investigated here is shown in Fig. 2-1.

Using the pseudopotential, we can calculate the ion height above the trap substrate r_0, the secular frequencies ω_i in the harmonic region of the potential, and the trap depth Ψ_0. The trap depth is defined as the minimum energy required by an ion sitting at rest at the trap minimum to escape to an electrode surface or to infinity. If the escape path is known, then it is simply the difference between the pseudopotential's maximum value along that escape path and its value at the trap minimum.

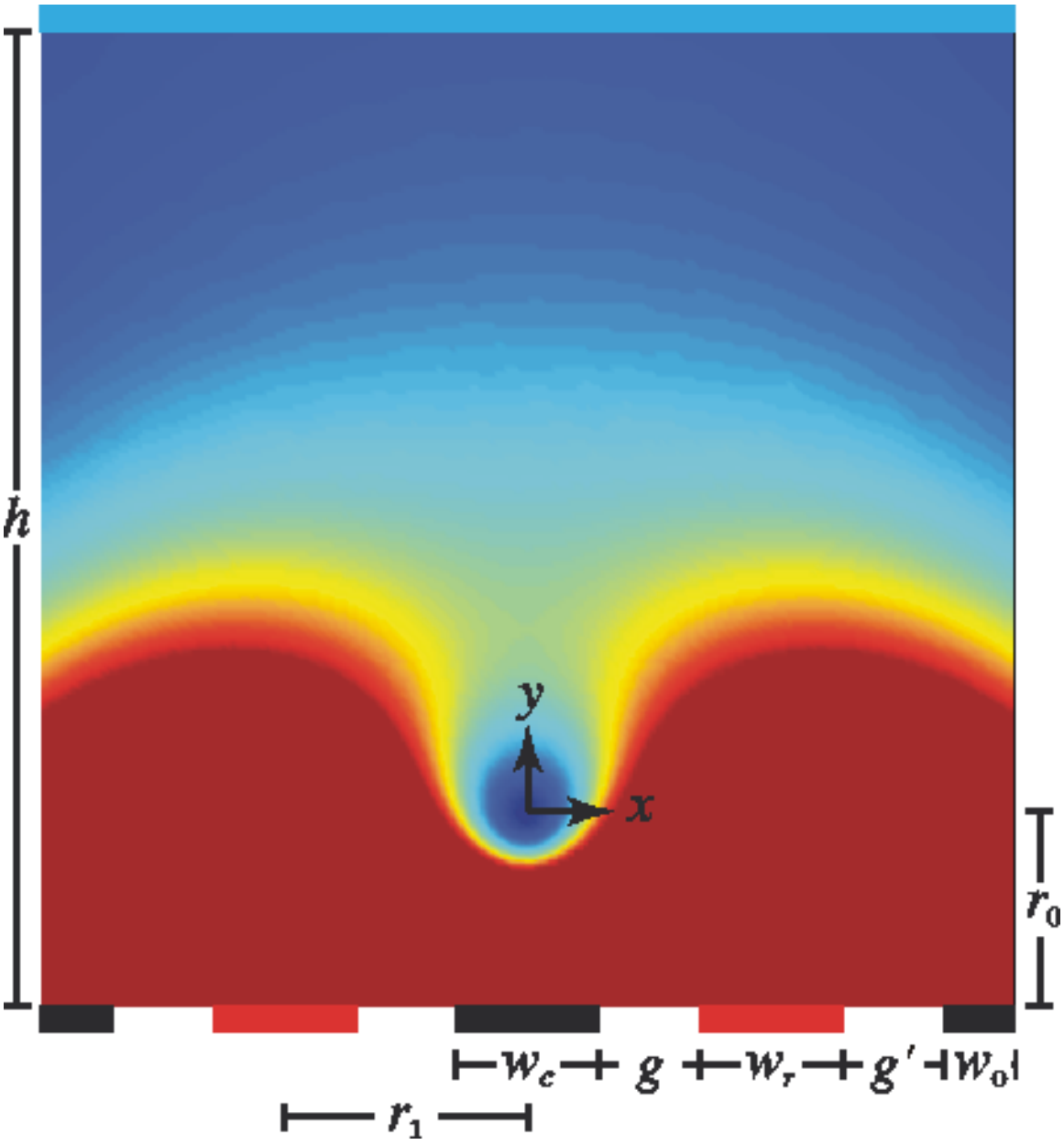

Figure 2-1: Pseudopotential for a planar ion trap. The particular geometry depicted is that of the cross trap described in Sec. 3. The pseudopotential is plotted on a linear color scale as a function of x and y, with blue representing the lowest and red representing the highest secular potential values. Pseudopotential values higher than twice the trap depth are truncated for clarity. The ion is located at the origin of the coordinate system. An RF potential $V\cos(\Omega t)$ is applied to the red electrodes at the bottom, a DC potential U is applied to the blue top plate electrode ($U = 0$ in this figure), and the black electrodes are grounded.

2.2 Simulated linear geometries

In order to determine the optimum relative sizes of the trap electrodes, we have calculated the pseudopotential numerically for the planar trap geometry defined in Fig. 2-1 over a range of dimensions using a two dimensional finite element electrostatic package named BELA [Mee04]. Here, w_c is the width of the center electrode, w_r is the width of the RF electrodes, w_o is the width of the outer electrodes, g is the width of the gap between the center and the RF electrodes, g' is the width of the gap between the RF and outer electrodes, h is the height of a planar electrode which is parallel to and above the trap electrodes, r_0 is the height of the ion above the trap electrodes, and $r_1 = \frac{1}{2}(w_c + w_r) + g$ is a measure of the trap size. We set $g' = g$ and $w_o \to \infty$, and varied w_c, w_r, and h. Note that $h \to \infty$ for a true planar trap.

Figures 2-2 and 2-3 show the scaled trap depth d_0 and scaled secular frequency f_i defined by

$$\Psi_0 = \frac{Q^2V^2}{4m\Omega^2 r_0^2}\, d_0 \tag{2.7}$$

$$\omega_i = \frac{QV}{\sqrt{2}m\Omega r_0^2}\, f_i \tag{2.8}$$

$$= \frac{q_i\Omega}{2\sqrt{2}} \tag{2.9}$$

as functions of w_c/r_0 and w_r/r_0 for $h/r_1 = 706$. Note that $d_0 = f_i = 1$ for a perfect quadrupole trap (Fig. 1-1(b)). In Eq. (2.9) we absorb the factor f_i into the Mathieu q_i parameter such that the stability region $0 < q_i \leq q_{max} = 0.908$ is the same for all trap geometries. We then have a form for the Mathieu q parameter that applies to traps of any geometry:

$$q_i = \frac{2QV}{m\Omega^2}\frac{f_i}{r_0^2}. \tag{2.10}$$

Here we have the freedom to define r_0 to be any characteristic dimension we wish, provided we adjust f_i appropriately such that the quantity f_i/r_0^2 remains constant.

We consider the secular frequency in the harmonic region of the pseudopotential, where in the case of the linear planar trap it is the same along both axes. This

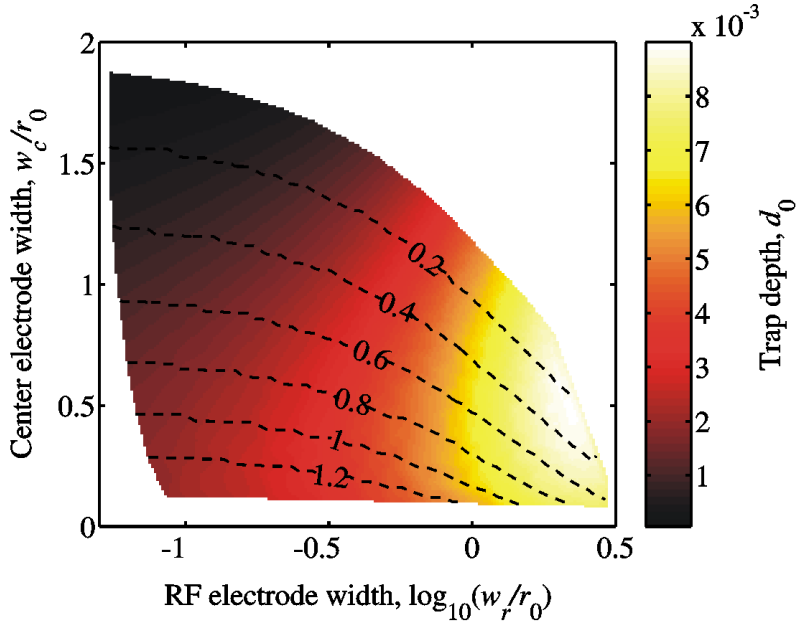

Figure 2-2: Trap depth versus electrode widths. The normalized trap depth d_0 is plotted in color as a function of $\log_{10}(w_r/r_0)$ and w_c/r_0 for $h/r_1 = 706$. The dashed lines are contours of constant g/r_0. Note that the maximum trap depth is obtained for $w_c/r_0 \approx 0.5$ and w_r/r_0 as large as possible.

approximation is appropriate when the ions have low kinetic energy compared to the trap depth.

Using Figs. 2-2 and 2-3, we can design a planar trap to maximize the trap depth subject to our experimental design constraints. For example, consider a planar ion trap for $^{88}Sr^+$. The ion height r_0 is set by either the acceptable ion heating rate or by how tightly the cooling and other lasers can be focused such that they do not scatter off the surface of the trap. Suppose we pick $r_0 = 500$ μm. The electrode widths w_c and w_r should be chosen to maximize the trap depth using Fig. 2-2, subject to the constraint that the gap between them g must be large enough that the RF voltage does not induce electrical breakdown. In general, the optimum center electrode width is around $0.5r_0$, and the optimum RF electrode width is as wide as possible given practical considerations such as the capacitance of a large electrode. For our example, suppose further that $g = 0.5r_0 = 250$ μm and $w_r = r_0 = 500$ μm. Figs. 2-2 and 2-3, then, give $w_c = 0.58r_0 = 290$ μm, $d_0 = 0.0065$, and $f_i = 0.28$. At $V = 500$ V and

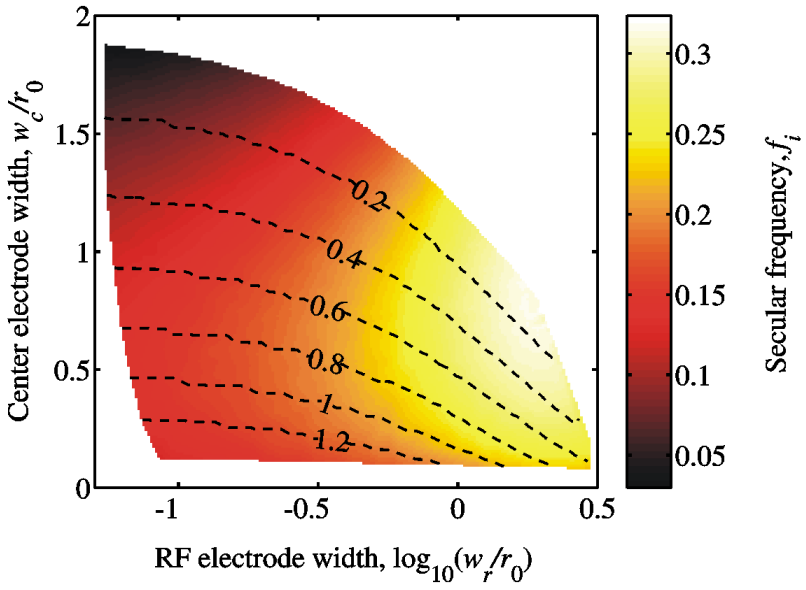

Figure 2-3: Secular frequency versus electrode widths. The secular frequency at zero ion temperature f_i is plotted in color as a function of $\log_{10}(w_r/r_0)$ and w_c/r_0 for $h/r_1 = 706$. The dashed lines are contours of constant g/r_0.

$\Omega = 2\pi \times 10$ MHz, this corresponds to $\psi_{sec,0} = 0.47$ eV and $\omega_i = 2\pi \times 1.1$ MHz.

We have found that by adding a planar top electrode (i.e., choosing h to be finite) biased at a positive DC potential U we can increase the trap depth by up to a factor of a 40 for a given RF amplitude and frequency. Figure 2-4 shows a scaled trap depth d_1 defined by

$$\Psi_0 = \frac{Q^2V^2}{4mr_1^2\Omega^2}d_1 \tag{2.11}$$

as a function of the scaled voltage u on the top plate defined by

$$U = \frac{QV^2}{4mr_1^2\Omega^2}\frac{h}{r_1}u, \tag{2.12}$$

for $w_c/r_1 = w_r/r_1 = 0.6$ and several values of h/r_1. Note that the trap depth is scaled differently for this plot than it was for Fig. 2-2. This is because r_0 is a logical starting point for selecting the electrode dimensions, but r_1 is the fixed length scale once the trap is built.

At $u = 0$, the smallest barrier in the secular potential over which the ion can

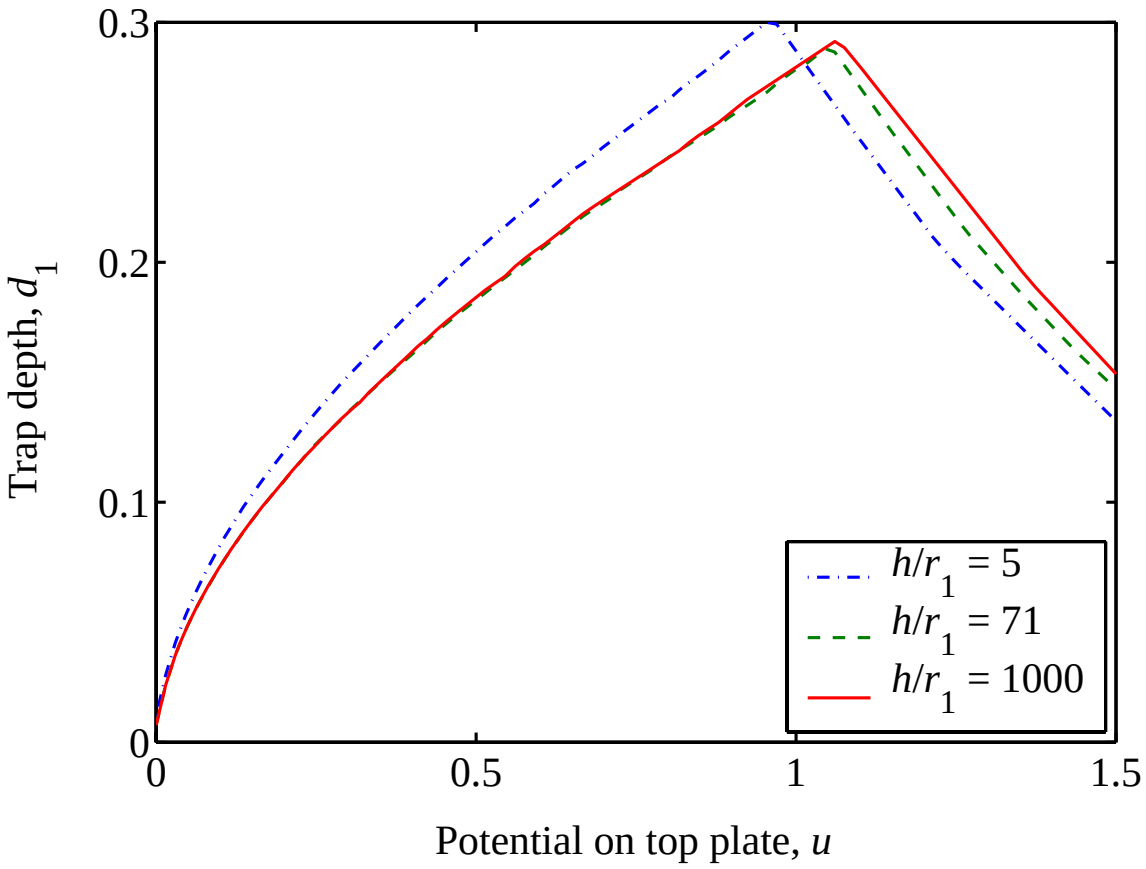

Figure 2-4: Trap depth versus top plate location and potential. The normalized trap depth d_1 is plotted as a function of u for $w_c/r_1 = w_r/r_1 = 0.6$ and several values of h/r_1. For $u \lesssim 0.2$, the ion escapes straight up in the positive y direction; for $0.2 \lesssim u \lesssim 1$, the ion escapes out to the side; and for $1 \lesssim u$ the ion escapes straight down in the negative y direction. Note that the maximum trap depth $d_1 \approx 0.29$ is obtained at $u \approx 1$.

escape is in the positive y direction. As u increases, the minimum energy escape path shifts first to the sides and then to the negative y direction. For a given geometry, the trap depth increases with u until the minimum energy escape path is straight down to the center electrode, then decreases with a further increase in u. The maximum trap depth occurs at $u \approx 1$ and is given by $d_1 \approx 0.29$, or a little more than one fourth the trap depth of a standard four rod ion trap with similar dimensions. The secular potential depends only weakly on h/r_1 because the effect of nonzero u is well approximated by a constant electric field in the regime $h/r_1 \gg 1$ that we consider. Note that because the DC potential pushes the ion off of the RF quadrupole null,

there will be increased micromotion. To first order in a harmonic potential, the micromotion amplitude is

$$q\Delta y/2 \tag{2.13}$$

where Δy is the displacement of the ion (located at the pseudopotential minimum) from the RF null. In practice we envision turning the DC potential on for loading, then gradually turning it off as the ions are laser cooled. Continuing our previous example, with a top plate electrode $h = 1$ cm above the trap biased at $U = 100$ V, we get a trap depth $\Psi_0 = 4.6$ eV and a micromotion amplitude of 15 μm using Eq. (2.13). A direct numerical calculation of the classical ion trajectory along the y axis predicts a micromotion amplitude of 20 μm, confirming that Eq. (2.13) is a reasonable approximation despite the rather anharmonic nature of the potential.

2.3 Ion motion in background gas

When trapping macroscopic ions in the presence of background gas, the gas exerts a drag force on the ions that both stabilizes the radial motion and slows down the axial ion movement operations. It is important to verify that the background pressure in our experiments is low enough to make accurate assessments of the trap performance.

For small Reynolds number and small Knudsen number,

$$Re = \frac{2\rho\dot{x}R}{\mu} \ll 1 \tag{2.14}$$

$$Kn = \frac{\lambda}{R} \ll 1, \tag{2.15}$$

where ρ, μ and λ are the gas number density, dynamic viscosity and mean free path, and $\dot{x}$ and R are the ion velocity and radius, the drag on a sphere takes the form of viscous damping

$$F_{drag} = -m\gamma\dot{x}, \tag{2.16}$$

where m is the ion mass. In this limit the damping coefficient γ is given by Stokes'

law

$$\gamma = \frac{6\pi\mu R}{m}. \tag{2.17}$$

However, when the Knudsen number is large compared to 1, Stokes' law overestimates the drag because the flow is no longer continuous. We divide Eq. (2.17) by an empirical slip correction factor

$$C(Kn) = 1 + Kn\left(1.165 + 0.483e^{-0.997/Kn}\right) \tag{2.18}$$

to obtain an expression for the drag force which is valid at larger Knudsen number [KMKP05].

To confirm the applicability of the modified Stokes' law, we must verify that we are at small Reynolds number. The micromotion of particles in the traps under investigation turns out to be

$$x_\mu \sim 0.5 \text{ mm } \cos(2\pi \text{ kHz } t), \tag{2.19}$$

such that

$$\dot{x}_\mu^{max} \sim \pi \text{ m s}^{-1}. \tag{2.20}$$

The viscosity of air is $\mu = 1.83 \times 10^{-5}$ Pa s [Bir45], the radius of our particles is $R = 0.22$ μm, and the mass density of air is

$$\rho_m = m\frac{P}{kT}, \tag{2.21}$$

where $T \approx 295$ K, $m \sim 5 \times 10^{-26}$ kg, P is the pressure and k the Boltzmann constant. A high estimate of the Reynolds number is therefore $Re \sim 10^{-4}$ P torr^{-1}, which is small for anything less than atmospheric pressure.

We may be able to make some useful approximations if we know the range of Knudsen number in which we are working. The mean free path is given by

$$\lambda = \frac{1}{\sqrt{2}\rho\sigma}, \tag{2.22}$$

where the number density ρ is given by the ideal gas law $\rho = \frac{P}{kT}$ and $\sigma = \pi d^2$ is the collision cross section. In this case the appropriate d is known as the kinetic diameter [LC01, XYLL00], and for molecular nitrogen and oxygen this is $d \approx 0.35$ nm. A low estimate of the Knudsen number is therefore $Kn \sim 255 \text{ torr}/P$. At pressures of a few torr and below, we are in the limit of large Knudsen number, such that the Cunningham slip correction factor Eq. (2.18) reduces to

$$C(Kn) \approx 1.648 \; Kn. \tag{2.23}$$

We determine the effect of drag on stability by considering a modified dimensionless equation of motion

$$\frac{d^2x}{d\tau^2} + b\frac{dx}{d\tau} + (a - 2q\cos(2\tau))\, x = 0 \tag{2.24}$$

where the dimensionless drag coefficient

$$b = \frac{12\pi\mu R}{C(Kn)m\Omega}. \tag{2.25}$$

A similar equation holds for the y motion. For $b = 0$, this reduces to Eq. (2.2). Numerical computations verify that the region of stable trapping in a-q parameter space grows with increasing b [WO91, NF01]. In particular, the maximum stable Mathieu q parameter at $a = 0$ goes from $q_{max} = 0.908$ at $b = 0$ to $q_{max} = 1.05$ at $b = 0.45$. The drag parameter b is plotted as a function of vacuum pressure p in Fig. 2-5. At 70 Pa (0.5 torr), $b = 0.45$ is already less than 1 so air drag has only a small effect on the trap stability in these experiments.

The speed of ion motion in our shuttling experiments, however, is significantly affected by drag. The physical reason for this is that the characteristic time for shuttling experiments is much longer than the characteristic time for stability ($1/\Omega$). As a simple model, consider an ion starting from rest at $z = 0$ in a piecewise linear

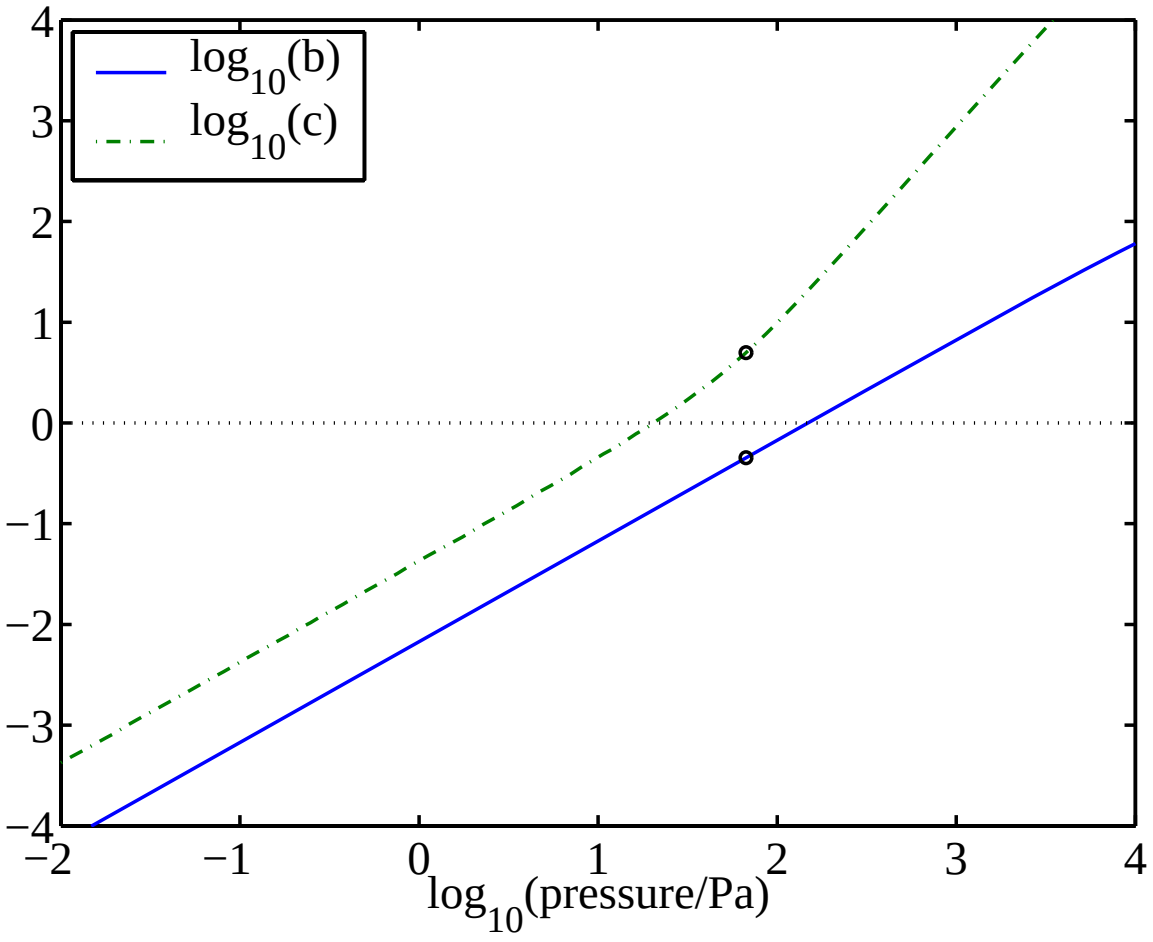

Figure 2-5: Drag coefficients describing ion stability and the speed of linear ion shuttling versus background pressure. The dimensionless drag coefficients b and c for stability and ion shuttling, respectively, are plotted as functions of the vacuum chamber pressure on a log scale. The drag coefficients are computed using $R = 0.22$ μm, $Q = 5.3 \times 10^{17}$ C $= 330$ e, $m = 4.7 \times 10^{-17}$ kg, $\mu = 1.83 \times 10^{-5}$ Pa s, $\lambda = (67.3 \text{ nm})(10^5 \text{ Pa}/p)$, $\Omega = 2\pi \times 5$ kHz, $d = 1$ mm, and $E = 10^3$ V mm^{-1}; which is appropriate for the cross trap assuming that we are trapping single microspheres. The circles indicate the values of the drag coefficients at the pressure used in our experiment.

axial potential

$$\phi(z) = \begin{cases} E(L-z) & , \quad z < L \\ 0 & , \quad z > L \end{cases} \tag{2.26}$$

and suppose we measure the ion velocity when $z = L$. In this model the length scale L is of the order of the axial dimension of a control electrode, and the electric field E is of the order of the electric potential applied to a control electrode divided by its axial dimension. Drag is important when the dimensionless drag parameter $c = \gamma t_L \gtrsim 1$ where t_L is the time to reach $z = L$. Here t_L is the solution to the transcendental equation

$$L = \frac{QE}{\gamma m}\left(t_L + \frac{e^{-\gamma t_L} - 1}{\gamma}\right) . \tag{2.27}$$

The dimensionless drag coefficient c is plotted as a function of pressure in Fig. 2-5. At 70 Pa, $c = 4.9$ so drag plays an important role in ion shuttling experiments in the cross trap despite the fact that the trap stability is not affected by damping.

For large damping ($c \gg 1$), $\dot{z}(z = L)$ approaches the terminal velocity $(QE)/(\gamma m)$. The drag coefficient $\gamma \sim 1/C(Kn) \sim 1/Kn \sim P$, so $\dot{z}(z = L) \sim 1/P$. This is experimentally verified in Sec. 3.3.3, and the relationship $\gamma \sim P$ is studied in much greater detail in Chapters 5 and 6.

Chapter 3

Experiment: Characterizing the Linear Planar Trap

The design of a planar trap for use with macroscopic ions involves three main considerations: the ion source, the ion loading mechanism, and the design of the trap itself. Particle ion sources in common use include electrospray ionization [YF84], laser ablation [KBBH87, BCS89], and piezoelectric particle generation [AF86]. Careful choice of an ion loading scheme is important because of the low trap depth of planar traps. The trap described in this chapter is loaded using a four rod trap with a higher trap depth. Designing the printed circuit board (PCB) containing the trap electrodes involves choosing the electrode dimensions to obtain the desired trap depth, ion height above the substrate, and secular frequencies; choosing the layout of the control electrodes to allow for performing the desired movement operations; and choosing a PCB substrate that has a high voltage breakdown threshold, does not accumulate charge easily, and is vacuum compatible in the case of a trap in a UHV environment.

The discussion in the previous chapter has provided us with appropriate trap dimensions. In the following sections we will describe the specific trap under consideration and the experimental setup. We will then characterize the trapped ions in terms of their charge to mass ratio and the trap in terms of the secular frequencies and ion heights. Finally, we will discuss the performance of the trap in executing movement operations.

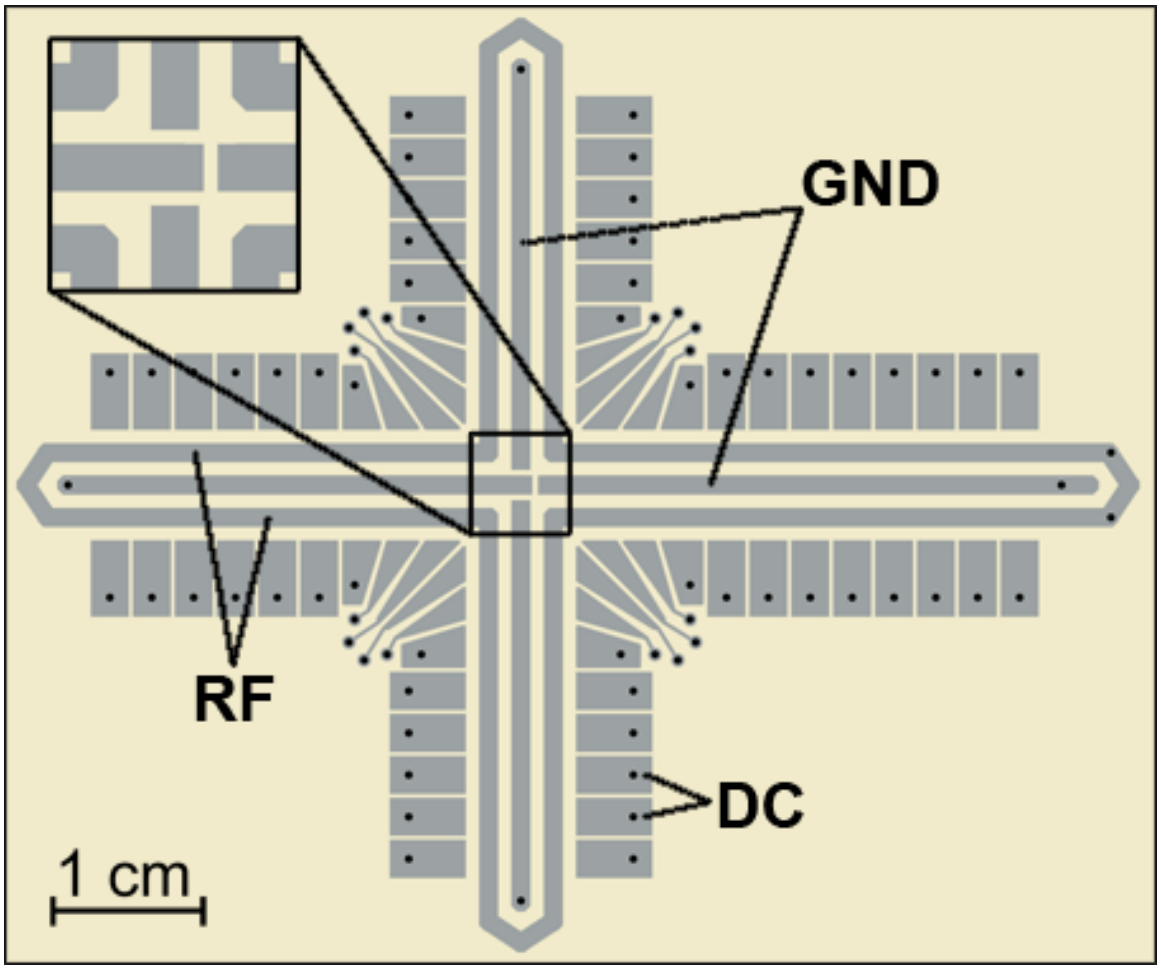

Figure 3-1: Top view of the trap. Opposing electrodes in straight sections of the trap are electrically connected, but near the intersection both the outer and center electrodes are separated to provide finer control. Electrical connections are made via surface mount headers on the underside. The RF loop at each end helps prevent ions from leaking out axially.

3.1 Experimental apparatus

In this section, we discuss the specifics of the trap's design and construction, our source of ions, the method for loading the planar trap, the environment used for performing our experiments, and our methods for measurement and control of ions.

The planar trap under consideration is made up of four straight arms joined at a cross intersection (Fig. 3-1). It is a printed circuit board (PCB), made using standard techniques. The electrodes are tin coated copper, and the substrate is GML-1000, a microwave laminate. The trap is a five electrode design, with outer electrodes segmented to control the axial potential. Connections to these electrodes are made on the bottom layer of the PCB using surface mount headers. Most opposing pairs of control electrodes are electrically connected, but the two pairs nearest the intersection on each arm are electrically independent for finer control. The center electrodes are also segmented at the intersection to provide additional control in that region. The middle three electrodes are all 1.27 mm wide, the electrode spacing is 0.89 mm, and the outer control electrodes are 2.5 mm long. We do not fully optimize the electrode sizes as discussed in Sec. 2.2 due to the practical considerations of printed circuit board manufacture, specifically minimum feature and drill sizes.

Electrospray ionization (ESI) provides ions to the trap. This technique, commonly used with linear quadrupole filters for mass spectrometry, applies high voltage to a liquid solution at a sharp tip. Strong electric fields at the tip blow off fine droplets of solution, and as solvent evaporates from these charged droplets, self repulsion breaks them up into smaller particles, eventually producing individual charged solute particles. Following [CPK$^+$02a], we begin with a 5% suspension of 0.44 μm diameter aminopolystyrene spheres. We then prepare a solution buffered to pH = 3.9 to encourage cationization of the amine groups, add methanol to produce a 4:1 methanol/solution mixture, and add the spheres to produce a 0.05% suspension. The suspension is then placed in a sealed bottle, and pressurized to 50-100 kPa. This forces the liquid through a 0.45 μm filter to block any clusters of microspheres, and out the electrospray tip. The tip itself is made from fused silica capillary tubing,

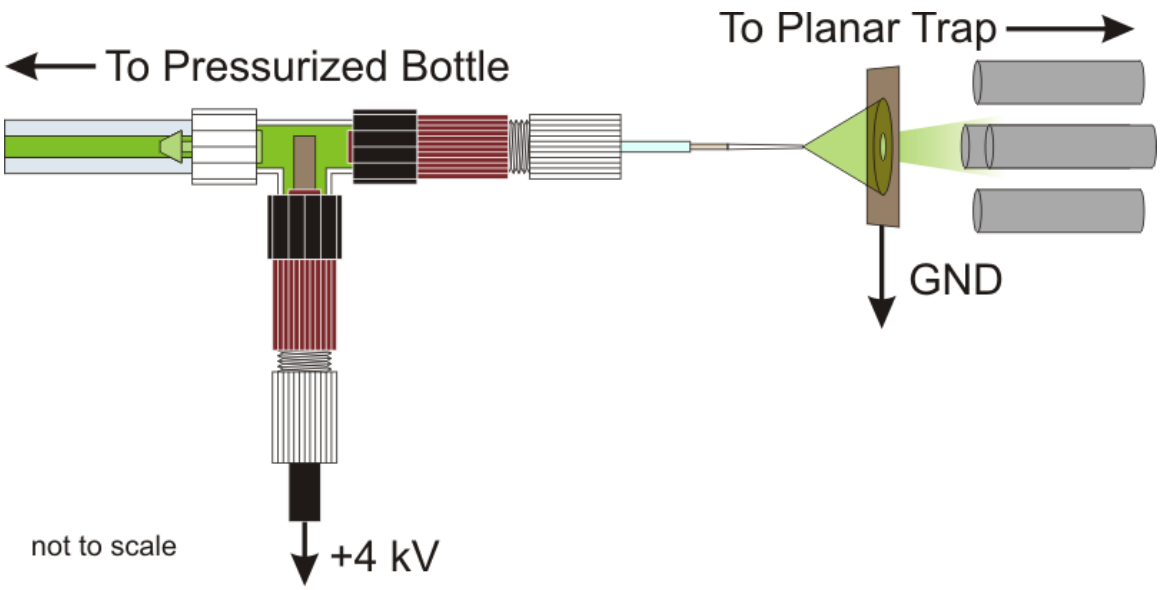

Figure 3-2: The ESI apparatus. Microspheres suspended in a mixture of methanol and water are forced from a pressurized bottle, through a 0.45 μm filter and past a copper wire with +4 kV applied voltage, and out the capillary tip. The charged spray passes through a mask and into a four rod trap.

which is heated, stretched to produce a neck, and cleaved to produce a 100 μm opening. We apply 4 kV directly to the liquid with a copper wire inserted in the fluid near the tip (Fig. 3-2). The spray plume from the tip is directed through a grounded mask and into the end of a four rod trap.

By arranging the rods so that they match the strips of a planar trap, we interface the four rod trap directly to the planar trap. A slot cut in the side of the PCB allows us to lower the four rod trap to a point where its trap axis coincides with that of the planar trap (Fig. 3-3). Mutual repulsion of ions loaded in the far end of the four rod trap forces them along, eventually pushing them into the planar trap. When completely full, the planar trap can hold $\sim$50 ions.

Electrospray ionization must be performed at or near atmospheric pressure, and experiments on free trapped particles require a vacuum, so we enclose both four rod and planar traps in a custom built clear acrylic box (Fig. 3-4), and load through an open side of the box. We perform all loading at atmospheric pressure, then seal the box shut and carefully pump down. We use a needle valve to control flow rate

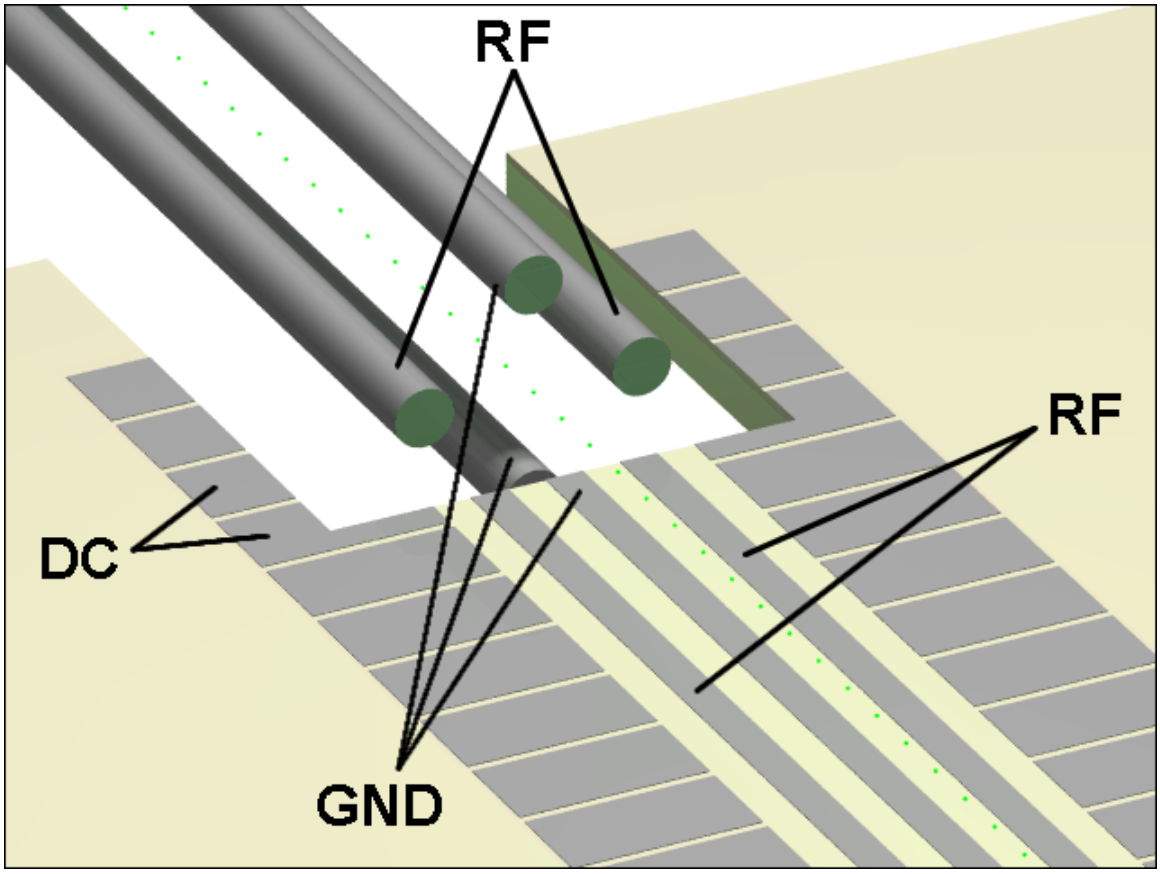

Figure 3-3: Four rod to planar interface. A slot cut in the planar trap allows for a common trap axis. The large particles form a linear Wigner crystal immediately and are pushed into the planar trap.

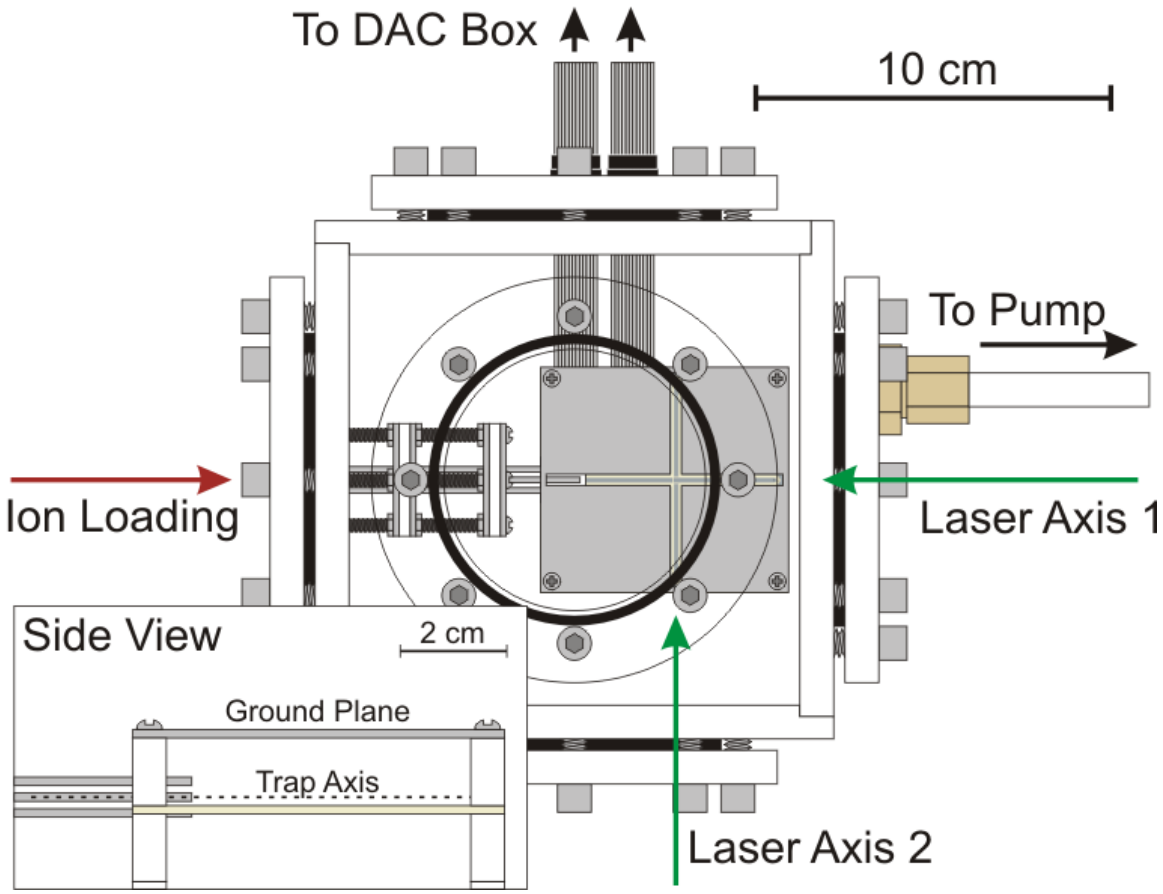

Figure 3-4: Top view of the vacuum chamber. Ions are loaded into the left side, and then a flange is screwed into place and the air evacuated slowly. Two green lasers illuminate the trap axes.

during pumping, since any significant air flow can push ions out of the trap. The lowest attainable pressure in this enclosure is about 0.10 torr (15 Pa). Green (532 nm) laser light directed along the trap axes illuminates ions by classical (off resonant) scattering. The ions are clearly visible to the naked eye, and we photograph them using a zoom lens mounted on a CCD camera.

Also shown in Fig. 3-4 is a metal plate installed above the trap to increase its trap depth and shield from stray static charge. Machined slots in this plate allow us to view ions from above, but we can also see them from the side. This slotted top plate design has the advantage of masking laser scatter, but for more complex trap topologies it might be easier to use a transparent conductor such as indium tin

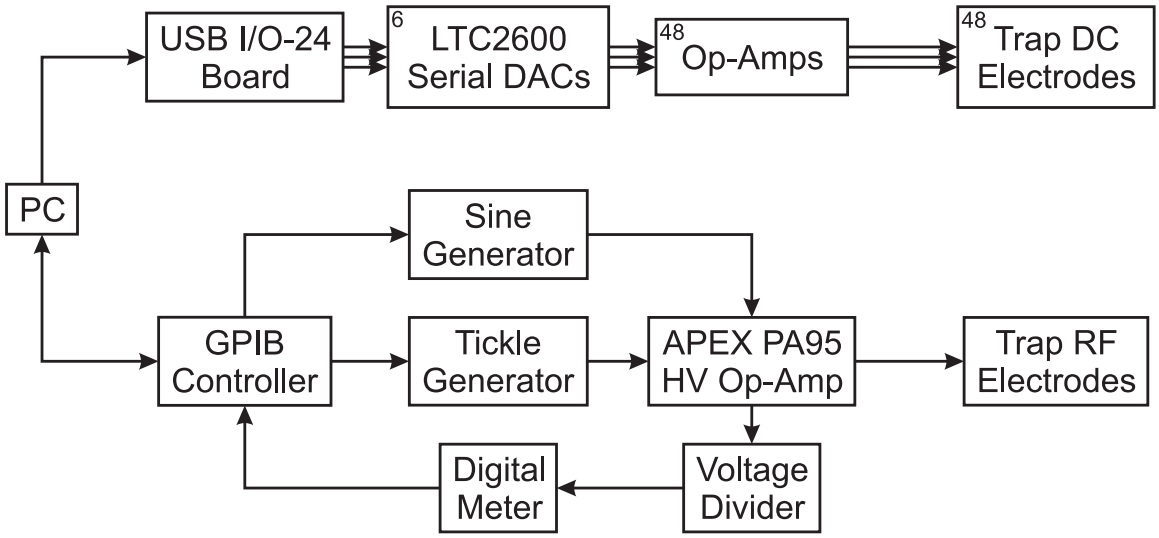

Figure 3-5: Control electronics for the planar trap.

oxide or a thin film of gold [Gor00, GH02, SHKS01]. This could be deposited on a glass plate or directly on the vacuum window or an imaging optic inside the vacuum chamber.

The electronics used to generate the RF and DC potentials for the trap are shown in Fig. 3-5. Frequencies for which the microspheres are stable range from a few hundred hertz to several kilohertz, depending on the pressure. This is in the audio frequency (AF) range, but we will continue to refer to it as RF. Since these frequencies are easily synthesized, we use a function generator as the source, then use an active high voltage amplifier to reach the target voltage range. A small tickle signal can be added to the main RF signal before amplification to probe for resonances in ion motion, allowing us to determine secular frequencies (Sec. 3.3.2). In this design, the upper limit to RF voltage is set by arcing between RF and ground electrodes, which occurs at about 400 V amplitude. Typical operating conditions are 250 V and 1.5 kHz.

To provide DC control of the trap's 48 independent electrodes, we use a board with 24 digital output channels to address six serial octal digital to analog converter (DAC) integrated circuits. The outputs of these DAC chips are then amplified to $\pm$20 V, sufficient to axially confine or to move these particles.

3.2 Ion characterization

Our goal in this set of experiments is to study the properties of planar traps rather than the ions loaded into them. To be able to draw conclusions about atomic ion traps from work on macroscopic ions, we must first scale away the charge-to-mass dependence from measured parameters.

The principal drawback of using macroscopic charged particles to investigate a trap design is that, unlike atomic ions, these particles are not identical. Electrospray ionization (ESI) is a soft ionization technique that produces multiply charged ions with a significant spread in the charge state. The variation in the mass of the microspheres ($\approx 10\%$) also contributes to broadening the charge-to-mass distribution. Nevertheless, we are able to keep the Q/m spectrum constant by maintaining constant electrospray pressure, voltage, capillary diameter and loading parameters.

To measure the Q/m spectrum of the ions, groups of about five ions at a time were loaded into the four rod trap with $\Omega = 2\pi \times 2$ kHz and $V = 250$ V. With the chamber pressure at 0.5 torr, the RF frequency was lowered while observing the ejection frequency Ω_{ej} of each ion. The charge-to-mass ratio was calculated using the formula

$$Q/m = \frac{q_{max} r_0^2 \Omega_{ej}^2}{2V}, \tag{3.1}$$

where $q_{max} = 0.908$ is the value of the Mathieu q parameter at the boundary of the first stability region of a quadrupole trap. Figure 3-6 shows a spectrum obtained for 178 ions with mean $Q/m = 1.17 \times 10^{-8}$ e/u (elementary charges per atomic mass unit).

3.3 Trap performance

When damping forces can be neglected, the Mathieu equations of motion of a trapped ion depend only on dimensionless parameters. It follows that the dynamics of macroscopic charged particles, viewed in the appropriate time scale (a micromotion period), are identical to that of atomic ions, and can be fully explored without the much more

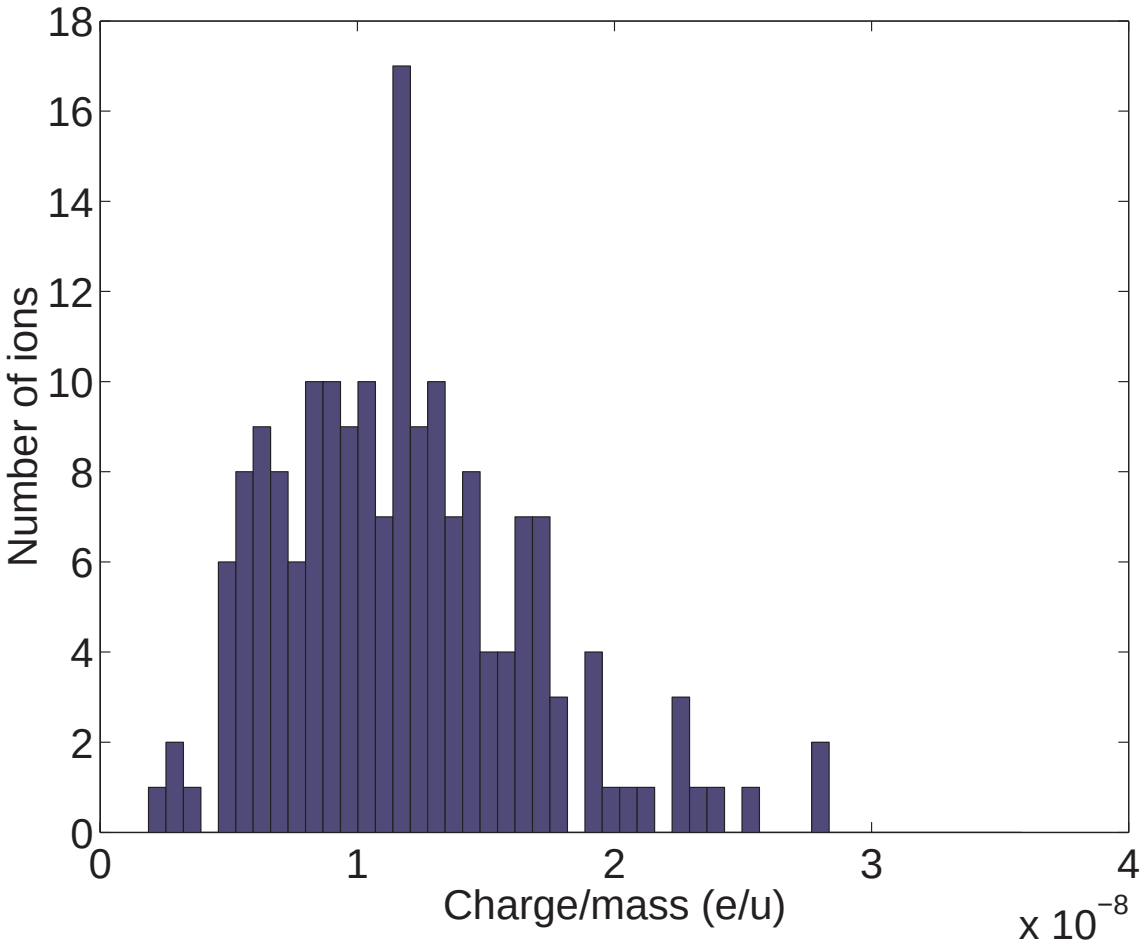

Figure 3-6: Charge-to-mass distribution of ESI generated ions. The mean $Q/m = 1.17 \times 10^{-8}$ e/u and the standard deviation is 0.49×10^{-8} e/u.

demanding experimental requirements of trapping atomic ions [HB93]. We have found macroscopic charged particle planar traps to be a rapid and accurate test bed for investigating traps of different geometries (e.g. three electrode, five electrode) and control electrode layouts (e.g. segmented center, segmented outer electrodes). In this section, we present the results of an experimental investigation of planar trap performance using this test bed.

3.3.1 Ion height above trap substrate

A planar trap with a segmented center electrode can be used to control the height of individual ions above the substrate by applying DC voltages to the electrode segments. One advantage of such control in a quantum computer is the ability to perform single qubit gates on different ions using a single stationary laser beam. The laser beam would have to be parallel to the ion chain but slightly raised or lowered. By changing the height of individual ions, they can be brought into the path of the beam to perform single qubit gates.

We measured the height of an ion above the trap substrate using a CCD camera mounted on a calibrated translation stage. The micromotion of the ion in the y direction causes the images (which have an exposure time much longer than the period of the RF drive) to show a streak where the ion is located, so we actually measured the positions of the top and bottom of the ion motion. Figure 3-7 shows the average of the positions of the top and bottom of the ion motion as a function of the DC potential on the center electrode. We measured Q/m for the ion by lowering the RF drive frequency until the ion became unstable as described in Sec. 3.2. The expected ion height shown in Fig. 3-7 is calculated using this value of Q/m and a numerical computation of the pseudopotential.

Figure 3-8 shows the amplitude of the ion motion as a function of the DC potential on the center electrode. The micromotion is minimized when the ion is located at the null of the RF quadrupole electric field, which occurs when the potential on the center electrode is zero. Even without a bias on the center electrode, however, there is still a substantial amplitude of ion motion because we do not cool the secular motion

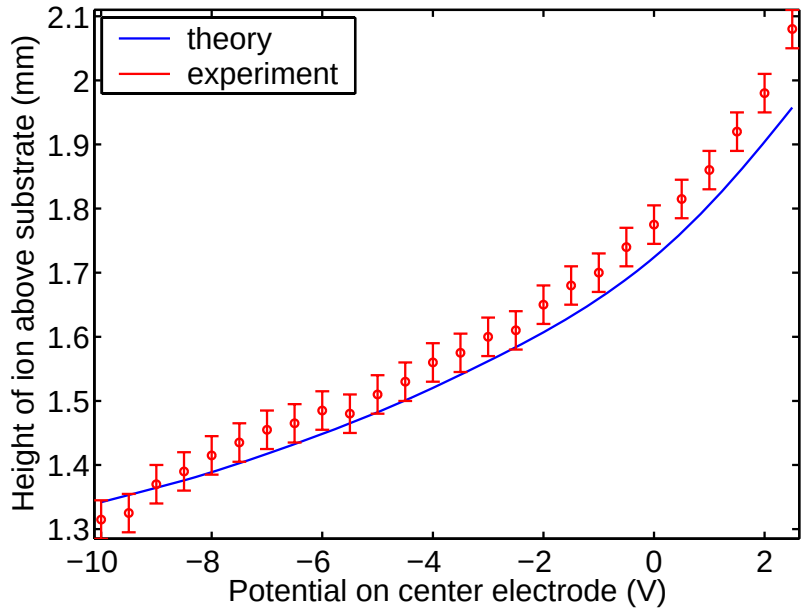

Figure 3-7: Ion height above the trap substrate, r_0, is plotted as a function of the DC potential on the center electrode. The solid line is the expected ion height from numerical computations of the pseudopotential as described in Sec. 2.2 using the measured charge-to-mass ratio of the ion.

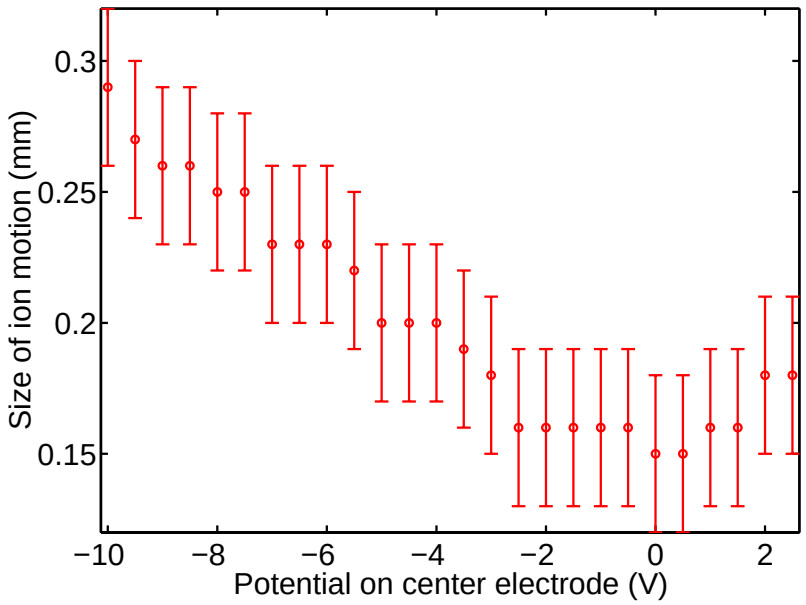

Figure 3-8: Ion motion amplitude. The peak to peak amplitude of the ion motion in the y direction is plotted as a function of the DC potential on the center electrode.

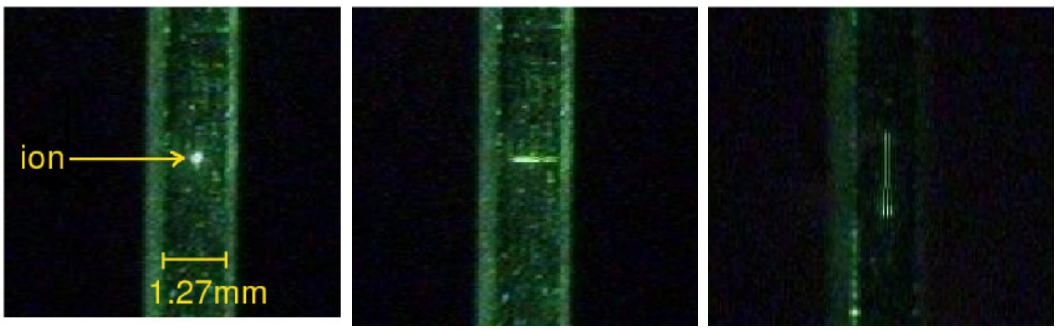

(a) (b) (c)

Figure 3-9: (a) Top view of an ion trajectory from secular resonances with $V = 250$ V and $\Omega = 2\pi \times 2$ kHz. Only the center ground electrode is seen in these pictures because the grounded top plate electrode masks the other electrodes from view. The width of the ground electrode is 1.27 mm. (b) Transverse mode excited at a drive frequency of 288 Hz. (c) Axial mode excited at 25 Hz.

of our ions.

3.3.2 Secular frequencies and trap geometric factors

We determine the secular frequency of an ion by adding a Fourier component of frequency Ω_t and amplitude V_t to the RF signal. Typically, V_t is between 0.5 V and 2 V. By sweeping Ω_t, we are able to observe a sharp increase in the extent of the ion trajectory along the direction of the secular mode excited by the drive signal as seen in Fig. 3-9. Although the drive signal is applied to the RF rods, indirect coupling of the drive to the axial motion of the ion is sufficient to excite axial modes. The exact axial secular frequency depends on which trap electrodes are used as end caps and what voltage is applied to them, but it is typically between 15 Hz and 30 Hz. The transverse secular frequencies are of more interest because they depend directly on the trap geometry: the geometric factor f_i/r_0^2 in Eq. (2.8) depends only on electrode dimensions and their spacing. We were not able to resolve separate resonant frequencies for ω_x and ω_y, which indicates that the ion energy is much less than the trap depth. Figure 3-10 shows the dependence of the x secular frequency on V and Ω. Both dependences behave as expected from the pseudopotential approximation.

To confirm the accuracy of our simulations of pseudopotentials in planar traps,

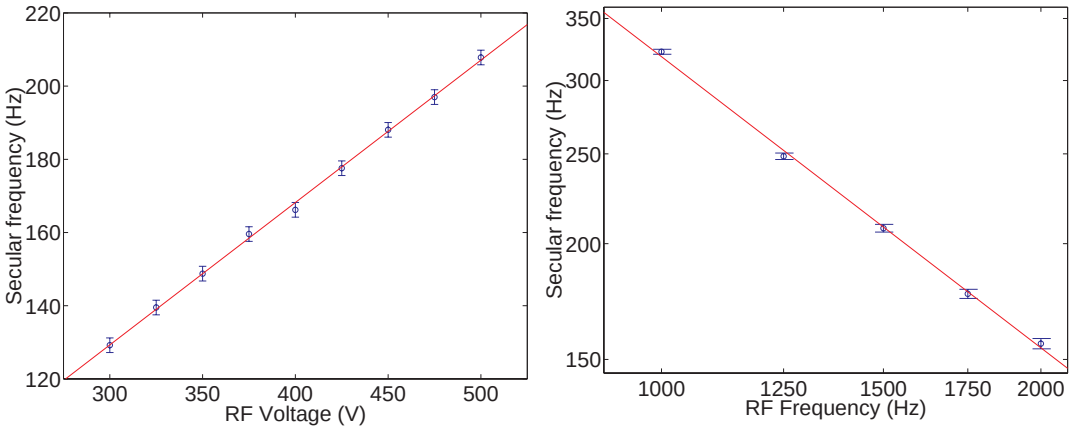

(a) (b)

Figure 3-10: Measurements of the secular frequency versus (a) RF amplitude at a fixed RF frequency of 1.5 kHz (on a linear scale) and (b) RF frequency at a fixed RF amplitude of 250 V (on a log scale). The solid lines are fits to Eq. (2.8) with $\frac{Q}{m} f_i$ as a fit parameter.

we measured the ratio of the geometric factor f_x/r_0^2 in the planar trap to that of the loading four rod trap. The large spread in the Q/m distribution does not allow for the determination of the geometric factor for each trap separately. However, we can measure the ratio of the geometric factors of the traps by first measuring ω_x of an ion in the planar trap, then applying a sequence of voltages on the control electrodes to move that ion into the four rod trap, where ω_x is measured again. By doing several experiments of this kind, we determined the geometric factor ratio to be 0.40 ± 0.01. Numerical simulations of this setup were also performed using BELA, giving for this ratio the value 0.404, which is within the error bar of the experimental result.

3.3.3 Ion movement

Three important ion movement primitives for a multiplexed ion trap quantum computer are shuttling, turning corners and splitting/joining two ions [KMW02]. We have demonstrated these three operations in planar traps, using our macroscopic charged particle system.

Figure 3-11 shows a strobe image of shuttling a microsphere in the planar trap at 0.34 torr. The shuttling shown was performed by raising the potential of the nearest

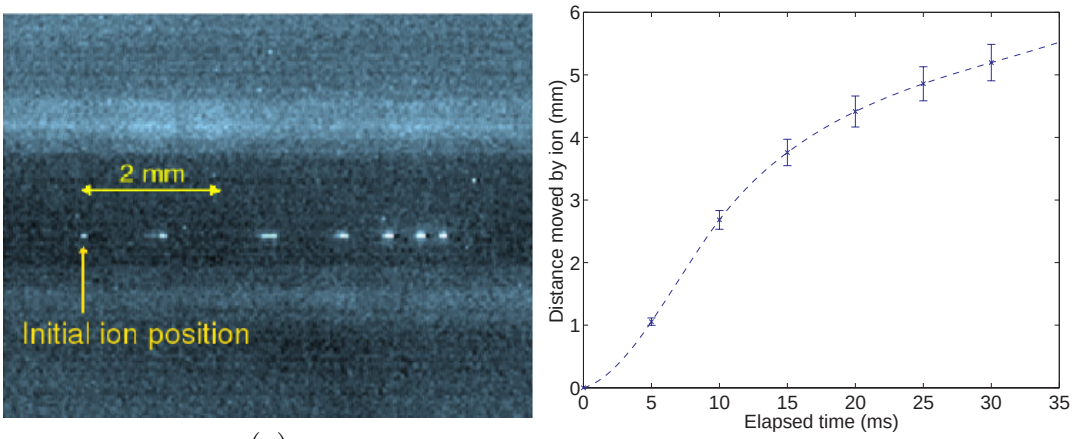

(a) (b)

Figure 3-11: (a) A strobe image showing shuttling of a single ion, taken by modulating the current to the illuminating laser. The laser is periodically turned on for 2 ms and off for 5 ms. The ion is moving from left to right; there is a short acceleration period after which the ion reaches a maximal velocity and then decelerates. This shuttle was performed by applying a potential of 5 V to the nearest control electrode that is to the left of the ion. (b) Distance moved by the ion versus elapsed time, fitted with a spline to guide the eye.

control electrode to the ion. In this case, the speed of the ion and its final position are determined both by the electrode potential and the drag force on the ion. Figure 3-12 shows how the maximum speed the ion achieves during its motion depends on these two parameters.

We have also shuttled ions using another scheme where the nearest control electrodes on both sides of an ion are used to create a confining well along the axial direction. By moving this well along the trap, we have more control over the acceleration, speed, and final position of the ion.

Splitting a pair of ions was performed by using the control electrodes to introduce a potential hill that pushes the ions apart. The ion spacing is approximately equal to the axial dimension of one control electrode, so this technique is satisfactory. Typically, an electrode between the ions is raised to 5 V for separation and lowered back to 0 V to join them again. For performing two qubit gates with atomic ions, it is desirable to bring the ions as close to each other as possible, because gates are fastest when the frequencies of the two axial normal modes of the ions are well separated [SS03].

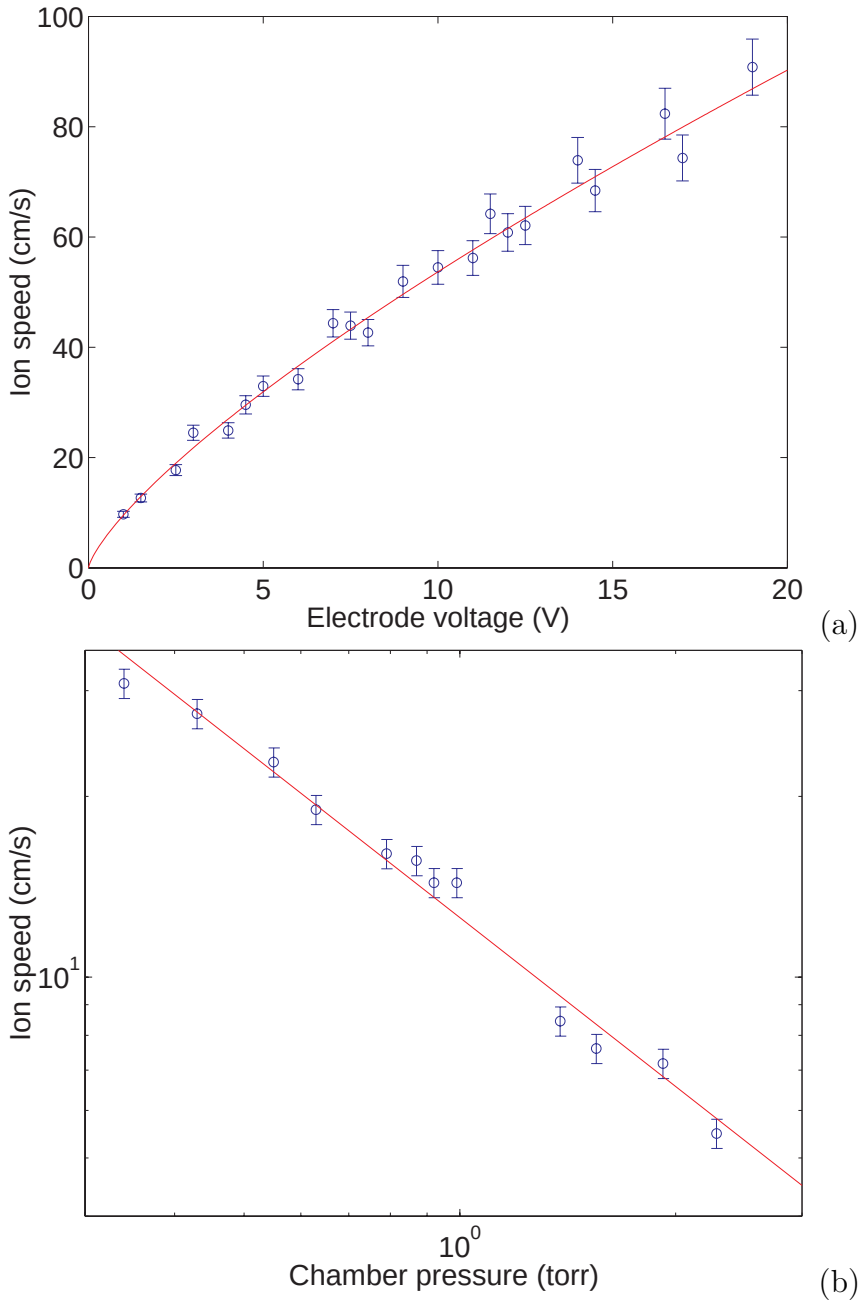

Figure 3-12: The maximum speed v_{max} an ion attains during a shuttling operation versus (a) the potential u_c applied to the nearest control electrode at constant pressure (0.34 torr) fit to a 3/4 power law ($v_{max} = Au_c^{3/4}$ where $A = 9.55$ cm s^{-1}V$^{-\frac{3}{4}}$) (b) the chamber pressure at constant control electrode voltage (5 V). Ion speed is found to be inversely proportional to the chamber pressure. This behavior is expected for (1) large Knudsen number and (2) $\gamma t_L \gg 1$ where γ the damping coefficient and t_L is the acceleration time of the ion (see Sec. 2.3). When the damping is low enough such that (2) no longer holds, the ion speed is expected to reach a pressure-independent value.

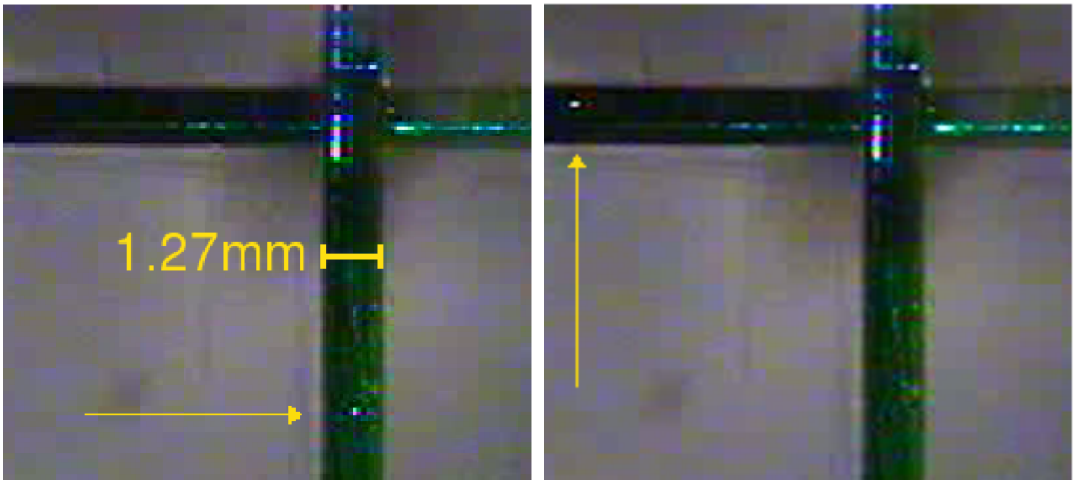

(a) (b)

Figure 3-13: Turning a corner. The arrows point to the position of the ion (a) before and (b) after turning the corner. This operation takes about 50 ms.

In that case, the ion spacing is likely to be smaller than the electrode spacing, and it has been shown that it is advantageous to use the DC electrodes to produce an electric octopole moment for fast separation [HS03].

Figure 3-13 shows an ion turning a corner in the planar trap. Simulations of the pseudopotential indicate that there are potential hills in the RF nodal lines in each of the four arms close to the intersection, with a point node right at the intersection. To turn a corner, it is necessary for an ion to overcome the hills in both the source and destination arms. We have used the following pulse sequence to do that: (1) lower the center electrode of the destination arm to -2 V, then (2) raise a control electrode in the source arm to 5 V to push the ion over the hill in the source arm. We find that the ion has enough kinetic energy after traversing the first potential barrier to also overcome the second one.

Chapter 4

Theory: The Planar Point Trap

Traps in linear configurations are invaluable for storing, moving and operating on arrays of ions. However, for experiments that don't require translation, such as those studying small crystals or clouds of ions, a more symmetric trap is advantageous.

In a point trap, there is no need to use DC electrodes to confine the ions axially, or to perform 3D simulations to determine the resulting axial potential. Even in linear traps where the axial potential has been calculated, dielectric charging in the trap could distort the axial potential beyond recognition.

In our application of the planar trap as a pressure gauge, we'll be using small numbers of ions. The smaller extent and greater symmetry of a point trap will be useful to keep the ions well localized and in a more accurately known potential.

This chapter will take a different approach to analyzing the point trap than was used in Chapter 2. Instead of simulating the pseudopotential on a computer, we will calculate the potential analytically in an idealized limit.

This chapter proceeds as follows: we begin by determining the electrostatic potential at one instant in time, then assume a cosine time dependence and derive the pseudopotential. We then analyze the pseudopotential to determine trap location, depth, and secular frequency, and we make use of this information to indicate an optimal design for the experimental trap. We then give an idea of some typical values for a realistic experiment, and compare those to values for a conventional three dimensional linear trap.

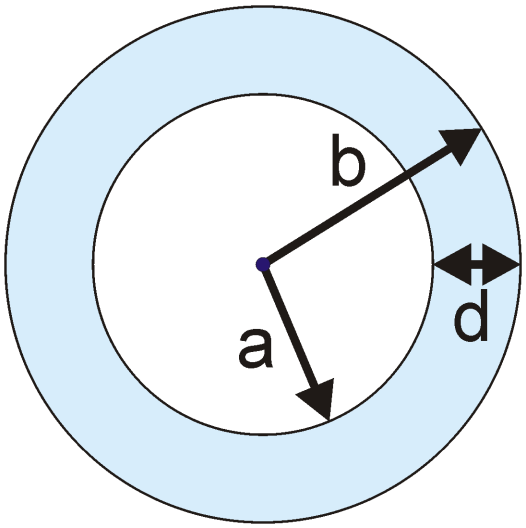

Figure 4-1: Top view of the point planar trap. The shaded region $a < \rho < b$ is at a potential $V\cos(\Omega t)$, while the unshaded regions $\rho < a$ and $\rho > b$ are at ground.

4.1 Electric potential

This section follows the discussion in [SGA+05] of a Penning trap in a planar configuration. Since a Penning trap uses an electric quadrupole potential to confine ions axially, the results for such a potential can be carried over directly, considered at one instant in time, then inserted into the pseudopotential formula to characterize a Paul trap.

The electrode configuration for the point trap is shown in Fig. 4-1, as seen from above. The idealizations made in this treatment are that there is no space between RF and ground electrodes, that the outer ground plane extends to infinity, and of course that there are no other elements contributing to the potential. For the following discussion we will use the coordinates (z, ρ) to denote the axial (vertical) and radial (horizontal) directions, respectively.

The electric potential for $z > 0$ is given by the expansion

$$\phi(z,\rho) = \int_0^\infty A(k) e^{-kz} J_0(k\rho)\, dk, \tag{4.1}$$

where the $A(k)$ are expansion coefficients and $J_0(k\rho)$ is the Bessel function of the first kind.

At $z = 0$, the trap surface, the potential is

$$\phi(0,\rho) = \begin{cases} 0 & , \quad \rho < a \\ V\cos(\Omega t) & , \quad a \leq \rho \leq b \\ 0 & , \quad \rho > b \end{cases} . \tag{4.2}$$

By imposing these potential constraints, we find that at $t = 0$

$$A(k) = V\left[bJ_1(kb) - dJ_1(kd)\right], \tag{4.3}$$

where $d = b - a$.

Inserting Eq. (4.3) into Eq. (4.1) and integrating will give us the potential at any point in space. If we consider the axial potential,

$$\phi(z,0) = \phi(z) = \int_0^\infty V\left[bJ_1(kb) - dJ_1(kd)\right] e^{kz}\, dk, \tag{4.4}$$

then the integral can be done analytically to give

$$\phi(z) = V\left[\frac{1}{\sqrt{1 + (d^2/z^2))}} - \frac{1}{\sqrt{1 + (b^2/z^2))}}\right]. \tag{4.5}$$

4.2 Pseudopotential

To obtain the pseudopotential along the z axis, we first find

$$\frac{d\phi}{dz} = V\left[d^2(d^2 + z^2)^{-\frac{3}{2}} - b^2(b^2 + z^2)^{-\frac{3}{2}}\right]. \tag{4.6}$$

Inserting this into the pseudopotential formula Eq. (2.6), we obtain

$$\Psi(z) = \frac{Q^2V^2}{4m\Omega^2}\left[d^2(d^2 + z^2)^{-\frac{3}{2}} - b^2(b^2 + z^2)^{-\frac{3}{2}}\right]^2. \tag{4.7}$$

4.2.1 Trap location and depth

First, we need to confirm that this pseudopotential is trapping, and for what ranges of b and d the trap exists. Specifically, we are interested in the trap location and trap depth, which can be investigated by finding pseudopotential maxima and minima. The derivative of the pseudopotential is

$$\begin{aligned}\frac{d\Psi}{dz} = -\frac{3zQ^2V^2}{2m\Omega^2} &\times \left[d^2(d^2+z^2)^{-\frac{3}{2}} - b^2(b^2+z^2)^{-\frac{3}{2}}\right] \\ &\times \left[d^2(d^2+z^2)^{-\frac{5}{2}} - b^2(b^2+z^2)^{-\frac{5}{2}}\right], \end{aligned} \tag{4.8}$$

which has a trivial root at $z = 0$ and other roots at

$$d^2(d^2+z^2)^{-\frac{3}{2}} - b^2(b^2+z^2)^{-\frac{3}{2}} = 0 \tag{4.9}$$

and

$$d^2(d^2+z^2)^{-\frac{5}{2}} - b^2(b^2+z^2)^{-\frac{5}{2}} = 0. \tag{4.10}$$

Rearranging, we find

$$z_0 = \sqrt{\frac{b^{4/3}\ d^{4/3}}{b^{2/3}+d^{2/3}}} \tag{4.11}$$

and

$$z_1 = \sqrt{\frac{b^{6/5}-d^{6/5}}{d^{-4/5}-b^{-4/5}}}\ . \tag{4.12}$$

Since $b > d > 0$ always, both the numerator and denominator in each of the radicals are always positive, so both roots always exist. Note that when b and d are equal, $b = d = \sqrt{2}z_0$, so the range of physical traps is

$$\frac{b}{z_0} > \sqrt{2}, \tag{4.13}$$

$$0 < \frac{d}{z_0} < \sqrt{2}. \tag{4.14}$$

We may wish to hold z_0 constant when designing our trap. Given Eq. (4.11), we can do this by solving for b in terms of z_0 and d, or vice versa. Substituting $\tilde{b} = b^{\frac{2}{3}}$

and $\tilde{d} = d^{\frac{2}{3}}$ into the definition of z_0, we find that

$$z_0^2 = \frac{\tilde{b}^2\tilde{d}^2}{\tilde{b}+\tilde{d}}, \tag{4.15}$$

or

$$z_0^2\tilde{b} + z_0^2\tilde{d} - \tilde{b}^2\tilde{d}^2 = 0. \tag{4.16}$$

This is a quadratic equation in $\tilde{b}$ or $\tilde{d}$. Writing $\tilde{b}$ in terms of $\tilde{d}$, then undoing our change in notation, we obtain

$$\frac{b}{z_0} = \frac{1}{2\sqrt{2}(d/z_0)^2}\left(1+\sqrt{1+4(d/z_0)^2}\right)^{\frac{3}{2}}. \tag{4.17}$$

Here we have chosen to scale lengths by z_0 to emphasize the scale-independence of the relationship. Since the derivation is totally symmetric under the interchange of b and d, we can also immediately write

$$\frac{d}{z_0} = \frac{1}{2\sqrt{2}(b/z_0)^2}\left(1+\sqrt{1+4(b/z_0)^2}\right)^{\frac{3}{2}}. \tag{4.18}$$

Note that since $z = z_0$ is the solution to Eq. (4.9), which occurs squared in Ψ,

$$\Psi(z_0) = 0. \tag{4.19}$$

Furthermore, since $\Psi \geq 0$, z_0 must be a minimum in the pseudopotential: it is therefore our trapping point. After some algebra, we find that

$$z_1^2 - z_0^2 = \frac{(b^2-d^2)(b^{\frac{4}{3}}-d^{\frac{4}{3}})}{b^{\frac{4}{3}}d^{\frac{4}{3}}(d^{-\frac{4}{3}}-b^{-\frac{4}{3}})(d^{-\frac{4}{5}}-b^{-\frac{4}{5}})}, \tag{4.20}$$

which is positive for $b > d > 0$. So, $z_1 > z_0$. Since $\Psi(z_0) = \lim_{z\to\infty}\Psi(z) = 0$, $\Psi(z_1)$ must be a local maximum.

We can define the trap depth as the difference in pseudopotential between the

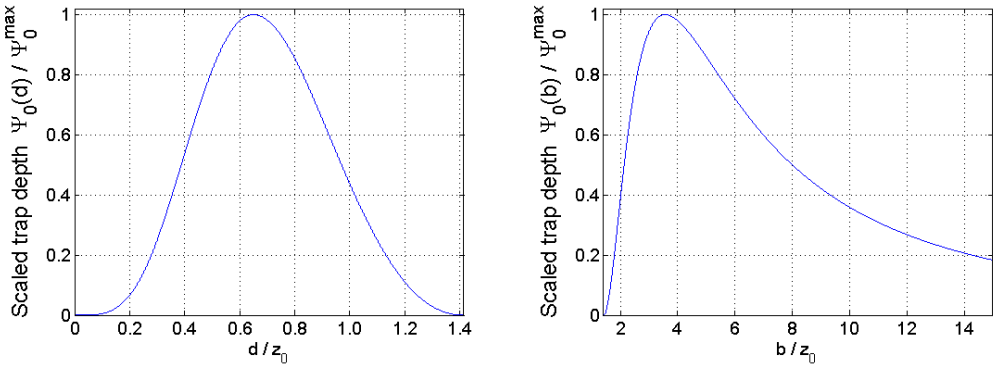

(a) (b)

Figure 4-2: Trap depth Ψ_0 plotted as a function (a) of d/z_0 and (b) of b/z_0, for constant z_0, using Eq. (4.17) and Eq. (4.18). The trap depth is scaled by its maximum value, as discussed in Sec. 4.3. Ψ_0 itself scales as $1/z_0^2$.

escape point z_1 and the trap point z_0:

$$\Psi_0 = \Psi(z_1) - \Psi(z_0) = \Psi(z_1). \tag{4.21}$$

Since this is a local maximum of a nonnegative function, and therefore positive, a trap exists for all $b > d > 0$. Note that for a given b/z_0 and d/z_0,

$$\Psi(z) \propto \frac{1}{z_0^2} \quad ; \quad \Psi_0 \propto \frac{1}{z_0^2}. \tag{4.22}$$

Trap depth Ψ_0 is plotted as a function of b and d, for fixed z_0, in Fig. 4-2. The plots are scaled vertically by the maximum value of Ψ_0: see Sec. 4.3. The plots are of the same function: b and d are interchangeable in every formula in which they appear. The function is simply plotted over different ranges due to the physical constraint.

4.2.2 Secular frequency

We can expand the pseudopotential to second order about the minimum at z_0, obtaining

$$\Psi(z) \approx \frac{1}{2} m\omega_z^2 (z - z_0)^2, \tag{4.23}$$

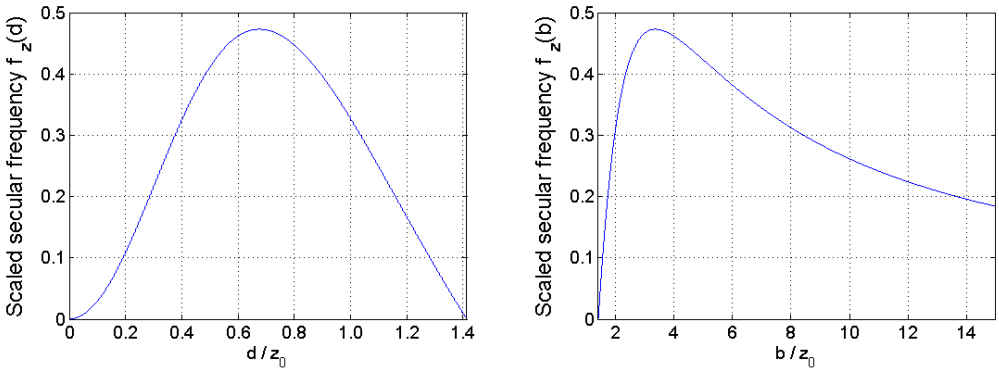

(a) (b)

Figure 4-3: Scaled secular frequency f_z plotted as a function (a) of d/z_0 and (b) of b/z_0, for constant z_0, using Eq. (4.17) and Eq. (4.18). Note the correlation with scaled trap depth (Fig. 4-2): both functions reach their maxima at the same points, and have similar shapes.

where

$$\omega_z = \frac{QV}{\sqrt{2}m\Omega z_0^2} f_z \tag{4.24}$$

is the secular frequency in the z direction, and

$$f_z = \frac{3\, b^{\frac{2}{3}}\, d^{\frac{2}{3}}\, |b^{\frac{2}{3}} - d^{\frac{2}{3}}|\, (b^{\frac{2}{3}} + d^{\frac{2}{3}})^2}{(b^{\frac{4}{3}} + b^{\frac{2}{3}}\, d^{\frac{2}{3}} + d^{\frac{4}{3}})^{\frac{5}{2}}} \tag{4.25}$$

is the scaled secular frequency from Eq. (2.8). We can then use Eq. (2.10) to compute the Mathieu stability parameter q_z:

$$q_z = \frac{2QV}{m\Omega^2 z_0^2} f_z. \tag{4.26}$$

Scaled secular frequency f_i is plotted as a function of b and d, for fixed z_0, in Fig. 4-3. As with trap depth (Fig. 4-2), these are the same function plotted over different ranges. Note the similarity to Fig. 4-2: the secular frequency reaches a maximum value where the trap depth reaches its maximum.

4.3 Optimization

Now that we know a trap exists, and a few things about it, what dimensions should we build the trap to? This will of course depend on the application. One reasonable goal would be to minimize anharmonic terms in the pseudopotential, while another would be to maximize trap depth. Here we investigate the latter.

In order to maximize $\Psi(z_1)$, we should vary b or d and look for stable points in the function. However, currently b and d are independent variables, and together they set a scale for the trap, which we would like to remove. A more natural choice of scale than either b or d is the trapping height z_0. So, making use of Eq. (4.18), and setting $z_0 = 1$, we can hide this scaling factor without any laborious changes in notation, provided we put it back in using dimensional analysis once our results are in hand.

Taking the derivative of the trap depth with respect to b, we obtain

$$\begin{aligned}\frac{d\Psi(z_1)}{db} &= \left[d^2(d^2+z_1^2)^{-\frac{3}{2}} - b^2(b^2+z_1^2)^{-\frac{3}{2}}\right] \\ &\quad \times \left[2d\frac{dd}{db}(d^2+z_1^2)^{-\frac{3}{2}} - \frac{3}{2}d^2(d^2+z_1^2)^{-\frac{5}{2}}(2d\frac{dd}{db}+2\frac{dz_1^2}{db}) \right. \\ &\quad \left. - 2b(b^2+z_1^2)^{-\frac{3}{2}} + \frac{3}{2}b^2(b^2+z_1^2)^{-\frac{5}{2}}(2b+2\frac{dz_1^2}{db})\right].\end{aligned} \tag{4.27}$$

The first factor has a zero at $z_1 = z_0$, which never occurs, so is of no concern to us. Looking at the second factor and using the definition of z_1 Eq. (4.10), we can eliminate the terms proportional to $\frac{dz_1^2}{db}$. That leaves us with the following equation to solve:

$$d\frac{dd}{db}(d^2+z_1^2)^{-\frac{5}{2}}(2z_1^2-d^2) - b(b^2+z_1^2)^{-\frac{5}{2}}(2z_1^2-b^2) = 0. \tag{4.28}$$

Inserting Eq. (4.18) into Eq. (4.28) and solving numerically, then inserting appropriate factors of z_0, we obtain

$$b = 3.57668\ z_0, \tag{4.29}$$

$$d = 0.651679\ z_0, \tag{4.30}$$

$$z_1 = 1.95797\ z_0, \tag{4.31}$$

$$f_i = 0.471565, \tag{4.32}$$

$$\tag{4.33}$$

and

$$\Psi_0^{max} = 0.0197034\ \frac{Q^2V^2}{4m\Omega^2 z_0^2} \tag{4.34}$$

$$= 5.56782 \times 10^{-3}\ q_z^2 m\Omega^2 z_0^2 \tag{4.35}$$

The planar point trap shown in Fig. 1-1(f) has this optimal scaling.

4.4 Example trap

To illustrate some typical values of the parameters of a point trap, recall the example from Chapter 2 of $^{88}Sr^+$ in a trap with $r_0 = 500$ μm and $V = 500$ V. Choosing the optimal design for $z_0 = 500$ μm gives us $a = 1.46$ mm, $b = 1.79$ mm, and $d = 0.33$ mm. If we choose to operate at $q_z = 0.2$, then our desired $\Omega = 2\pi \times 16.2$ MHz, which gives us a secular frequency $\omega_z = 2\pi \times 1.14$ MHz and a trap depth $\Psi_0 = 0.52$ eV. The pseudopotential for this trap is plotted in Fig. 4-4 (thick curve). The escape path is to the right on the curve, vertically upward in the apparatus.

By comparison, suppose we operated a linear trap with hyperbolic electrodes (Fig. 1-1(b)), with a distance from the trap point to the electrodes $r_0 = 500$ μm. We assume the same ions, V and q. We would then drive with $\Omega = 2\pi \times 23.6$ MHz, and the trap would have a radial secular frequency $\omega_{x,y} = 2\pi \times 1.67$ MHz, and a trap depth $\Psi_0 = 12.5$ eV. Since the potential for a hyperbolic trap is purely harmonic, the escape path is to one of the electrodes at $r = r_0$.

The point planar trap therefore has a potential with approximately 2/3 the curvature of a comparable linear hyperbolic trap, but only 1/24 the trap depth. However, this is a better ratio of 1/100 that the linear planar trap achieves, according to Chiaverini *et al.* [CBB+05].

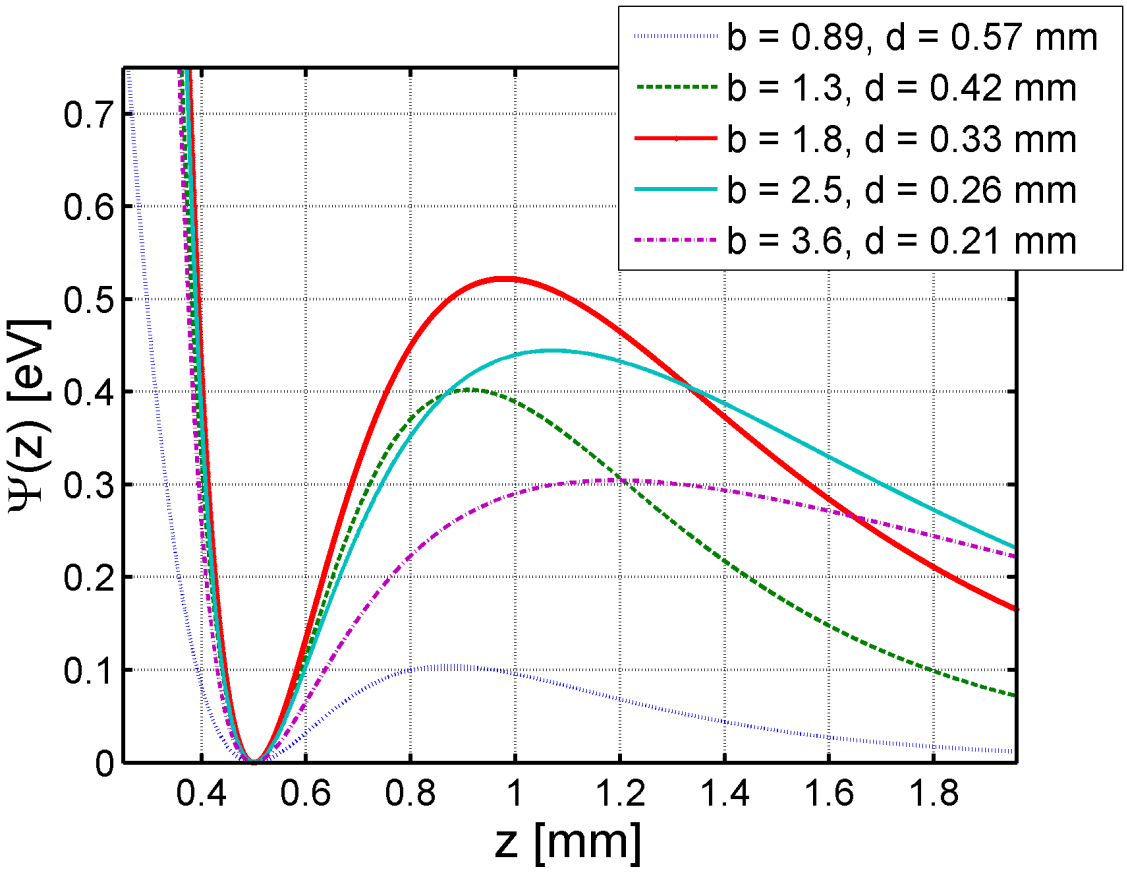

Figure 4-4: Pseudopotential plot for optimal and sub-optimal traps for $^{88}Sr^{+}$. The thick red line ($b = 1.8$mm)is the optimal trap, and the other lines are traps with b scaled up and down by factors of $\sqrt{2}$ and 2, with d computed to maintain $z_0 = 0.5$ mm. Note from Fig. 4-2 that since the $\Psi_0(b)$ curve is steeper on the left side, traps that were scaled down in b suffered more in trap depth. The trap is off the left side of the plot at $z = 0$; the escape path is to the right (upward).

Chapter 5

Experimental Method: Pressure Measurement with the Point Planar Trap

Now that we have characterized the point trap from a theoretical standpoint, we can outline its intended application as a pressure gauge. First, we discuss the mechanism by which we propose to determine pressure using macroscopic ions, then go on to describe the experimental apparatus and procedure.

5.1 Pressure measurement

In the movement operations described in Sec. 3.3.3, ion maximum speed was shown to be inversely proportional to chamber pressure. Furthermore, the displacement of the ion from its final position decreased monotonically to zero (Fig. 3-11). These features are consistent with overdamped motion, and constitute one method of pressure measurement using these macroscopic ions.

At lower pressures, we would expect the character of the ion motion to change, and the ion to oscillate about its final position at something close to the secular frequency before coming to rest. The decay time of this 'ringing' should indicate the background gas pressure. This second method of pressure measurement should be

useful at much lower pressures that those attained in the linear trap apparatus.

This section proceeds as follows: we begin by describing the transient motion of an ion in the trap. We then draw from the aerodynamic drag formulas in Sec. 2.3 to obtain a relationship between the damping time and the pressure.

5.1.1 Damped harmonic oscillator

Ions in the point trap experience a locally harmonic pseudopotential characterized by the secular frequency, and the drag from the background gas takes the form of viscous damping. This allows us to write equations of motion for the ions in a damped harmonic oscillator form. For this analysis we will disregard the actual direction of the ion motion, calling it simply x.

The forces on the ion are $F_{net} = F_{trap} + F_{drag}$, where

$$F_{net} = m\ddot{x} \tag{5.1}$$

$$F_{trap} = -m\omega_x^2 x \tag{5.2}$$

$$F_{drag} = -m\gamma\dot{x}. \tag{5.3}$$

The equation of motion for the ion is therefore

$$\ddot{x} + \gamma\dot{x} + \omega_x^2 x = 0. \tag{5.4}$$

Guessing a solution of the form $x = Ae^{-kt}$, we find that

$$k = \frac{\gamma}{2} \pm \sqrt{\left(\frac{\gamma}{2}\right)^2 - \omega_x^2}. \tag{5.5}$$

We intend to operate in the underdamped regime, and are interested only in the exponentially damped component of the solution, and therefore the real part of k:

$$\mathrm{Re}(k) = \tau^{-1} = \frac{\gamma}{2}. \tag{5.6}$$

5.1.2 Damping coefficient and pressure

Combining Stokes' law Eq. (2.17) with the approximate version of the Cunningham correction factor for large Knudsen number Eq. (2.23), then following the analysis of Knudsen number in Sec. 2.3 we obtain

$$\gamma = \frac{6\pi\mu R}{1.648 m K n} \tag{5.7}$$

$$= \frac{6\pi\sqrt{2}\rho\sigma\mu R^2}{1.648 m} \tag{5.8}$$

$$= \frac{6\pi^2\sqrt{2}\mu d^2 R^2 P}{1.648 m k T}. \tag{5.9}$$

Modeling the ion as a sphere of density ρ_m and radius R, we obtain $m = \frac{4}{3}\pi R^3 \rho_m$ and

$$\gamma = \frac{9\pi\mu d^2 P}{1.648\sqrt{2} R \rho_m k T} \tag{5.10}$$

Inserting this into Eq. (5.6) and solving for the pressure,

$$P = \frac{1.648 \cdot 2\sqrt{2} R \rho_m k T \tau^{-1}}{9\pi\mu d^2}, \tag{5.11}$$

or collecting all the calculated terms together into a constant β,

$$\beta = \frac{1.648 \cdot 2\sqrt{2} R \rho_m k T}{9\pi\mu d^2}, \tag{5.12}$$

$$P = \beta\tau^{-1}. \tag{5.13}$$

5.2 Experimental apparatus

In this section, we discuss the trap's design and construction in detail, the high vacuum environment used, and our source of ions and loading method. Our methods for observation and and control of ions remain largely the same as in Sec. 3, but we will briefly review these as well.

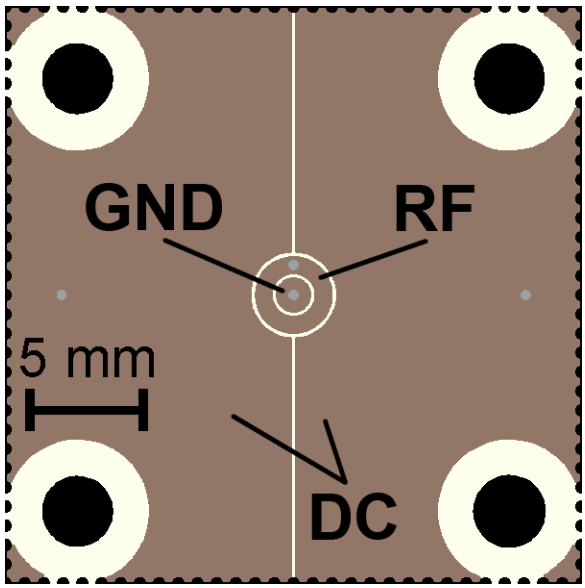

Figure 5-1: Top view of the point trap. The segmented ground plane allows for DC control of ion position within the trap. Electrical connections are made via four solder pads on the underside. The connecting vias are filled with solder (grey dots) to maintain the symmetry of the trap electrodes. Four mounting holes allow the trap to be mounted on standoffs in the vacuum chamber (see Fig. 5-3). This trap was fabricated on a single board along with many other point traps of varying dimensions, all laid out in an array; the perforated edges allowed it to be cut out from the array.

5.2.1 Trap materials and dimensions

Like the linear trap, the point planar trap is a PCB made using standard techniques. Figure 5-1 shows a top view of the trap. The electrodes are bare copper, and the substrate is Rogers 4350B, a microwave laminate with better vacuum compatibility than GML-1000. The electrode layout is as described in Chapter 4, with a central dot at ground, a concentric RF ring, and a large ground plane outside. The ground plane is segmented into two halves to allow for DC control. Electrical connections are made by solder pads on the bottom of the board, with vias connecting to the top. To avoid distortion of the trap potential, the via holes are filled in with solder. The width of the central dot is 1.5 mm, the width of the RF electrode is 0.76 mm, and electrodes are separated from each other by 0.18 mm. The entire trap is one square inch. Once again we do not use fully optimized electrode sizes as described in Sec. 4.3, in this case because the trap was selected from an array of prefabricated point traps with

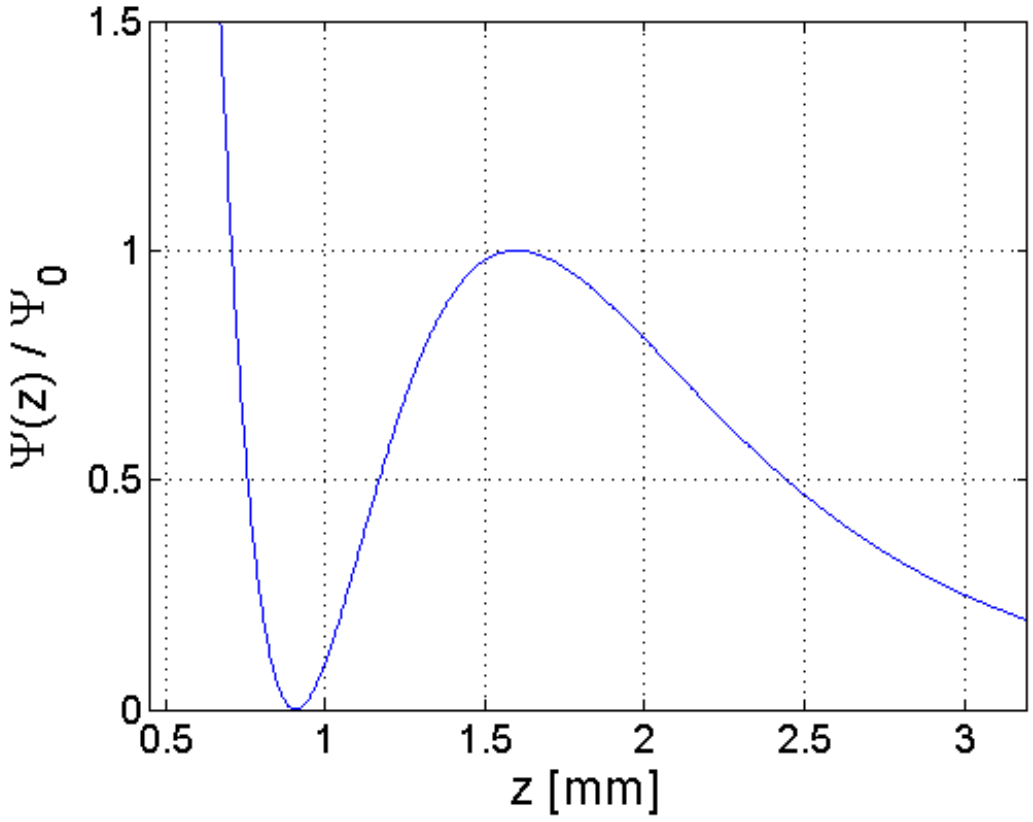

Figure 5-2: Pseudopotential of the point trap used in this experiment along the vertical central axis. The trap minimum is located at $z_0 = 0.91$ mm, and the escape point (local maximum) at $z_1 = 1.6$ mm. We estimate a trap depth $Psi_0 = 3.8$ eV in Sec. 5.2.3.

varying dimensions, as the one with the greatest depth.

Given the widths of RF and ground electrodes and the space between them, we obtain the theory parameters $a = 0.85$ mm, $b = 1.8$ mm and $d = 0.94$ mm. A plot of the pseudopotential along the z (vertical) axis is shown in Fig. 5-2. We calculate a trapping height $z_0 = 0.91$ mm, an escape point $z_1 = 1.6$ mm, and a scaled trap depth

$$\tilde{\Psi}_0 = \frac{4m\Omega^2 z_0^2}{Q^2 V^2}\Psi_0 = 7.2 \times 10^{-3}, \tag{5.14}$$

which is 36% of the optimal value. In Sec. 5.2.3 we discuss the trap depth and secular frequency, which we infer from the trap's operational parameters.

5.2.2 Ion source

Matrix-assisted laser desorption ionization (MALDI) provides ions to the trap. This technique involves the use of laser ablation, where short pulses of intense laser light heat a small patch of material and vaporize it. The material exits in a plume perpendicular to the surface, consisting of neutral and ionized species of varying size, and free electrons. MALDI makes use of a matrix of material in which the particles of interest (analyte) are suspended [KBBH87, BCS89]. The purpose of the matrix is to absorb the majority of the pulse energy and evaporate, freeing ionized but undamaged analyte particles in the process. The presence of acids, bases or salts in the matrix assist in chemically ionizing the analyte particles in much the same way as in ESI. This technique is widely used in the mass spectrometry of proteins and other sensitive biomolecules.

Our ablation light source is a Continuum Minilite II Q-switched neodymium: yttrium-aluminum-garnet (YAG) laser, frequency tripled from 1064 nm to 355 nm. Its output energy is 8 mJ per pulse, and the pulse width is $\sim$4 ns. Our analyte particles are the same 0.44 μm diameter aminopolystyrene microspheres as used in Chapter 3. Following [CPK$^+$02b], we add the microspheres to a saturated solution of picolinic acid in water, and air dry the mixture on our target. The resulting matrix is brittle and porous, and breaks down easily when subjected to focused pulses from the YAG. We can obtain ions in the trap even when the YAG is in a low energy alignment mode with 0.5 mJ pulse energy, particularly with a fresh target. However, in this experiment we operate at the full energy of 8 mJ to increase the yield of ions per pulse.

In this experiment we load directly into the planar trap without using a four rod trap for delivery. Ablated material can and does contaminate the trap surface, but the area of exposed dielectric is small compared to that in the linear trap, the amount of material produced by ablation is small compared to that produced by ESI, and there is no conductive liquid to short trap electrodes together. Furthermore, since MALDI can be performed at any pressure, we have no need to interface to an ion

source outside the vacuum chamber.

5.2.3 Trap environment and operating parameters

Figure 5-3 shows the experimental apparatus. The vacuum chamber is a Kimball Physics spherical cube, sealed with O-rings rather than copper gaskets to facilitate opening and closing the chamber when necessary. It will turn out that this does not limit the chamber base pressure. The YAG laser enters from the right, passing through a lens that focuses the beam onto the target, on the left side of the chamber. Classical (off resonant) scattering from a green (532 nm) diode laser is once again used to illuminate ions: this green beam passes underneath the ablation target from the left and skims the trap surface. We place a top plate above the trap, held at ground, the primary purpose of which is to shield from stray fields and increase trap depth. Electrical connections pass through a feedthrough underneath the trap, and a vacuum pump system is attached via the top flange. The electronics are identical to those used in Chapter 3 (see Fig. 3-5). In each of these experiments, we operate the trap at an RF amplitude of 400 V and a (linear) frequency of 1 kHz. Potentials on DC electrodes vary from 0-10 V.

Since the ion charge Q was not determined in this experiment, we do not know the actual trap depth or the Mathieu parameter q. However, we can proceed if we assume a reasonable value of $q = 0.2$. We then use the known mass of a single microsphere $m = 4.7 \times 10^{-17}$ kg, our applied voltage $V = 400$ V and frequency $\Omega = 2\pi \times 10^3$ Hz, to infer a charge $Q \approx 11\ e$, a charge to mass ratio $Q/m = 4.0 \times 10^{-10}\ e$/u, a trap depth $\Psi_0 = 3.8$ eV, and a secular frequency $\omega_z = 2\pi \times 70$ Hz. We should not expect the charge or charge to mass ratio of our ions to be the same as in Sec. 3.2, since we use a different method of particle generation and charging.

5.2.4 Measurement and control

Windows are attached to the remaining four sides of the cube to admit laser light and allow observation with cameras. A custom made lens system with a magnification

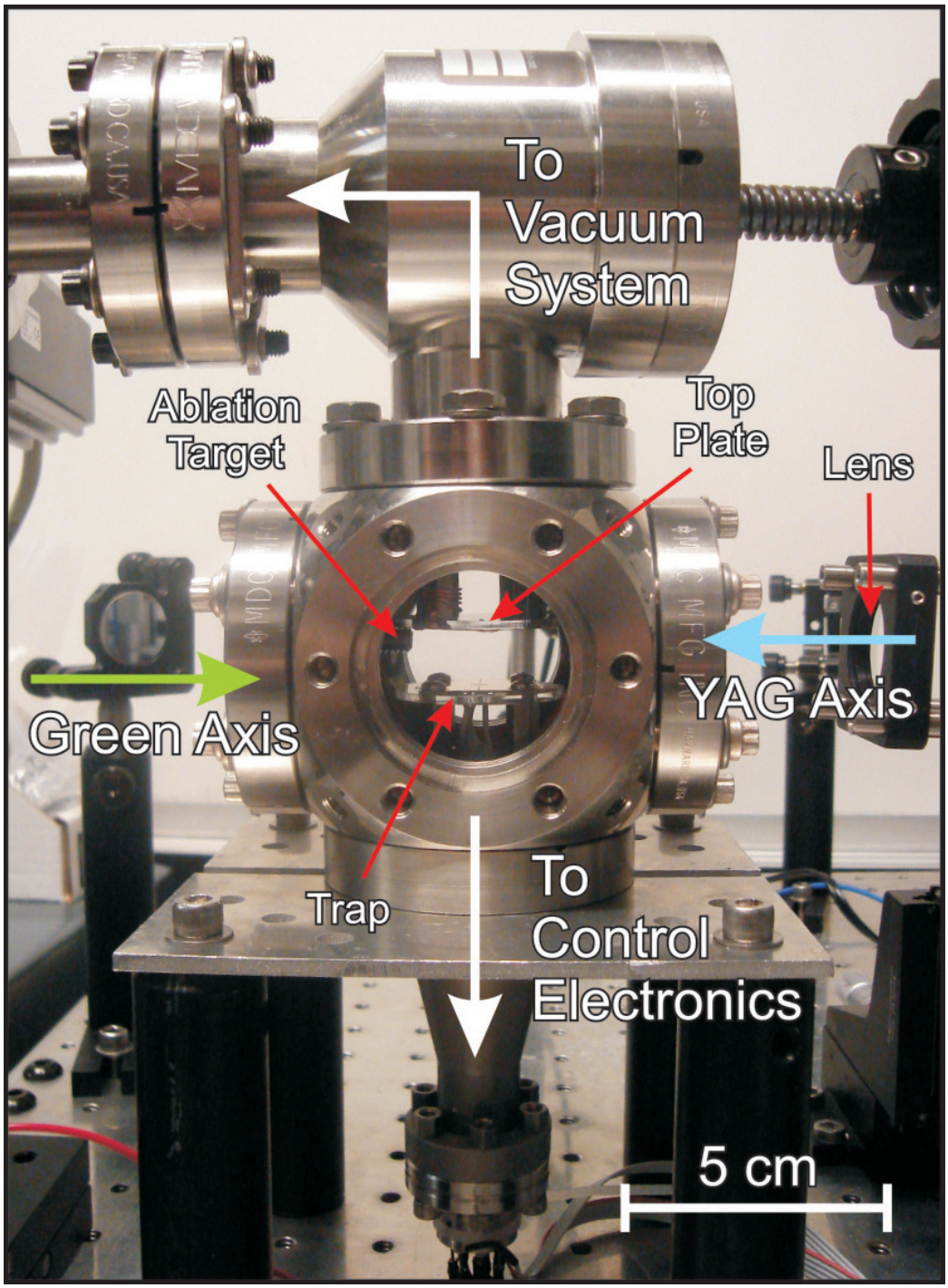

Figure 5-3: Photograph of the experimental apparatus. The ablation beam enters from the right to hit the target on the inside left. A green laser beam passes under the target to illuminate ions above the trap surface. Connections to vacuum and electronics are made at the top and bottom, and ions are viewed along the remaining axis. The trap is oriented such that applied DC voltages will kick ions to the left or right, perpendicular to the viewing axis.

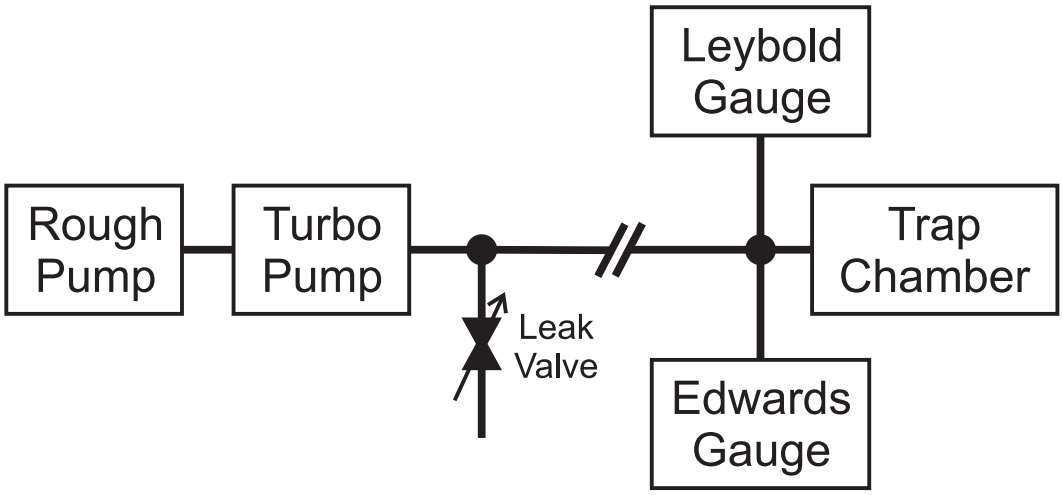

Figure 5-4: Vacuum system for the point trap. Two gauges provide pressure reference values, and a leak valve allows the pressure to be raised for loading or venting.

of approximately 2.75 attached to a 30 frame per second CCD camera is pointed in one of the remaining sides to record ion motion. This is a higher magnification than used in Chapter 3 and allows us to resolve ~ 15 μm features. The trap is oriented with the cut in the ground plane parallel to the camera axis, such that applied DC voltages will cause motion perpendicular to this axis.

A block diagram of the vacuum system is shown in Fig. 5-4. The chamber has two wide range gauges nearby to serve as a pressure reference, and is attached by a 75 cm hose to the pump station. The station contains a roughing pump and a turbomolecular pump, and a leak valve allows us to admit small amounts of air to raise the pressure in the chamber when necessary. The base pressure of this system is approximately 3×10^{-5} torr, and seems to be limited by the effectiveness of the seals near the pump and the pumping rate through the hose.

Though MALDI works at any pressure in that it produces ions in a plume from the target, those ions will not be trapped unless they lose energy. For that reason we do not load at the base pressure, but raise the pressure to the $10^{-2} - 10^{-1}$ torr range, and pump down further after loading [CPK+02b, PCC04]. This pressure range is chosen because it is high enough to slow the ions for trapping, but not so high as

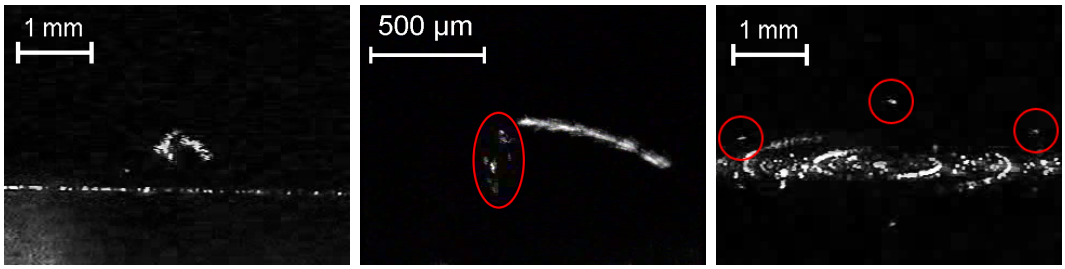

(a) (b) (c)

Figure 5-5: Side-view photographs of ions loaded into the point trap. (a) The ions tend to form an arc above the trap surface. Laser scatter from the trap surface is visible as a horizontal line. (b) We can trap both positive and negative ions at the same time, and distinguish them by applying DC fields. Here many positive ions for a bright arc, and two fast-moving negative ions are also faintly visible (circled). (c) Ions trap both inside and outside the RF ring. This view from slightly above the plane shows an ion inside and two ions outside the ring (circled). Laser scatter makes the trap electrodes visible, and reflections of the ions can also be seen in the polished surface.

to cause arcing between the trap electrodes or to significantly increase the settle time of the ablation plume. To load, we typically fire a train of 3-5 pulses at a rate of 10-15 Hz. This pulse train is fast enough to hit particles multiple times before they leave the beam path and settle onto the trap surface, and seems to increase ion yield compared to the same number of pulses spaced far apart.

When loading the trap, we notice that ions tend to form an arc over the center electrode (Fig. 5-5(a)). After many loads, when stray electric fields have begun to build up, we see only part of the arc as ions are pushed to one side of the trap region. Sometimes we see two crystals at opposite ends of the trap, and by applying DC potentials and observing the displacement of these crystals we find that the one is made up of positive ions and the other made up of negative ions (Fig. 5-5(b)). Negative ions are typically rarer than positive ions in this apparatus. We also find ions present between the RF ring and the outer ground plane (Fig. 5-5(c)): if many ions are captured here, they form an outward-pointing arc.

Once the trap is loaded, we get rid of any ions we do not want, such as those trapped outside the RF ring, or any negative ions. We try to obtain a small crystal of just a few (2-4) positive ions. We pump down to the turbo base pressure, and apply

a regular sequence of alternating step-function voltages on the DC electrodes, to kick the ions to the left or right and induce the transient ringing motion. This motion is recorded by the camera, and the pressure values displayed by the two gauges are recorded simultaneously. We shut off both pumps to eliminate vibrations, a source of ion heating, and slowly leak air into the chamber in order to record the ringing motion over a range of pressures. Once we reach pressures of 5×10^{-2} torr and higher, the damping time is so fast that the camera is unable to track it, so we stop and either pump down or reload to repeat the experiment.

Chapter 6

Experimental Results: Pressure Measurement with the Point Planar Trap

Measurements described in Sec. 5.2 were carried out in eight separate runs. In each run, a few (2-4) positive ions were present in the trap, organized into a loosely spaced crystal, and the ions exhibited transient oscillations when step potentials were applied to the DC electrodes. Each run applied between 15 and 40 such step potentials. Due to the large volume of data collected, only representative plots and figures will be given here. A review of the complete data sets for each of the eight experiments can be found in Appendix A.

This chapter proceeds as follows: we begin with a discussion of the analysis of the frame data. This analysis produces widths and heights of the collection of ions as a function of frame number (time). We then discuss the fitting of this size data to extract decay time constants. From these decay time constants we calculate the pressure, and compare the calculated pressure to that measured by the gauges. We then compare disparate pressure gauge readings to each other in an attempt to find a best value of pressure, against which we can compare our calculated values. Once this best value is obtained, we finish with a study of the correlation between the pressure calculated from ion motion and that indicated by the gauges, and discuss the results.

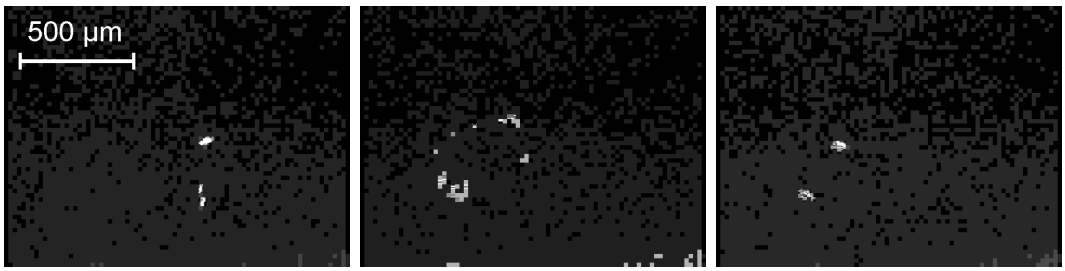

(a) (b) (c)

Figure 6-1: Sequence of three images of the motion of two trapped ions. Levels have been adjusted to aid viewing. (a) Ions are at rest just before a step potential is applied. (b) Ions are executing large amplitude oscillations about a new equilibrium point just after the step potential is applied. (c) Ions are at rest at the new equilibrium point after a few seconds.

6.1 Processing of video frames

The eight ringing experiments produced a combined total of 1.23 GB of video data. Converting this video into image frames is a relatively simple task in MPlayer[1], and we are then left with a sequence of ∼125,000 images. Figure 6-1 shows three such images: the first is just before a DC potential kick, the second just after, and the third some time after. It is clear from the video data that the ions are executing the kind of damped oscillations that we wish to see, and obtaining the time constants is just a matter of digesting the information appropriately.

Note that the ions appear smeared out in Fig. 6-1(b). Recall from Sec. 5.2.3 that we calculated a secular frequency $\omega_z = 2\pi \times 70$ Hz: the ringing oscillations occur at this frequency, whereas the camera frame rate is 30 Hz. Since the frame time is longer than the oscillation time, we will only see the exponentially damped envelope. This will be useful later, since we can safely ignore the ringing motion when performing our fits.

While it is appealing in principle to determine the amplitude of motion of each individual ion in the trap, in practice the ion trajectories often overlap in these frames, particularly during the most critical large amplitude oscillations. At times this makes the ions indistinguishable even to a human observer, and therefore hopeless for a

[1]http://www.mplayerhq.hu/ Copyright © 2000-2006 MPlayer team

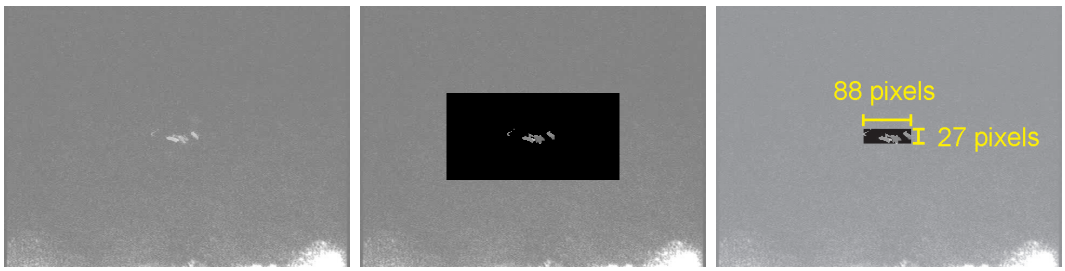

(a) (b) (c)

Figure 6-2: Processing of a video frame into width and height data. (a) The raw frame is extracted from the video sequence. (b) The image is cropped to remove areas with trap scatter, and a threshold is applied to separate ions from background. (c) Black edges are trimmed from the image, and the dimensions of the result are proportional to the dimensions of the ion crystal.

computer algorithm. We instead choose to look at the entire extent of the crystal, observing its return to equilibrium size after a potential kick. Since this does not affect the damping time constant, the treatment is just as valid.

Starting with a raw video frame, we use the command line image processing utility ImageMagick[2] to apply a threshold to the image, separating light areas from dark. We then crop the image to remove areas with scatter from the trap surface. Finally, we trim away the dark edges, resulting in image that has the same height and width as the crystal at that instant. Figure 6-2 illustrates this process. Once this image processing is complete, we can extract the height and width from the header information of the processed image files. We then plot the height and width versus frame number, and typically get something resembling Fig. 6-3.

6.2 Analysis of height and width data

With the numerical height and width data in hand, we may begin fitting to sections of the data that show exponentially damped behavior. The DC step potentials are timed at 15 second (450 frame) intervals. We start the fit at the peak of the motion, and fit between 10 and 400 frames. The thresholding operation introduces some noise onto the data in addition to any noise on the ions' motion itself, and at times the ringing

[2]http://www.imagemagick.org/ Copyright © 1999-2006 ImageMagick Studio LLC

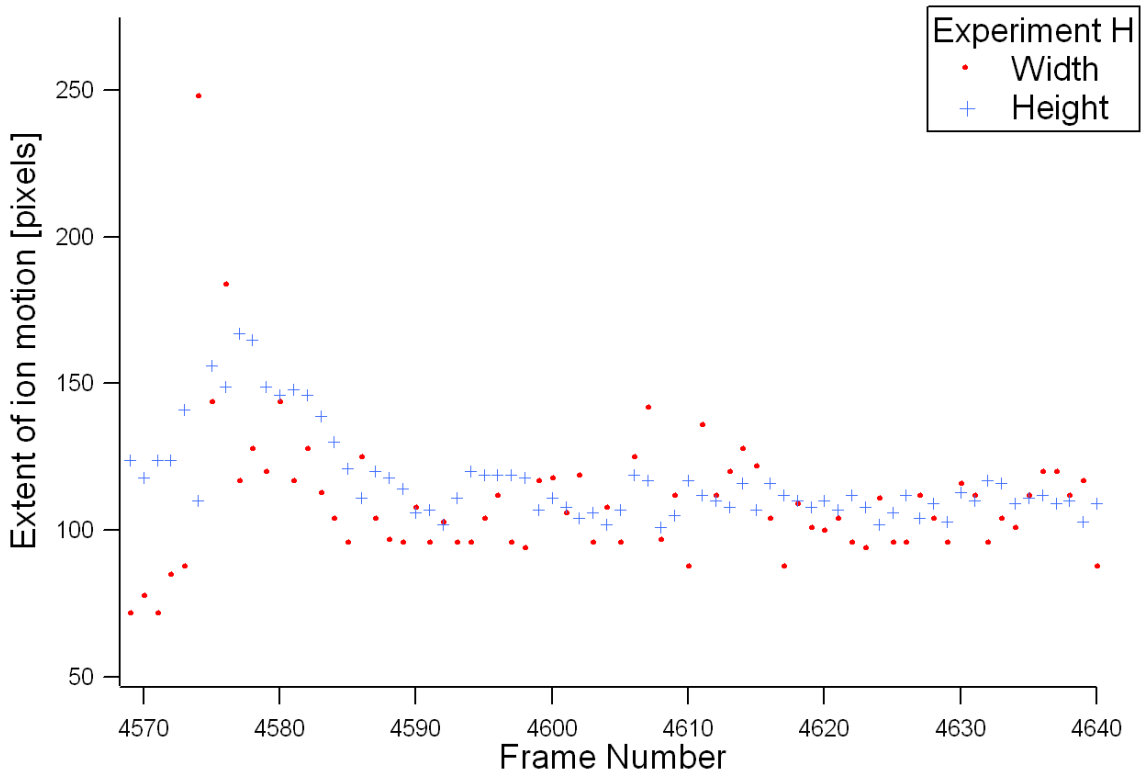

Figure 6-3: The height and width of each processed frame are plotted versus frame number. The images in Fig. 6-1 are taken from this region. The camera operates at 29.97 frames per second (NTSC), and one pixel is approximately 2.4 μm in the image plane. The former scale is important for the analysis; the latter is not. We fit a decaying exponential plus a constant to appropriate sections of this data, and discard all fit information except the time constant.

damps out so fast that there are only a few frames between maximum amplitude oscillations and rest. For these reasons, the fits sometimes have difficulty converging. We therefore try each fit several times with different numbers of data points in the fit. We also constrain the fit to reasonable values of amplitude, background level, and time constant. When the fitting is complete, we discard those fits that didn't converge or that violated the constraints, and combine the results together with their uncertainties to get a best value for the time constant. An uncertainty in this best value is derived from the spread in the time constants from different fits.

6.2.1 Pressure data

Having obtained a set of time constants, we can convert them to pressures using the parameter β (Eq. (5.12)),

$$\beta = \frac{1.648 \cdot 2\sqrt{2} R \rho_m k T}{9\pi\mu d^2}. \tag{6.1}$$

Here we use the properties of the microspheres ($R = 0.22$ μm, $\rho_m = 1050$ kg m^{-3}) and of the gas ($T = 295$ K, $\mu = 1.83 \times 10^{-5}$ Pa s, $d = 364$ pm) to obtain $\beta = 2.35 \times 10^{-4}$ torr s. We then calculate $P = \beta\tau^{-1}$ and plot these results along with the measured pressures. Figure 6-4 shows one such plot.

There are several things to note from this graph. First, some values of the calculated pressure are clear outliers: their far off values are accompanied by huge uncertainties. Such points are where the fitting algorithm had the most trouble. Second, the pressures exhibit a clear upward trend as the chamber is vented. Third, the behavior of the pressure gauges seems quite bizarre. They do agree somewhat with the calculated pressures at the higher end, but they disagree greatly with the calculated values, and with each other, and apparently with themselves, at lower pressures.

To understand what is going on here it's necessary to understand a bit about how these pressure gauges work. Each is a 'wide range' gauge, designed to cover as many orders of magnitude as possible. In order to claim accuracy as they do over ranges from 10^{-9} to 10^{2} torr, they combine a cold or hot cathode ion gauge, sensitive to low pressures, with a Pirani gauge that is accurate at higher pressures. The jumps seen

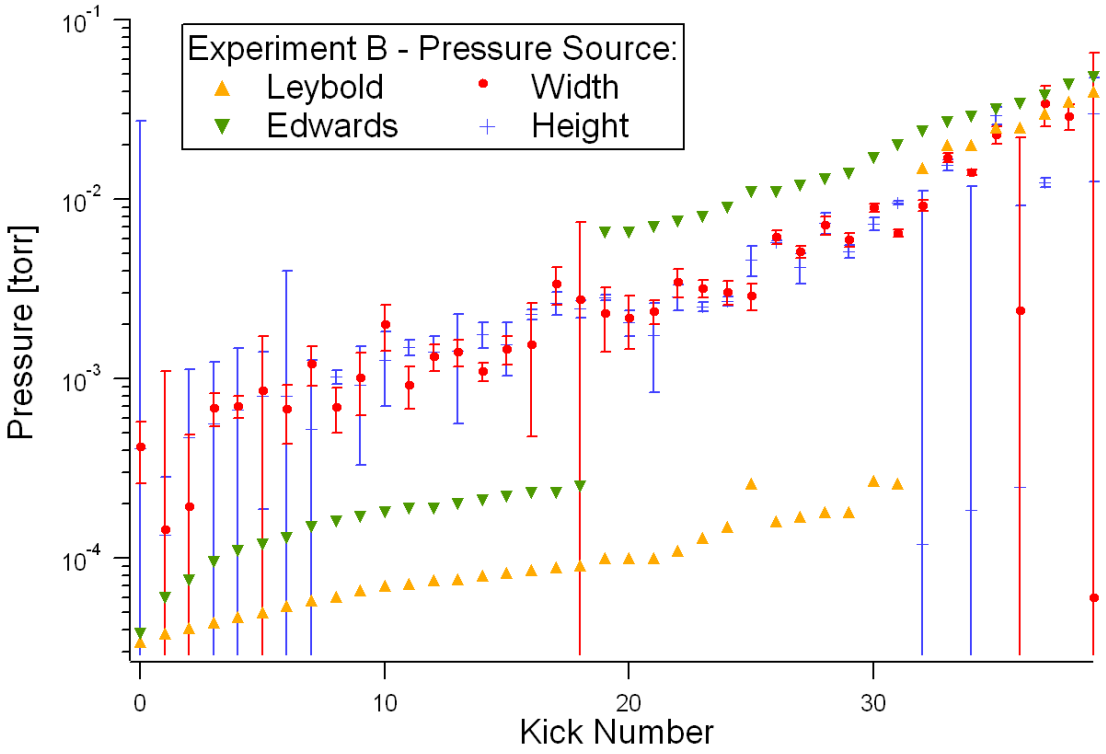

Figure 6-4: Sequential measurements of pressure as the trap chamber is slowly vented. Red dots and blue crosses are the values calculated based on ion ringing. Green and orange triangles are values reported by two wide range pressure gauges mounted right next to the trap (and each other). The jumps in reported gauge pressures are due to the gauges switching from ion gauge mode to Pirani mode.

in Fig. 6-4 are the transition points between the two modes in each gauge. Evidently, the ion gauges are not particularly well calibrated at the high end of their range.

In order to get some useful comparison between the calculated and 'actual' pressures, we perform a side experiment in which we compare readings of these two gauges with those of a third gauge that was not available for the ringing experiment.

6.2.2 Pressure gauge cross-calibration

The procedure here is quite simple: we connect three different models of wide range pressure gauge (Leybold IONIVAC ITR 90, Edwards WRG-S-NW25, and Alcatel ACC 1009) at the same point in the vacuum system, and vary the pressure while recording the value displayed by each gauge. Pressures are shown plotted against time in Fig. 6-5.

There is essentially no agreement between the gauges in the lower ranges. However, the Alcatel gauge does not show the jumps that the other gauges show, which may indicate that it is more accurate. Regardless of whether this gauge is in fact more accurate, a single smooth pressure curve is what we need to make comparisons to the ringing calculations, so we will attempt to reconstruct it using the data collected in Fig. 6-5. Figure 6-6 shows the Leybold and Edwards gauge readings versus the Alcatel reading. By fitting analytical curves to this data, we can use the readings from either of the two gauges in the ringing experiment to reconstruct the reading of the Alcatel gauge. The Leybold curve turns out to be easier to fit, and we obtain

$$\log_{10}(P_A) = \begin{cases} -1.57 + 1.02\ln(\log_{10}(P_L) + 4.50) & , \quad -4.5 < \log_{10}(P_L) \leq -3.53 \\ -1.6 & , \quad -3.53 < \log_{10}(P_L) \leq -1.71 \\ 0.086 + 0.985\log_{10}(P_L) & , \quad \log_{10}(P_L) > -1.71 \end{cases} . \tag{6.2}$$

This will give us a good value of the Alcatel gauge's expected reading only to the extent that the curves in Fig. 6-6 are reproducible from day to day.

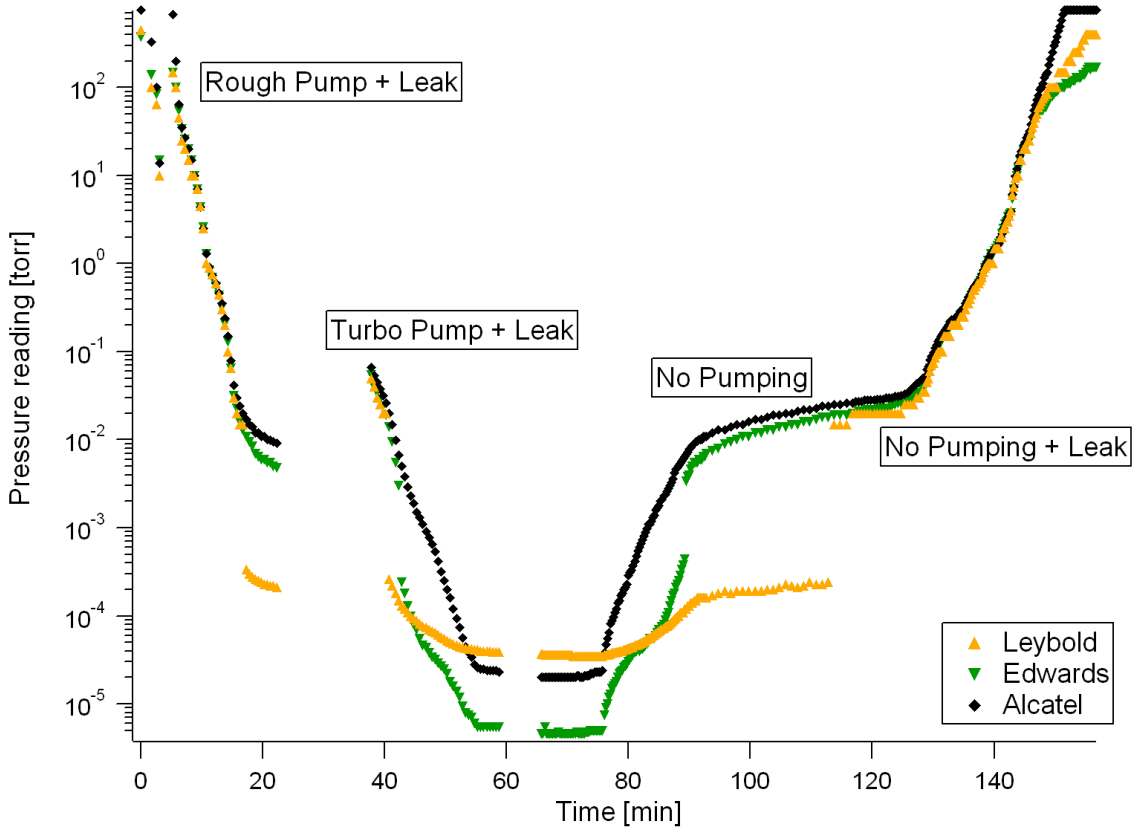

Figure 6-5: Readings of three different pressure gauges of the same pressure, plotted vs. time. Horizontal gaps are dead time between experiments; vertical gaps are significant, indicating a jump between modes. Note that all three gauges are in fairly good agreement while in Pirani mode (up to the 10^2 torr range, where Piranis become unreliable). The pressure is not varied in any very regular manner, so the shapes of the individual curves are not significant.

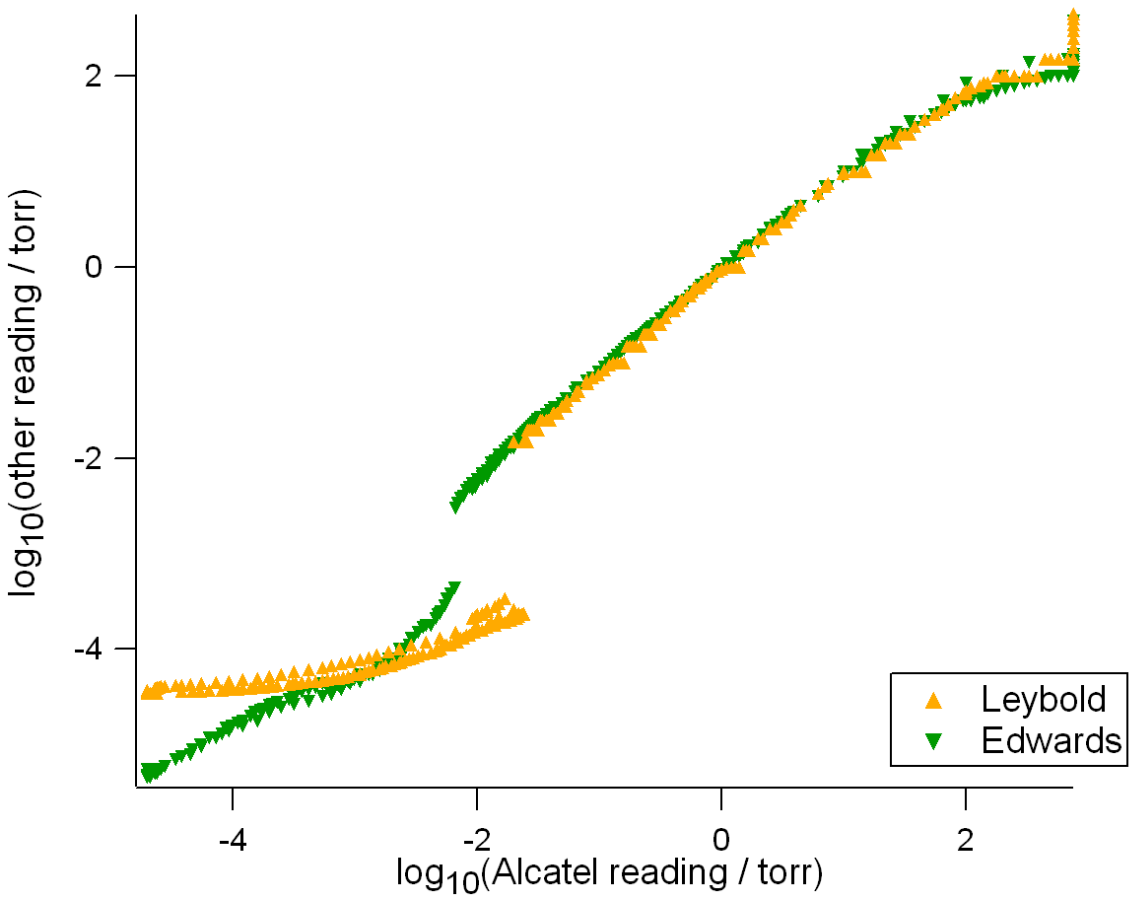

Figure 6-6: Data from Fig. 6-5 plotted again, treating Alcatel reading as the independent variable.

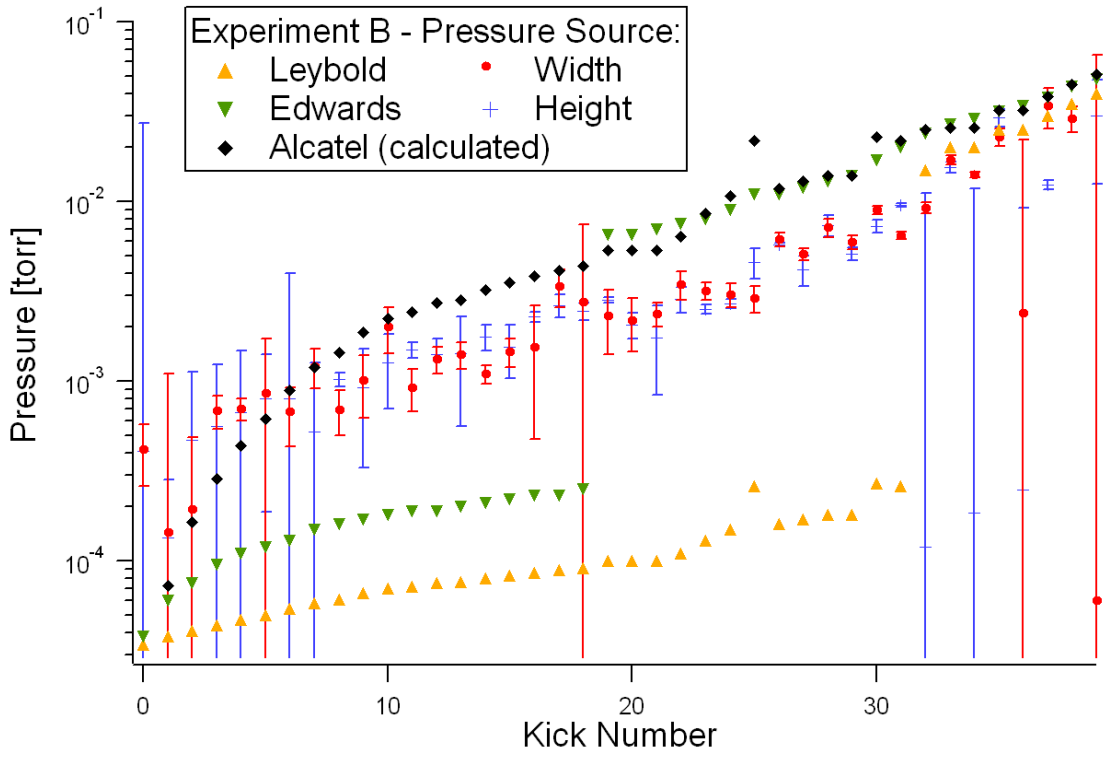

Figure 6-7: Pressure measurements and calculations from Fig. 6-4, with the addition of the reconstructed Alcatel gauge reading (black diamonds). Since the Leybold reading is used to calculate the Alcatel reading according to Eq. (6.2), fluctuations on the former show up on the latter.

6.3 Statistics

Figure 6-7 shows the data from Fig. 6-4 with the calculated Alcatel reading added in. To understand the agreement between the values, we perform two fits per data set, comparing the pressures calculated from ringing against the calculated Alcatel reading. First, we make a zero parameter fit, $f(x) = x$, and the goodness of this fit $\chi^2_{\nu,0}$ (reduced chi squared) indicates the degree of agreement between the values when no adjustments are made. Values close to 1 indicate the best agreement: larger values indicate either worse agreement or underestimated error, while values considerably less than 1 indicate overestimated error or too many fit parameters in the model. Then we perform a one parameter fit, $f(x) = Cx$, and $\chi^2_{\nu,1}$ here indicates the agreement between the values if we allow the scaling to float. This is equivalent to modifying

Expt.	ν	$\chi^2_{\nu,0}$	C	$\chi^2_{\nu,1}$
A	20	10.6	0.786	6.31
B	37	216	0.379	10.7
C	29	44.5	0.730	19.7
D	26	0.222	0.984	0.220
E	40	3.61	0.822	2.34
F	20	4.09	0.673	2.00
G	27	1.73	1.06	1.71
H	15	4.30	0.862	4.20

(a) Width

Expt.	ν	$\chi^2_{\nu,0}$	C	$\chi^2_{\nu,1}$
A	20	3.93	0.887	3.44
B	37	324	0.406	11.4
C	31	43.8	0.510	1.91
D	25	0.676	0.915	0.639
E	33	6.10	0.751	3.49
F	15	4.20	0.638	1.55
G	12	11.9	0.270	3.72
H	12	11.7	0.470	7.23

(b) Height

Table 6.1: Results of fits of pressure data derived from ringing against reconstructed Alcatel gauge reading. ν is the number of points in each fit, $\chi^2_{\nu,0}$ is the goodness of fit for the zero parameter fit, and C and $\chi^2_{\nu,1}$ are the parameter and goodness of fit for the one parameter fit. The values for (a) the width data and (b) the height data are comparable in most cases, except where there is considerable difficulty with exponential fit convergence and many values have to be thrown out (Experiments G and H, height).

Eq. (5.13) with an additional constant

$$P = C\beta\tau^{-1}, \tag{6.3}$$

then using a calibration to determine the parameter C empirically. The extra degree of freedom invariably gives better agreement, but how much χ^2_ν improves and how uniform the fit parameter C turns out to be from experiment to experiment can tell us something about possible systematic errors.

Fit parameters and goodness of fit are presented in Table 6.1. To get an idea of the repeatability of these experiments, we combine all the data together and plot versus measured pressure (Fig. 6-8). If ion size or other parameters change appreciably from one experiment to the next, that will affect the trend of the combined data. By performing the same fits here as were done on the individual experiments, we obtain the results given in Table 6.2.

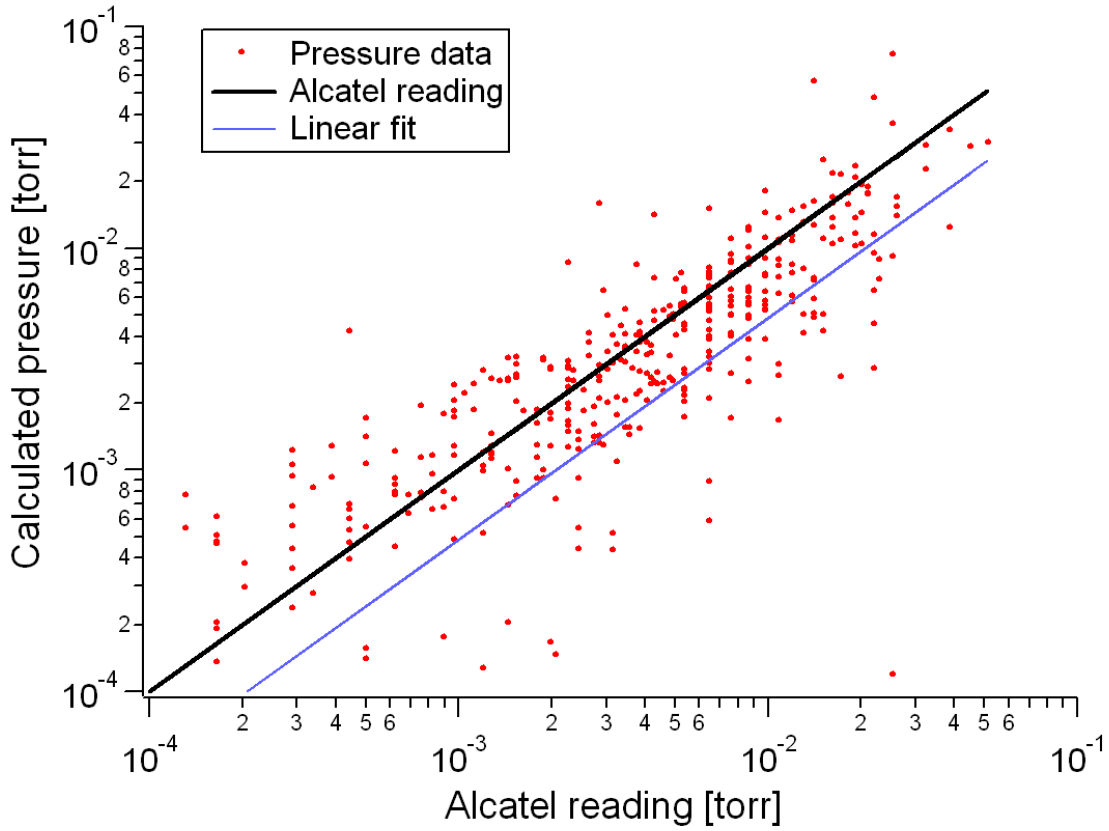

Figure 6-8: Combined pressure data with zero and one parameter fits shown. Fit results are given in Table 6.2. Error bars are not shown to reduce clutter.

ν	$\chi^2_{\nu,0}$	$C \pm \sigma_C$	$\chi^2_{\nu,1}$
399	59.76	0.4847 ± 0.0037	9.828

Table 6.2: Fit values for combined pressure data.

6.4 Discussion

It turns out that the data pressented from Experiment B in Fig. 6-7 has the worst agreement with gauge pressure, but that even so the calculated values agree with the gauge pressure as well as any of the gauges agree with each other. Plots of pressures for the other experiments are presented in Appendix A, and as indicated by Table 6.1, some show very good agreement with the gauge pressure.

Calibrating against a known pressure and then using that value to set the scale for the remaining measurements may be prudent if we are in doubt about any of the constants in Eq. (5.13). For example, we may be unsure of the actual size of the trapped ions R, since we could trap clusters of spheres, or microcrystals of the picolinic acid matrix. We also might be uncertain about the 'diameter' d of a gas molecule, particularly if the gas is of unknown composition: since this parameter occurs squared, the accuracy of the pressure is particularly sensitive to it.

While many of the χ^2_ν values we obtain here are not impressive, there is much that can be done in further experiments to improve precision. The random error in the calculated pressure values is dominated by the error in the fit parameter; the difficulty of fitting to the height and width data was discussed in Sec. 6.2, but is due to three main issues.

First, the ions do not remain completely still between kicks: quiescent secular motion can cause the crystal size can vary by as much as 100 pixels (240 μm). Stray electric fields seem to have a considerable effect on this: after the trap has been cleaned, ions tend to move all around the trapping region, but after many loads have accumulated some dust on the trap surface and charge on exposed dielectrics, the symmetry is broken and ions tend to move around much less, remaining pinned to one side of the trap.

The second contributor to the noise is the camera frame rate. The ringing curves we obtained typically had only a few points of large amplitude motion, making it difficult to determine the shape of the curve. Faster data acquistion would be very helpful, either using a faster frame rate camera or another measurement scheme such

as a slit mask imaged by a photodiode or photomultiplier tube.

The third noise contribution is from the data processing. The image data was stored on computer in real time, which is a very resource intensive task. The computer reduces the quality of the frames in order to keep up, introducing significant compression noise. This noise not only blurs out features of the ions, but can sometimes cause artifacts in dark areas of the picture. In order that the threshold operation does not pick up these bright spots, the threshold value must be increased, but this makes it more difficult to catch dim, fast moving ions, introducing additional noise at lower pressures. These issues could be helped either by devoting more computer resources to the data acquisition, or by increasing the contrast of the ions with the background.

Chapter 7

Conclusion

In this thesis, we have presented two types of planar ion trap, and using printed circuit boards and macroscopic particles to realize each, have demonstrated their operation and potential applications. We have addressed the challenges of ion loading in two ways, and our experiments in the linear trap constitute the first experimental demonstration of the basic ion movement operations in a planar geometry.

The challenge of loading ions into the linear trap was solved by coupling a traditional four rod trap to the planar trap. Ions with high kinetic energies were first loaded into the linear trap, and then offloaded into the planar trap, circumventing the relatively low trap depth and keeping the trap substrate clean. This method allowed us to load the planar trap with the efficiency of loading a traditional three dimensional linear trap.

We have also found that the addition of a charged conductive plane above the trap can be used to increase the trap depth at the cost of displacing the ions from the RF null. Though the latter is undesirable for atomic ion traps, the factor of 10 increase in trap depth can be immensely helpful while loading such traps, and the potential can then be lowered to reduce micromotion.

We were able to perform controlled movement of ions in the planar trap despite the low trap depth, and have performed the fundamental movement operations required for a multiple zone architecture: translation of single ions, splitting and joining chains of ions, and navigating around corners and through intersections. Before this work,

the potential at a cross intersection was thought to be too unstable to allow ions through.

Since we can use planar traps to produce a wide range of geometries, we then studied one useful geometry, the point design, for studying small collections of ions. We derived some useful analytical formulas for trap depth, secular frequency and optimal trap dimensions.

We addressed the challenge of planar trap loading again using a different technique, direct loading with MALDI. Though loading directly is less efficient than loading through a four rod trap, the implementation is more compact and much simpler to implement. The low trap depth was compensated by slowing the ions with buffer gas during loading and then pumping down for experiments.

We derived a simple relationship between pressure and a parameter of ion motion, the decay rate of damped secular motion. This relationship is affected by only two ion or trap dependent parameters; the ion radius and mass (or in this treatment, the radius and density). Other parameters depended on gas composition and temperature, which are considerations common to nearly all methods of measuring low pressures.

We then applied this relationship to determine pressure in a vacuum of 4×10^{-5} torr to 5×10^{-2} torr. Assuming that we loaded single microspheres, we achieved results that agreed with conventional gauge measurements with reduced chi squared $\chi^2_{\nu,0}$ values ranging from 0.222 to 324 with a median value of 5.20, with no experimental fit parameters required. When all the data was combined, we obtained a zero parameter $\chi^2_{\nu,0} = 59.76$. Adding a single fit parameter (which also eliminates the single sphere assumption) decreased this value to $\chi^2_{\nu,0} = 9.828$. Even in those experiments where $\chi^2_{\nu,0} > 40$, the accuracy was no worse than that of the gauges we employed as a check.

Planar ion traps are already emerging as a technology of major importance to quantum computing, with efforts underway to further miniaturize and integrate the design to a true chip trap [KPM$^+$05]. These design efforts make the planar trap an appealing technology for wider application, including the implementation as a pressure gauge studied here. The adaptability of the planar ion trap design is its greatest asset, and these traps show promise to adapt to new and widespread applications in

the coming years, just as ion traps in general have done since their inception.

Appendix A

Pressure Measurement Data

A.1 Frame by frame

This section contains all frame data for all experiments. Each frame is cropped, a threshold applied, and then trimmed so that the size of the resulting image is the extent of the ions. The heights and widths of the processed frames are then read in and plotted.

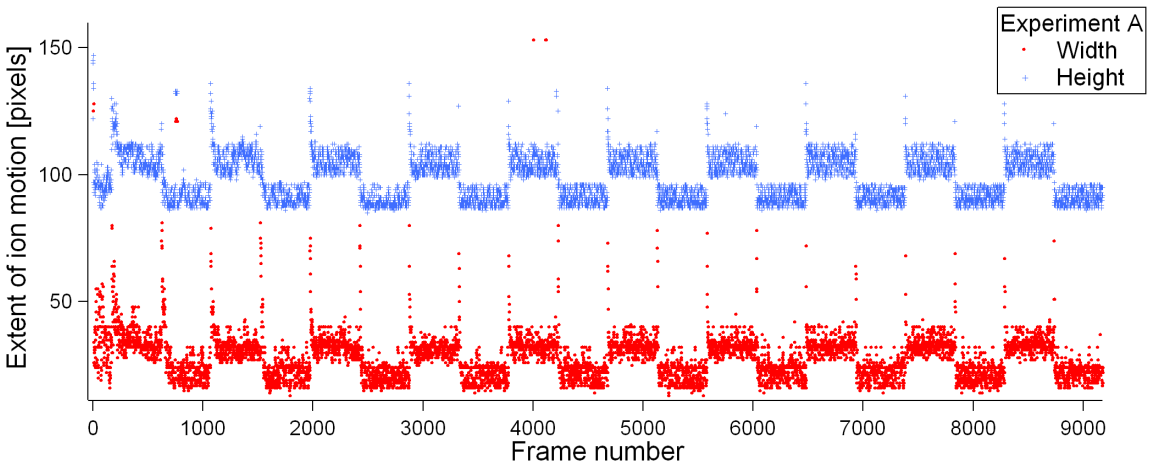

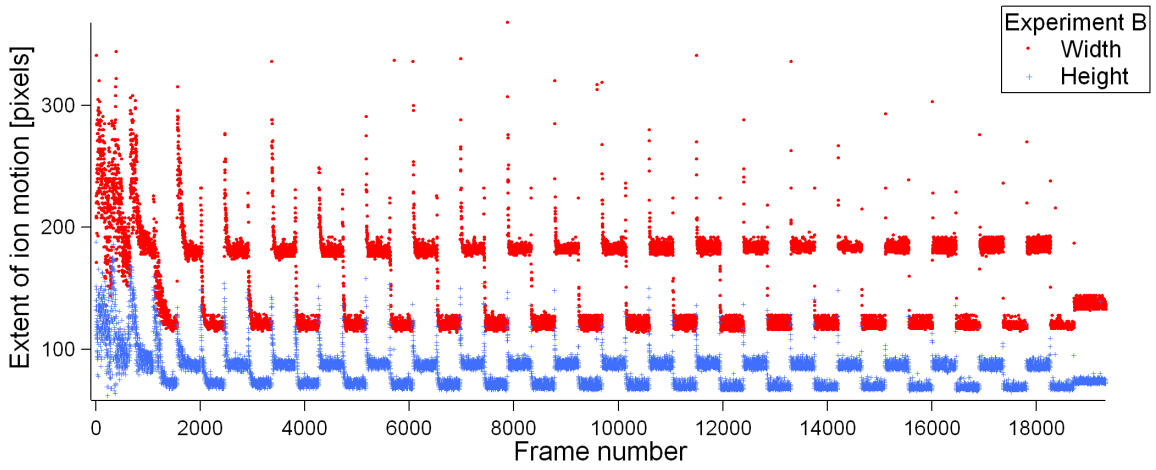
Experiment B
Width
Height
Extent of ion motion [pixels]
100
200
300
0
2000
4000
6000
8000
10000
12000
14000
16000
18000
Frame number

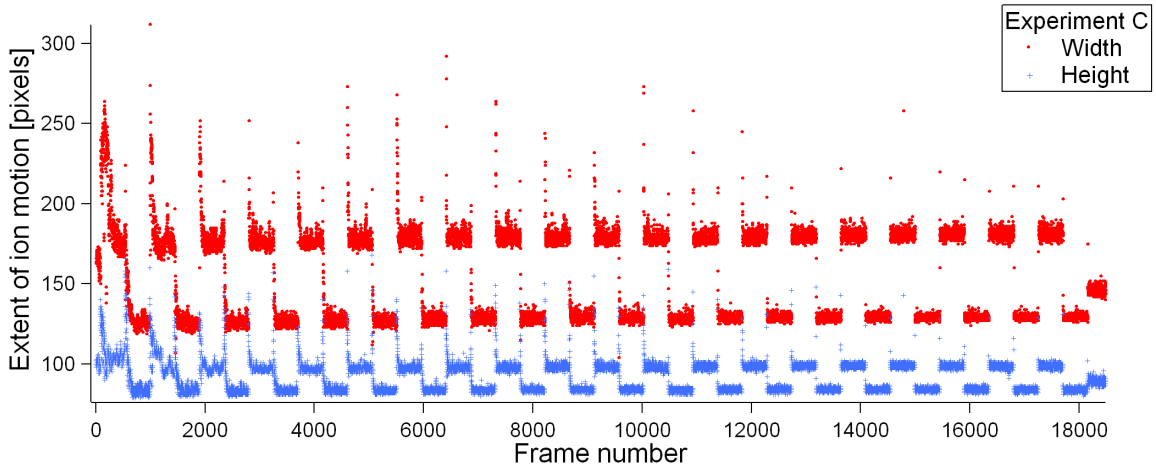
Experiment C
Width
Height
Extent of ion motion [pixels]
100
150
200
250
300
0
2000
4000
6000
8000
10000
12000
14000
16000
18000
Frame number

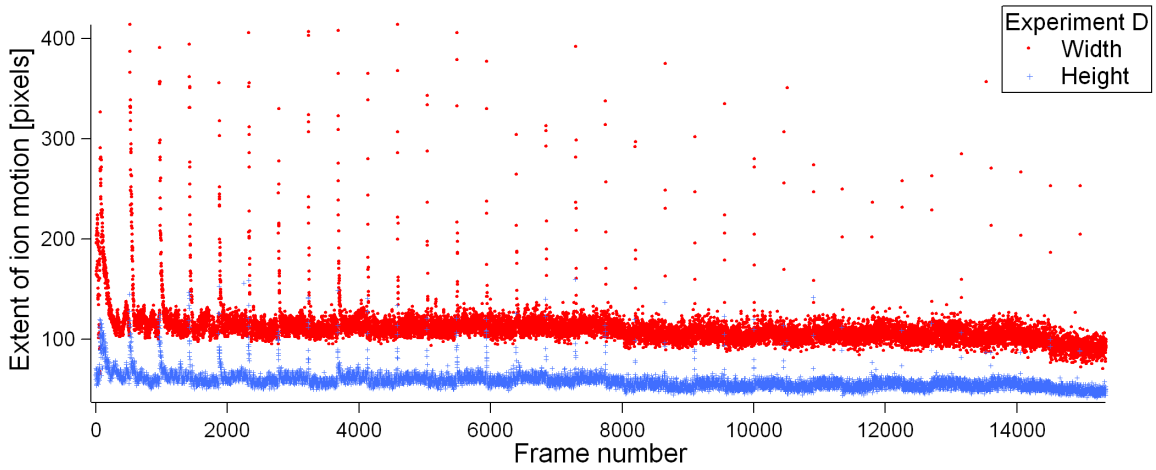
Experiment D
Width
Height
Extent of ion motion [pixels]
100
200
300
400
0
2000
4000
6000
8000
10000
12000
14000
Frame number

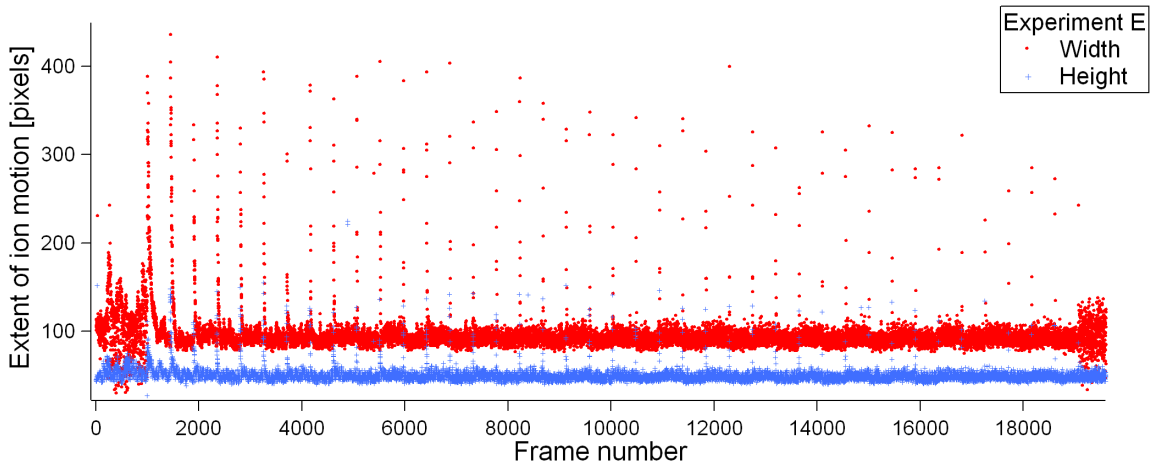
Experiment E
Width
Height
Extent of ion motion [pixels]
400
300
200
100
0
2000
4000
6000
8000
10000
12000
14000
16000
18000
Frame number

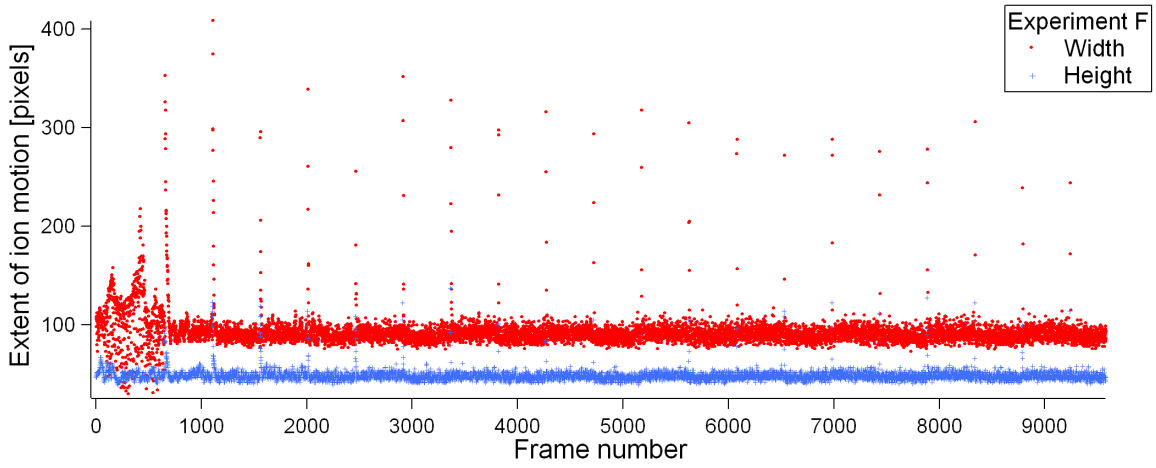
Experiment F
Width
Height
Extent of ion motion [pixels]
400
300
200
100
0
1000
2000
3000
4000
5000
6000
7000
8000
9000
Frame number

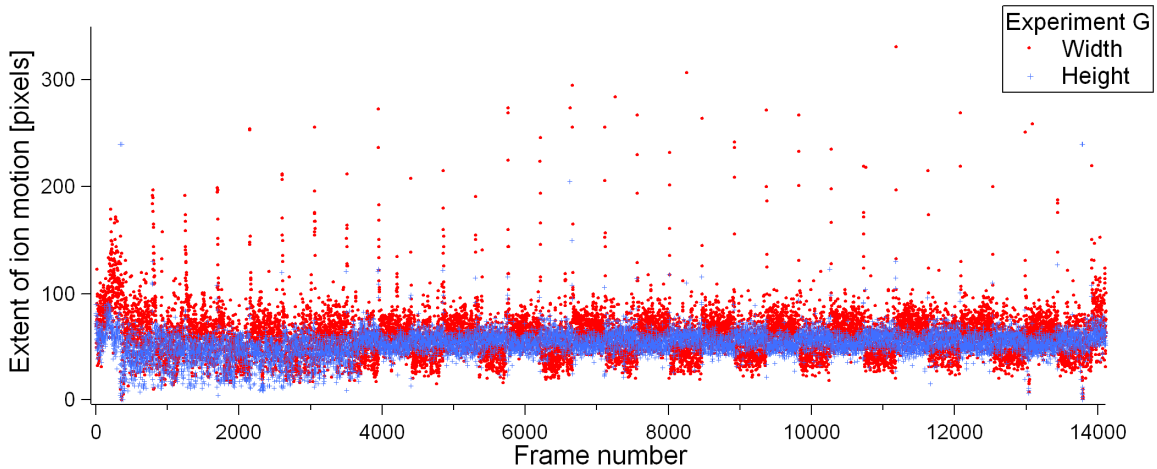
Experiment G
Width
Height
Extent of ion motion [pixels]
300
200
100
0
2000
4000
6000
8000
10000
12000
14000
Frame number

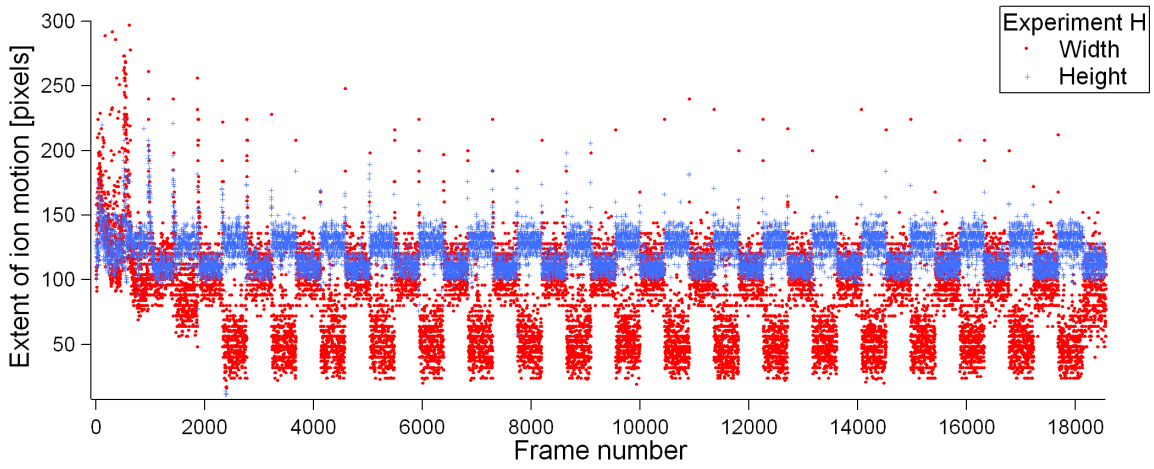

A.2 Pressures

Once the frames have been processed into heights and widths, a decaying exponential plus constant is fit to each region where ringing occurs. The kicks that induce ringing are evenly spaced 15 seconds (about 450 frames) apart. The exponential decay time constants from these fits are then inserted into Eq. (5.13) to produce these plots. Also on these plots are the readings from the Leybold and Edwards gauges. Since neither of these gauges is accurate in the region under investigation, the reading that the Alcatel gauge would show is calculated from that of the Leybold gauge. This calculation is based on a fit of Leybold pressure vs. Alcatel pressure as described in Sec. 6.2.2.

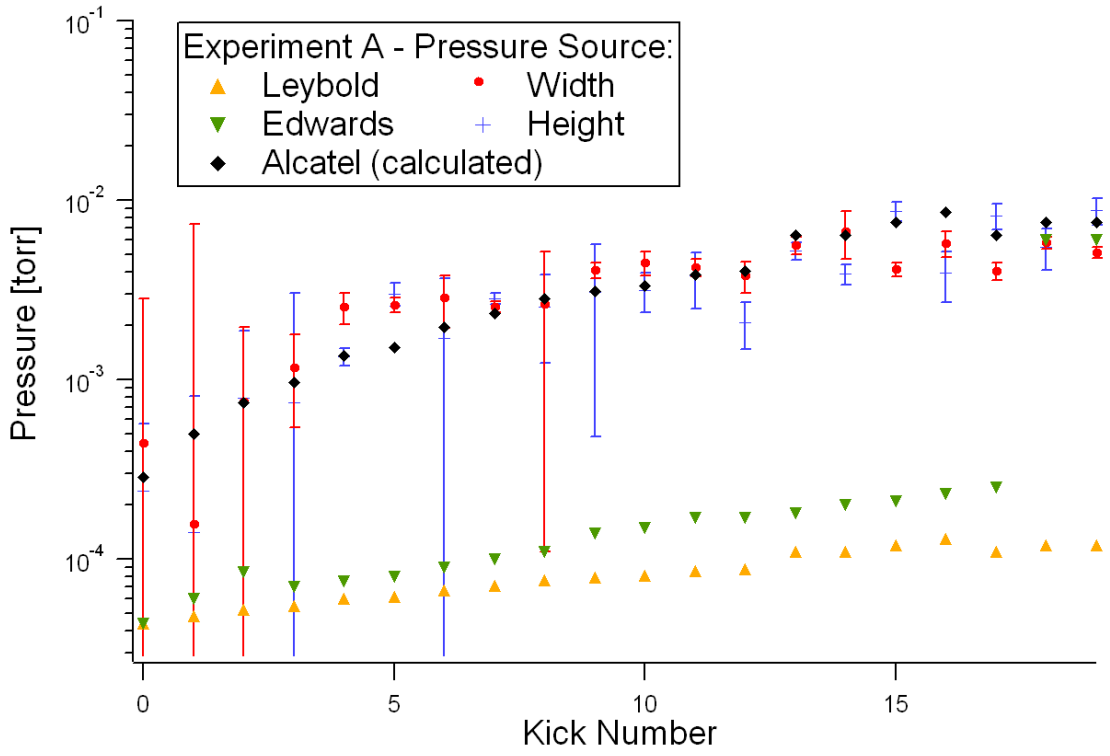
Experiment A - Pressure Source:
Leybold
Edwards
Alcatel (calculated)
Width
Height
Pressure [torr]
Kick Number
10^-1
10^-2
10^-3
10^-4
0
5
10
15

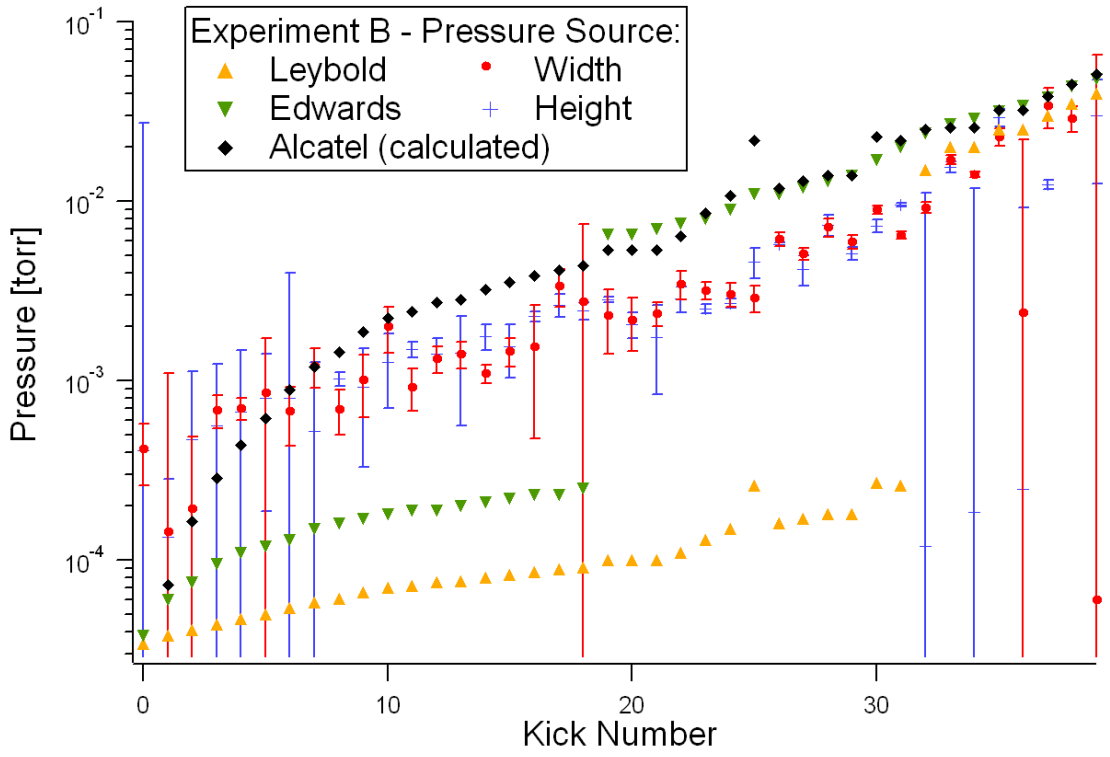
Experiment B - Pressure Source:
Leybold
Edwards
Alcatel (calculated)
Width
Height
Pressure [torr]
Kick Number
10^-1
10^-2
10^-3
10^-4
0
10
20
30

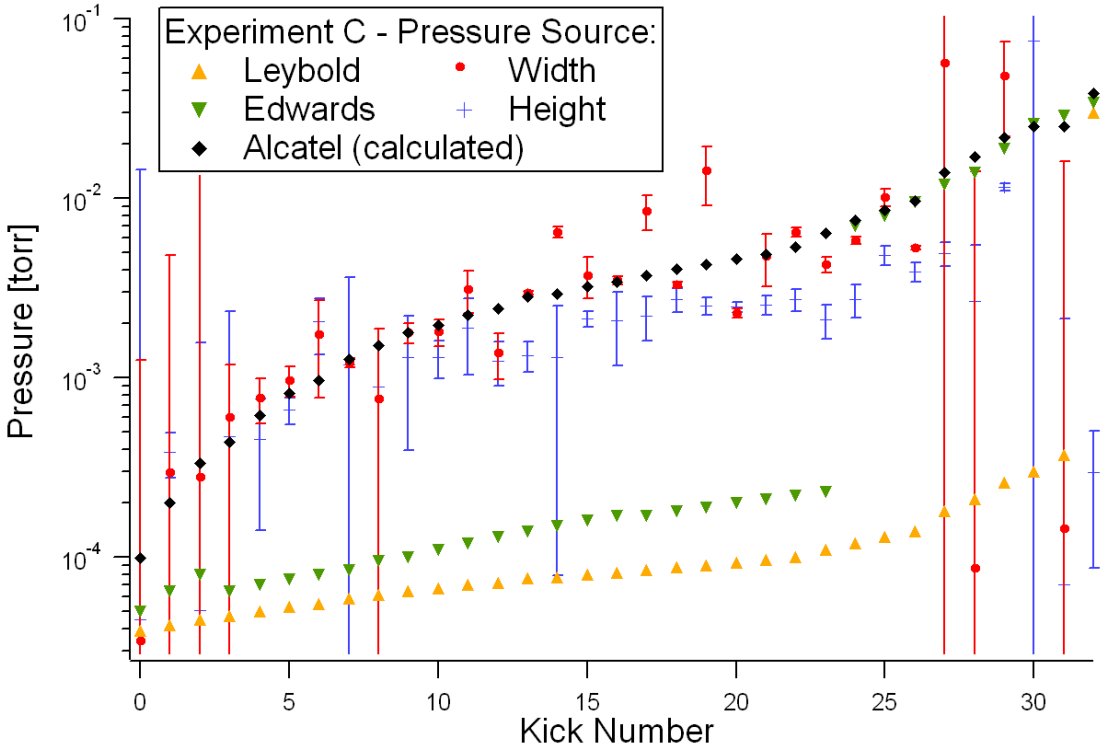
Experiment C - Pressure Source:
Leybold
Edwards
Alcatel (calculated)
Width
Height
Pressure [torr]
Kick Number

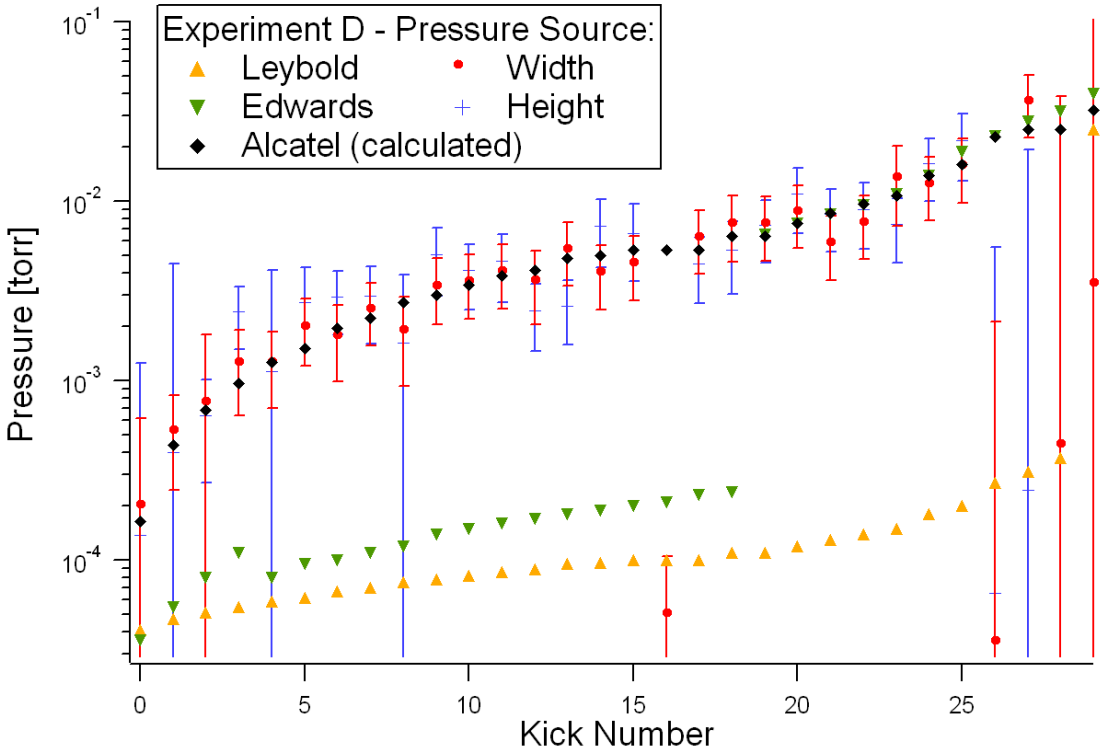
Experiment D - Pressure Source:
Leybold
Edwards
Alcatel (calculated)
Width
Height
Pressure [torr]
Kick Number

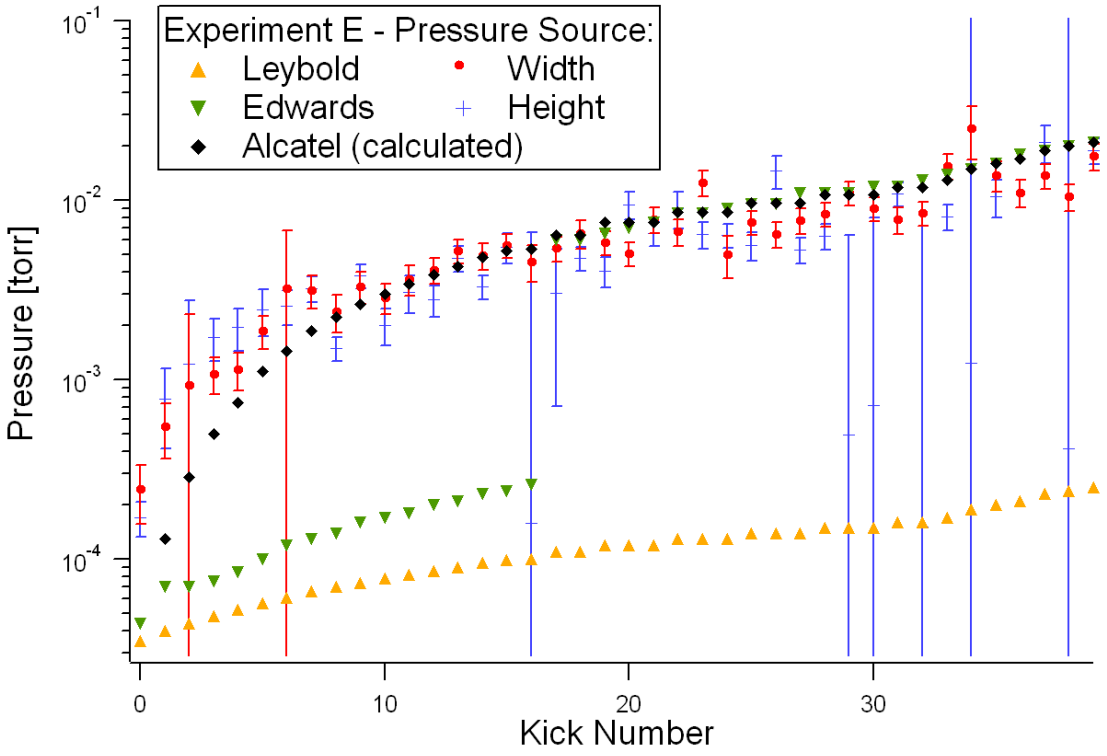
Experiment E - Pressure Source:
Leybold
Edwards
Alcatel (calculated)
Width
Height
Pressure [torr]
Kick Number

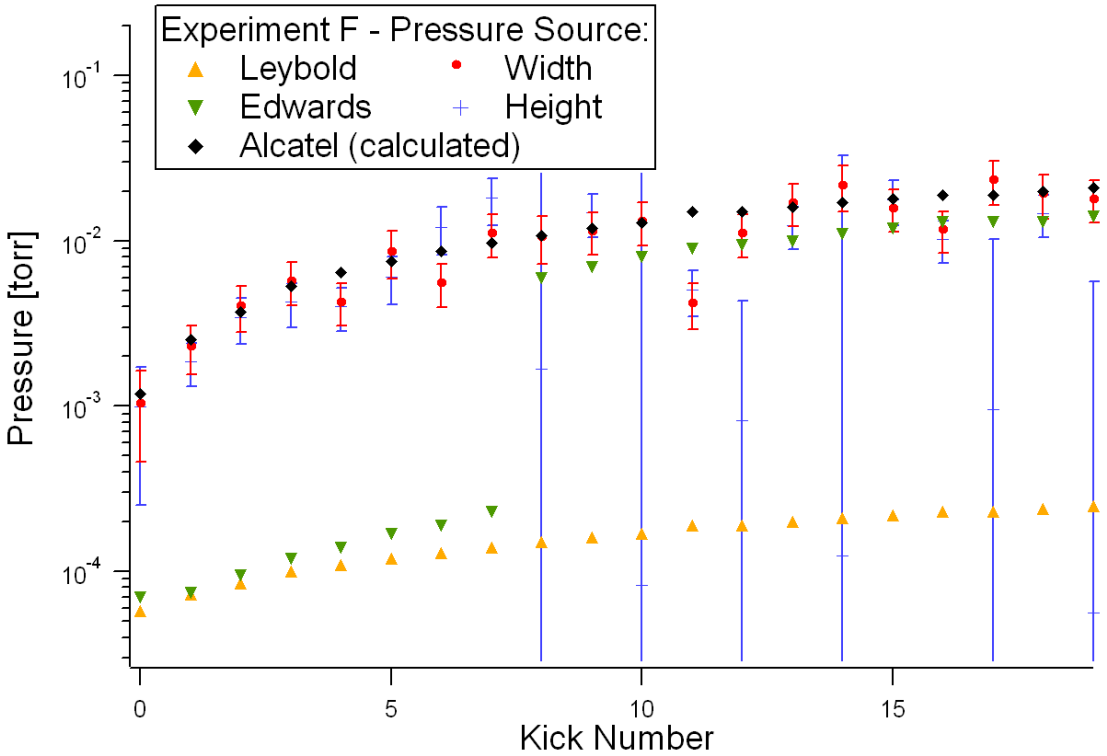
Experiment F - Pressure Source:
Leybold
Edwards
Alcatel (calculated)
Width
Height
Pressure [torr]
Kick Number

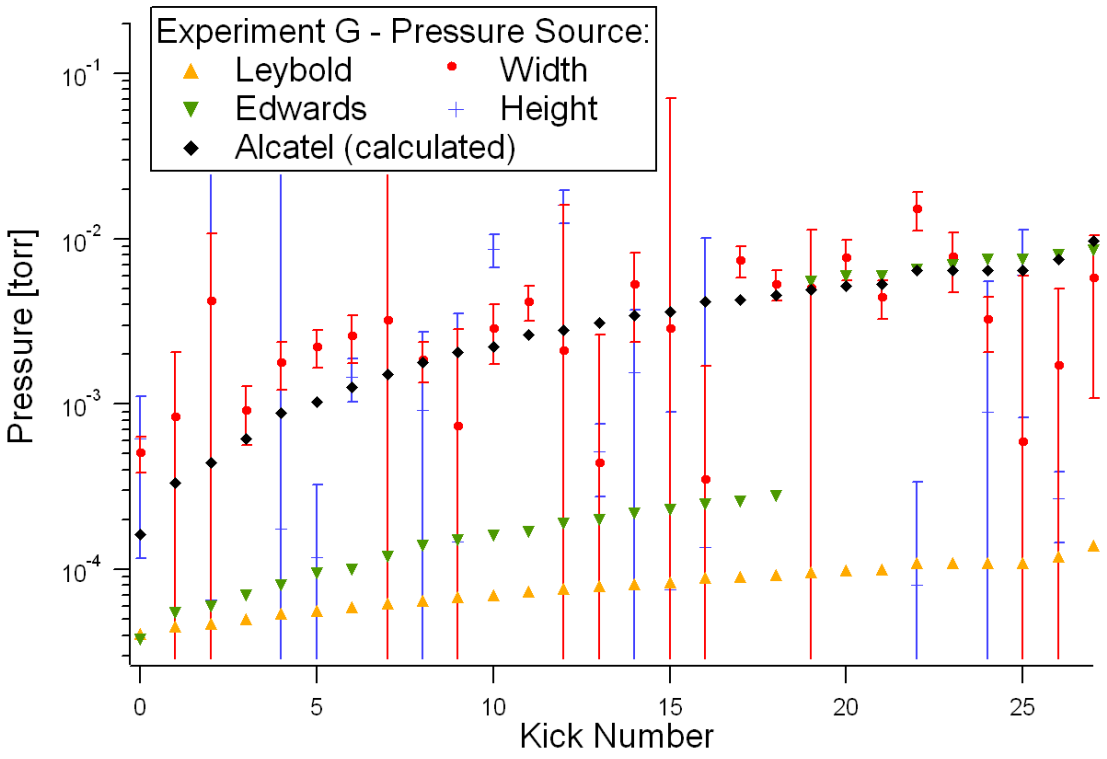
Experiment G - Pressure Source:
Leybold
Edwards
Alcatel (calculated)
Width
Height
Pressure [torr]
Kick Number

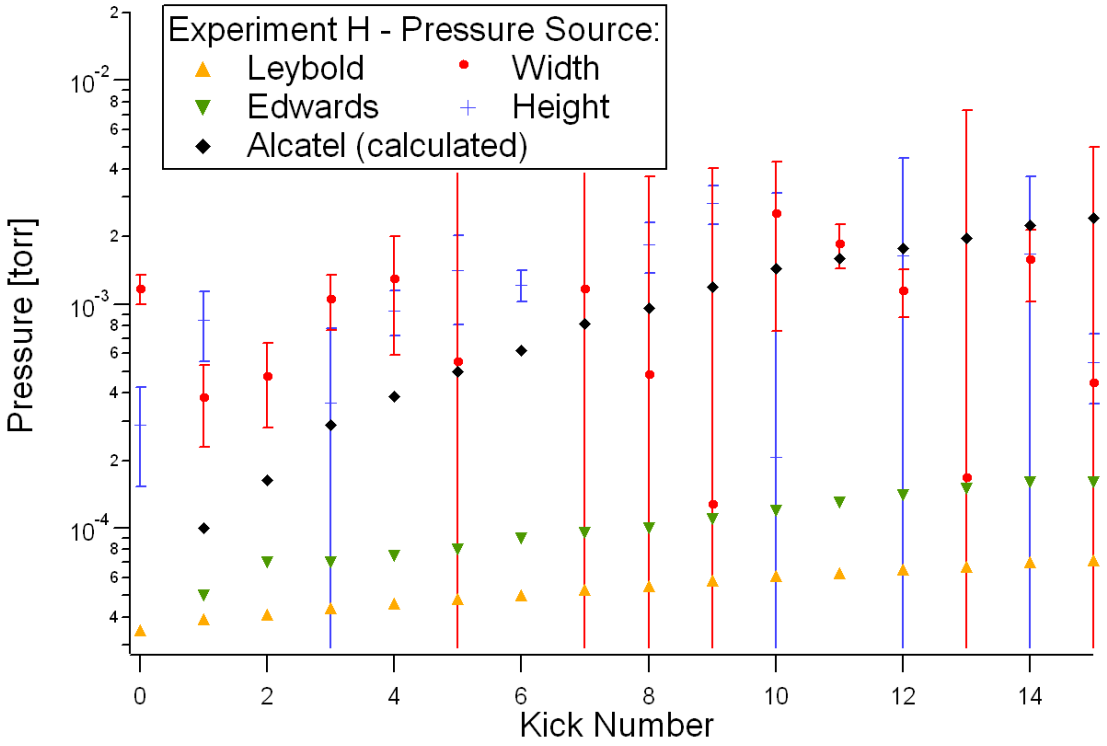
Experiment H - Pressure Source:
Leybold
Edwards
Alcatel (calculated)
Width
Height
Pressure [torr]
Kick Number

Bibliography

[AF86] S. Arnold and L.M. Folan. Fluorescence spectrometer for a single electrodynamically levitated microparticle. *Rev. Sci. Instrum.*, 57:2250–2253, 1986.

[BCS89] R. C. Beavis, B. T. Chait, and K. G. Standing. Factors affecting the ultraviolet laser desorption of proteins. *Rapid Commun. Mass Spectrom.*, 3:233–237, 1989.

[Bir45] Raymond T. Birge. The 1944 values of certain atomic constants with particular reference to the electronic charge. *Am. J. Phys.*, 16:63–73, 1945.

[BZ88] R. Blatt and P. Zoller. Quantum jumps in atomic systems. *Eur. J. Phys.*, 9:250, 1988.

[CBB+05] J. Chiaverini, R. B. Blakestad, J. Britton, J. D. Jost, C. Langer, D. Leibfried, R. Ozeri, and D. J. Wineland. Surface-electrode architecture for ion-trap quantum information processing. *Quantum Inf. Comput.*, 5:419, 2005.

[CPK+02a] Y. Cai, W.-P. Peng, S.-J. Kuo, Y. T. Lee, and H.-C. Chang. Single-particle mass spectrometry of polystyrene microspheres and diamond nanocrystals. *Anal. Chem.*, 74:232–238, 2002.

[CPK+02b] Y. Cai, W.-P. Peng, S.-J. Kuo, S. Sabu, C.-C. Han, and H.-C. Chang. Optical detection and charge-state analysis of MALDI-generated particles

with molecular masses larger than 5 MDa. *Anal. Chem.*, 74:4434–4440, 2002.

[CZ95] J. I. Cirac and P. Zoller. Quantum computations with cold trapped ions. *Phys. Rev. Lett.*, 74:4091, 1995.

[Deh67] H. G. Dehmelt. Radiofrequency spectroscopy of stored ions I: Storage. *Adv. Atom. Mol. Phys.*, 3:53, 1967.

[DHL+04] L. Deslauriers, P. C. Haljan, P. J. Lee, K-A. Brickman, B. B. Blinov, M. J. Madsen, and C. Monroe. Zero-point cooling and low heating of trapped $^{111}Cd^{+}$ ions. *Phys. Rev. A*, 70:43408, 2004.

[Fis59] E. Fischer. The three dimensional stabilization of charge carriers in a [h.f. electric] quadrupole field. *Z. Phys. (Germany)*, 156:1–26, 1959.

[Fis97] P. T. Fisk. Trapped-ion and trapped-atom microwave frequency standards. *Reports on Progress in Physics*, 60:761, 1997.

[G+91] G. Gabrielse et al. Cryogenic antiprotons: A 1000-fold improvement in their measured mass. *Am. Inst. Phys. Conf. Ser.*, 233:549, 1991.

[GH02] C. G. Granqvist and A. Hultåker. Transparent and conducting ITO films: new developments and applications. *Thin Solid Films*, 411:1, 2002.

[Gho95] P. K. Ghosh. *Ion Traps*. Clarendon Press, Oxford, 1995.

[Gor00] R. G. Gordon. Criteria for choosing transparent conductors. *MRS Bulletin*, page 52, August 2000.

[H+05] W. K. Hensinger et al. T-junction ion trap array for two-dimensional ion shuttling, storage, and manipulation. *arXiv:quant-ph/0508097*, 2005.

[HB93] J. Hoffnagle and R. G. Brewer. Frequency-locked motion of two particles in a paul trap. *Phys. Rev. Lett.*, 71:1828, 1993.

[HS03] J. P. Home and A. M. Steane. Electric octopole configurations for fast separation of trapped ions. *arXiv:quant-ph/0411102*, 2003.

[IBW87] W. M. Itano, J. C. Bergquist, and D. J. Wineland. Laser spectroscopy of trapped atomic ions. *Science*, 237:612, 1987.

[JPM90] G. R. Janik, J. D. Prestage, and L. Maleki. Simple analytic potentials for linear ion traps. *J. Appl. Phys.*, 67:6050, 1990.

[K+05] J. Kim et al. System design for large-scale ion trap quantum information processor. *Quantum Inf. Comput.*, 5:515, 2005.

[KBBH87] M. Karas, D. Bachmann, U. Bahr, and F. Hillenkamp. Matrix-assisted ultraviolet laser desorption of non-volatile compounds. *Int. J. Mass Spectrom. Ion Process.*, 78:53–68, 1987.

[KMKP05] J. H. Kim, G. W. Mulholland, S. R. Kukuck, and D. Y. H. Pui. Slip correction measurements of certified PSL nanoparticles using a nanometer differential mobility analyzer (nano-DMA) for Knudsen number from 0.5 to 83. *J. Res. Natl. Inst. Stand. Technol.*, 110:31, 2005.

[KMW02] D. Kielpinski, C. Monroe, and D. J. Wineland. Architecture for a large-scale ion-trap quantum computer. *Nature*, 417:709, 2002.

[KPM+05] J. Kim, S. Pau, Z. Ma, H. R McLellan, J. V. Gates, A. Kornblit, and R. E. Slusher. System design for large-scale ion trap quantum information processor. *Quantum Inf. Comput.*, 5:515–537, 2005.

[LC01] Wen-Hui Lin and Tai-Shung Chung. Gas permeability, diffusivity, solubility, and aging characteristics of 6FDA-durene polyimide membranes. *J. Membrane Sci.*, 186:183–193, 2001.

[Mee04] D. C. Meeker. Basic electrostatic analysis, version 1.0. http://femm.foster-miller.net, 2004.

[MHS+04] M. J. Madsen, W. K. Hensinger, D. Stick, J. A. Rabchuk, and C. Monroe. Planar ion trap geometry for microfabrication. *Appl. Phys. B*, 78:639, 2004.

[NF01] M. Nasse and C. Foot. Influence of background pressure on the stability region of a Paul trap. *Eur. J. Phys.*, 22:563, 2001.

[NLR+99] H. C. Nägerl, D. Leibfried, H. Rohde, G. Thalhammer, J. Eschner, F. Schmidt-Kaler, and R. Blatt. Laser addressing of individual ions in a linear ion trap. *Phys. Rev. A*, 60:145, 1999.

[Pau90] W. Paul. Electromagnetic traps for charged and neutral particles. *Rev. Mod. Phys.*, 62:531, 1990.

[PCC04] Wen-Ping Peng, Yong Cai, and Huan-Cheng Chang. Optical detection methods for mass spectrometry of macroions. *Mass Spec. Rev.*, 23:443–465, 2004.

[PDM89] J. D. Prestage, G. J. Dick, and L. Maleki. New ion trap for frequency standard applications. *J. Appl. Phys.*, 66:1013, 1989.

[PLB+06] C. E. Pearson, D. R. Leibrandt, W. S. Bakr, W. J. Mallard, K. R. Brown, and I. L. Chuang. Experimental investigation of planar ion traps. *Phys. Rev. A*, 73:032307, 2006.

[POF58] W. Paul, O. Osberghaus, and E. Fischer. An ion cage. *Forsch. ber. Wirtsch. Verkehrsminist. Nordrh.-Westfal. (Germany)*, 415:42 pp, 1958.

[R+02] M. A. Rowe et al. Transport of quantum states and separation of ions in a dual RF ion trap. *Quantum Inf. Comput.*, 2:257, 2002.

[Red99] P. A. Redhead. The ultimate vacuum. *Vacuum*, 53:137–149, 1999.

[RGB+92] M. G. Raizen, J. M. Gilligan, J. C. Bergquist, W. M. Itano, and D. J. Wineland. Linear trap for high-accuracy spectroscopy of stored ions. *J. Mod. Opt.*, 39:233, 1992.

[SGA+05] S. Stahl, F. Galve, J. Alonso, S. Djekic, W. Quint, T. Valenzuela, J. Verdú, M. Vogel, and G. Werth. A planar Penning trap. *Eur. Phys. J. D*, 32:139–146, 2005.

[SHKS01] M. Sawada, M. Higuchi, S. Kondo, and H. Saka. Characteristics of indium-tin-oxide/silver/indium-tin-oxide sandwich films and their application to simple-matrix liquid-crystal displays. *Jpn. J. Appl. Phys.*, 40:3332, 2001.

[SS03] M. Sasura and A. M. Steane. Fast quantum logic by selective displacement of hot trapped ions. *Phys. Rev. A*, 67:062318, 2003.

[Ste04] A. M. Steane. How to build a 300 bit, 1 Gop quantum computer. *arXiv:quant-ph/0412165*, 2004.

[T+00] Q. A. Turchette et al. Heating of trapped ions from the quantum ground state. *Phys. Rev. A*, 61:63418, 2000.

[Tod91] J. F. Todd. Ion trap mass-spectrometer - past, present and future. *Mass Spec. Reviews*, 10:3, 1991.

[TWK+98] Q. A. Turchette, C. S. Wood, B. E. King, C. J. Myatt, D. Leibfried, W. M. Itano, C. Monroe, and D. J. Wineland. Deterministic entanglement of two trapped ions. *Phys. Rev. Lett.*, 81:3631, 1998.

[WL95] P. Willems and K. Libbrecht. Creating long-lived neutral-atom traps in a cryogenic environment. *Phys. Rev. A*, 51:1403, 1995.

[WMI+98] D. J. Wineland, C. Monroe, W. M. Itano, D. Leibfried, B. E. King, and D. M. Meekhof. Experimental issues in coherent quantum-state manipulation of trapped atomic ions. *J. Res. Natl. Inst. Stand. Technol.*, 103:259, 1998.

[WO91] H. Winter and H. W. Ortjohann. Simple demonstration of storing macroscopic particles in a "Paul trap". *Am. J. Phys.*, 59:807, 1991.

[WSL59] R. F. Wuerker, H. Shelton, and R. V. Langmuir. Electrodynamic containment of charged particles. *J. Appl. Phys.*, 30:342–349, 1959.

[XYLL00] Xiaochun Xu, Weishen Yang, Jie Liu, and Liwu Lin. Synthesis of a high-permeance NaA zeolite membrane by microwave heating. *Adv. Mater.*, 12:195–198, 2000.

[YF84] M. Yamashita and J.B. Fenn. Electrospray ion source: Another variation on the free-jet theme. *J. Phys. Chem.*, 88:4451–4459, 1984.

[YLS06] B. Yurke, D. Leibrandt, and R. Slusher. Minimizing ion trap thermal noise decoherence. in press, 2006.